High-frequency nanomechanical resonators for sensor applications

Thesis by

Igor Bargatin

In Partial Fulfillment of the Requirements

for the Degree of

Doctor of Philosophy

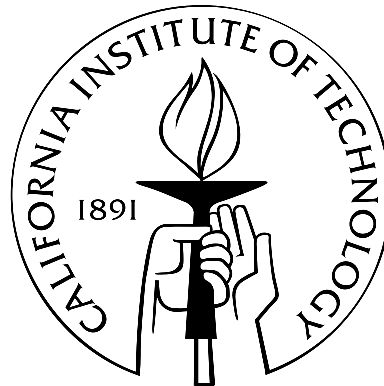

California Institute of Technology

Pasadena, California

2008

(Defended May 14, 2008)

© 2008

Igor Bargatin

All Rights Reserved

Acknowledgements

I would not have been where I am today without all the help and support I received during my Caltech studies. I will always be grateful to my advisor, Michael L. Roukes, for his encouragement and gentle guidance, for letting me explore the subjects that excited me most, and bearing with my habit of challenging authorities. I thank Edward B. Myers, who has taught me the dark arts of experimental measurements and helped me throughout my studies. I thank Ben Gudlewski and Steve Stryker for sharing their expertise and helping me with fabrication at nano- and macroscale, respectively. I appreciate the opportunity of working together with Dirk Orgassa, Jeff Fingler, Jessica Arlett, Mo Li, Philip Feng, Vincent Agache, Jan Hales, and Rassul Karabalin. I also appreciate the many discussions I had with Prof. Chris Hammel, Prof. John Sader, Denis Pelekhov, Sotiris Masmanidis, Henk Postma, Matt LaHaye, Blake Axelrod, Mehmet Selim Hanay, Radovan Urban, Wayne Hiebert, Akshay Naik, Wonhee Lee, Murali Ghatsekar, Jie Xiang, Matt Matheny, and all other members of the Roukes group. I thank the members of my defense committee—Professors Michael C. Cross, Kerry J. Vahala, and Axel Scherer—for their time and suggestions.

I am forever indebted to my parents, who let me follow my dreams to faraway cities and lands, and my brother, who supported me on this journey. Finally, my love and gratitude go to my wife Inna, with whom we shared and continue to share many adventures in the lab and and at home. Meeting and marrying her was by far my best achievement at Caltech.

Abstract

This thesis describes new ways of operating high-frequency nanomechanical resonators and using them for sensor applications.

The first part of the thesis is devoted to the techniques of detecting, actuating, and tuning the resonance motion of nanomechanical resonators. First, I consider piezoresistive detection using integrated thin-film piezoresistors made of doped semiconductors or metals. I describe the piezoresistive downmixing technique, which typically results in better performance than the conventional DC biasing technique. I then proceed to the possible ways of actuating the motion of nanomechanical resonators. After describing the challenges of applying the piezoshaker actuation technique to high-frequency resonators, I consider two alternatives: permanent-magnet magnetomotive actuation and Joule-heat-driven thermoelastic actuation. I demonstrate that the combination of thermoelastic actuation and piezoresistive detection can be used to efficiently detect multiple modes of nanomechanical resonators. Finally, I consider two ways of tuning the frequency of nanomechanical resonators: electrostatic tuning and absorptive tuning.

The second part of the thesis is devoted to applications of nanoscale resonators to spin sensing, studies of dissipation of mechanical motion, and gas sensing. I consider possible ways of observing the coupling between mechanical motion and spins, describe our experimental results, and explore the analogy between coupled the spin–resonator system and the quantum-optical model of a laser. I then describe the results of quality-factor measurements in vacuum and air for doubly clamped beams and other resonator geometries. Finally, I describe a way to build better gas sensors by using arrays of nanomechanical resonators and present the preliminary gas-sensing data.

Contents

Acknowledgements **iii**

Abstract **iv**

List of figures **ix**

List of tables **x**

Introduction **1**

1 Piezoresistive detection of resonant motion of nanomechanical resonators **5**

1.1 Piezoresistive detection using semiconductors and metals 8

1.2 Piezoresistive downmixing 10

2 Actuation techniques for nanomechanical resonators **18**

2.1 Piezoshaker actuation 20

2.2 Room-temperature magnetomotive actuation 25

2.3 Thermoelastic actuation 27

3 Frequency tuning techniques for nanomechanical resonators **35**

3.1 Electrostatic tuning 36

3.2 Adsorption tuning 39

4 Nanomechanical sensing of spin systems **45**

4.1 Mechanisms of coupling between spins and mechanical motion 48

4.2 Experimental results 57

4.3 Analogy to quantum optics: Cantilaser 63

5 Studies of quality factors of nanomechanical resonators **72**

5.1 Quality factors of flexural modes of beams in vacuum 75

5.2 Quality factors of flexural modes of beams in air 81

5.3 Alternative resonator designs for high quality factors in fluids 85

6 Nanomechanical resonator arrays for gas sensing applications **91**

6.1 Response of electrically connected arrays: Theory 92

6.2 Response of electrically connected arrays: Experiment 98

6.3 Preliminary gas sensing data 106

Concluding remarks **111**

Appendices **114**

A Phase relationships in piezoresistive downmixing **114**

B Two-port measurements using piezoresistive downmixing and thermoelastic actuation **118**

C Simulation of thermoelastic drive and piezoresistive detection **123**

Bibliography **127**

List of Figures

1.1 Schematics of optical, capacitive, magnetomotive, and piezoresistive detection techniques 6

1.2 Scanning electron micrographs of integrated piezoresistors 9

1.3 Direct-current piezoresistive readout schematic 11

1.4 Diagram of piezoresistive downmixing circuit 12

1.5 Optical and scanning electron micrographs of a silicon piezoresistive cantilever 14

1.6 Resonance signals measured using DC and downmixing piezoresistive techniques . . . 15

1.7 Thermomechanical noise peaks from the two vibration mode of a silicon cantilever . . 16

2.1 Schematics of piezoshaker, capacitive, magnetomotive, and electrothermal detection techniques 19

2.2 Resonance curves of the first and second mode of a silicon cantilever obtained using piezoshaker actuation at various temperatures 22

2.3 3D and density plots of resonance signal for continuously tuned cantilever resonance . 23

2.4 XY parametric plots of the response of two 20-MHz in-plane cantilever resonators with thermoelastic and piezoshaker actuation 24

2.5 Photograph and schematic of a room-temperature magnetomotive actuation setup and the obtained data 26

2.6 Scanning electron micrograph of one of a device used for thermoelastic drive and a schematic of the experimental setup. 28

2.7 Representative signal produced by thermoelastic drive and piezoresistive detection . . 30

2.8 Normalized efficiency of electrothermal drive and piezoresistive detection 33

3.1 Electrostatic tuning of an out-of-plane beam resonator 37

3.2 Electrostatic tuning of an in-plane beam resonator 38

3.3 Resonance curves of a tuned in-plane beam resonator 38

3.4 Schematic of the adsorptive tuning setup 40

3.5 Resonance curves at various stages of the adsorptive tuning process 41

3.6 Effect of adsorptive tuning on quality factor 42

3.7 Saturation of adsorption tuning 43

4.1 Schematics of longitudinal and transverse MRFM 46

4.2 Geometries of different experiments for observing the coupling between the transverse magnetization and mechanical motion 49

4.3 Simulation of transverse MRFM 51

4.4 Effective in-plane magnetic field 56

4.5 Images of doubly clamped beams with thin cobalt films 58

4.6 Magnetic response of a beam with a thin cobalt film 59

4.7 Changes in quality factor during adsorptive tuning of a beam with ferromagnetic film 60

4.8 Time-domain response of resonator to a pulse drive 61

4.9 Schematic of a mechanical laser device 65

4.10 Characteristic transients of a cantilaser for various numbers of resonant nuclei 69

5.1 Quality factor of flexural modes for devices of different geometries 76

5.2 Quality factor of flexural modes for devices of different geometries 77

5.3 Quality factor of flexural modes at different temperatures 79

5.4 Quality factors of flexural modes due to viscous damping in air 83

5.5 Simulation and measurements of the in-plane mode of a center-supported beam 85

5.6 Simulation and measurements of the extensional mode of a center-supported beam . . 87

5.7 Measurement schematic and finite-element simulation of a Lamé plate mode 88

6.1 Schematic and scanning electron micrographs of an electrically connected array 92

6.2 Simulated X and Y quadratures of the response of arrays with varying frequency dispersion . . . 97

6.3 Simulated X and Y quadratures of the response of arrays with varying quality factors 97

6.4 Schematics of regular and balanced two-port measurements of arrays . . . 99

6.5 Resonant response of the CK-A array in vacuum and air . . . 100

6.6 Resonant response of the A3A8 array in vacuum and air . . . 101

6.7 Optically detected spectrum of array A3A9 for different positions of the laser spot . . 102

6.8 Balanced detection of the arrays CK-2-A and CK-2-B in vacuum . . . 105

6.9 Balanced detection of the arrays CK-2-A and CK-2-B in air . . . 105

6.10 Integration of the array sensors into a commercial gas chromatography system 107

6.11 Gas chromatograms obtained with an array sensor . . . 108

A.1 Parametric plot of the real and imaginary parts of the harmonic resonance response . 115

A.2 Parametric plot of the real and imaginary parts of the resonance response of a 37 MHz beam resonator . . . 116

B.1 Schematic of two-port measurement using thermoelastic actuation and piezoresistive detection . . . 119

B.2 Wide frequency sweep for a two-port measurement of a 1.6-μm long cantilever 120

List of Tables

2.1 Predicted and experimental resonance frequencies and quality factors of various modes of a 16-μm-long beam E7A3 . . . 31

5.1 Experimental resonance frequencies and quality factors in vacuum and air for various modes of the 16-μm-long beam E7A3 . . . 82

5.2 Experimental resonance frequencies and quality factors in vacuum and air for various modes of the 8-μm-long beam E5C2 . . . 83

6.1 Fitted parameters of the resonance peaks of arrays of cantilevers of different dimensions. 103

Introduction

Like sportsmen, researchers are often motivated by the possibility of setting a new record and beating the competition. Practically every day there is news that scientists or engineers have developed a device that is faster, or slower, or bigger, or smaller, or darker, or brighter, or hotter, or colder, et cetera, et cetera, than ever before. Apart from the bragging rights for their inventors, many of these devices eventually result in real-life applications because these record-breaking properties allow people to do something useful better than before.

One general trend that has produced many such records and applications over the last several decades is miniaturization. The most obvious example of this trend is the amazing progress of electronic devices, which by now have permeated every aspect of modern life. The scaling of transistors from the initial few centimeters to the current few tens of a nanometer has not only miniaturized the radios of the 1940s, but has also produced thousands of new kinds of devices that could not even be imagined at the time (think iPods or cell phones). In the last couple of decades, the miniaturization of electronic devices has entered the nanoscale and engendered the new fields of nanoscience and nanotechnology, which now encompass not only electronic but many other types of devices. These nano-enabled devices promise to revolutionize many more areas of modern life, from materials to energy technology to medicine.

Over the last two decades, the fabrication techniques developed by the semiconductor industry have been applied to creating miniaturized devices with moving parts. Since electrical signals were usually used to actuate or detect the motion of these devices, they acquired the name *microelectromechanical systems* or MEMS [1, 2]. Since their appearance, MEMS have enabled many devices with record properties such as inkjet printers, optical switchers, displays, electronic filters, and all

kinds of sensors.

Microelectromechanical systems are now passing the baton of miniaturization to nanoelectromechanical systems (NEMS), which generally feature at least two characteristic dimensions of less than one micrometer. In particular, nanomechanical resonators promise to revolutionize many sensor applications. Their small size and the new properties emerging at the nanoscale have resulted in new records of sensitivity in charge [3], mass [4, 6, 5], force [7], and spin [8, 9] measurements. The detection sensitivity at cryogenic temperatures has now reached the range where a number of quantum effects can be observed using nanomechanical resonators [10, 11, 12].

In this thesis, I explore new types of nanomechanical resonators and the applications they enable. One of the continuing challenges in the field of nanomechanical resonators is finding new efficient ways to control the motion of the ever-shrinking nanomechanical devices. A large part of my graduate studies was devoted to finding new ways to actuate, detect, and tune the motion of nanomechanical resonators. Another large part of my graduate studies was devoted to developing new types of sensors that would use these types of resonators.

The six chapters of this thesis are arranged in a roughly chronological order. During the first few years of my studies, my main goal was to perform mechanical detection of nuclear magnetic resonance at the Larmor frequency, i. e., to realize the situation when the resonance frequency of the nanomechanical resonator and the frequency of magnetic resonance are the same and observe some form of interaction between the mechanical and spin systems. Working toward this goal required a lot of preparatory work. The first problem we needed to solve was developing a new method of motion detection for silicon piezoresistive cantilevers that would work at frequencies of tens of megahertz—the typical resonance frequency range of nuclear magnetic resonance. The solution was to use AC biasing of piezoresistive devices, and downmix the signal to low frequencies where measurements were much simpler. Chapter 1 describes piezoresistive detection and the piezoresistive downmixing technique in more detail.

The next issue we needed to address was actuation of nanomechanical resonators in the same frequency range of tens of megahertz. The two methods widely used in our group to actuate nanome-

chanical devices at the time—piezoshaker and magnetomotive actuation—proved inadequate for our purposes. Magnetomotive actuation requires a strong magnetic field, which makes it very inconvenient for studying magnetic resonances, where independent control of magnetic field is needed. The piezoshaker actuation turned out to be impractical also because the piezoshaker drive has a strong and arbitrary frequency dependence, especially at high frequencies and low temperatures. The solution we have developed involved the use of thermoelastic actuation, which suited the needs of Larmor-frequency measurement and, in addition, allowed us to use multiple modes of the nanomechanical resonators. Chapter 2 provides the details on piezoshaker, magnetomotive, and thermoelastic actuation techniques.

Another prerequisite for magnetic resonance experiments was the ability to tune the resonance frequency of nanomechanical resonators. The most common way to perform such tuning in MEMS devices is by using capacitive or electrostatic tuning. I was involved in the experiments that successfully applied this technique to nanomechanical resonators. However, the small dimensions of nanomechanical resonators limited the tuning range in these experiments and also often resulted in the destruction of the device due to electrostatic snap-in or dielectric breakdown. This motivated me to develop the adsorptive frequency tuning technique for nanomechanical resonators. This technique operates at liquid-helium temperatures and relies on adsorption of inert gas molecules on the device, which mass loads the device and tunes the frequency down. The technique allows controlled tuning of frequency by more than 15%, does not interfere with electrical measurements, and has never resulted in the destruction of a device. Chapter 3 describes the experimental results obtained using both capacitive and absorptive tuning of nanomechanical resonators.

After developing the necessary experimental techniques for the actuation, detection, and tuning of mechanical resonances, we were finally ready to try detecting the interaction between mechanical resonators and nuclear spins. I start Chapter 4 by describing two possible mechanisms of coupling between mechanical motion and spins. I then proceed to describe the experiments we have performed in attempt to detect the signature of the interaction between mechanical resonators and nuclear spins. I conclude the chapter by exploring theoretically the analogies between coupled resonator–

spins system and similar systems in quantum optics, in particular, the laser.

The experimental techniques developed for studying mechanical-spin interaction also proved useful for other applications. The first problem I could easily address was the study of quality factors of nanomechanical resonators in both vacuum and air. The combination of thermoelastic actuation and piezoresistive detection allowed me to perform systematic measurements of quality factors for multiple modes of doubly clamped beams. The results of these measurement also suggested ways to achieve high quality factors in fluids by using alternative designs of nanomechanical resonators. Chapter 5 describes the results of quality factor measurement in beams and other types of resonators.

Another promising application for thermoelastic actuation and piezoresistive detection is the detection of arrays of mechanical resonators. Building electrically connected arrays of nanomechanical resonators is the simplest way to improve the sensitivity of NEMS gas sensors. However, successful detection of resonances from entire arrays requires that the resonance frequency and drive are uniform across the array. We were able to achieve both using thermoelastic actuation with the arrays fabricated by our collaborators at LETI (Grenoble, France). These measurements allowed us to detect resonances of arrays with a much higher signal-to-noise ratio than those of individual cantilevers. We have also performed preliminary gas sensing measurements that demonstrated the feasibility of functionalizing entire arrays and using them for gas sensing inside a commercial gas chromatography system. Chapter 6 describes the the theoretical and experimental results relating to the measurements of electrically connected arrays.

I conclude the thesis with the summary of the obtained results and a description of possible future experiments.

Chapter 1

Piezoresistive detection of resonant motion of nanomechanical resonators

There are many ways to detect the resonant motion of nanomechanical devices. Some of these ways are adaptations of detection methods originally developed for microscale devices, while others are unique to nanoscale devices.

In the domain of MEMS [2], which are much larger than NEMS, the most popular detection techniques are optical, capacitive, piezoelectric, piezoresistive, and magnetic. All of these techniques can be adapted to work with nanoscale devices, albeit with some limitations. For example, optical detection works best if the spot size of a focused beam is smaller than the length and the width of the mechanical resonator. Since the minimum size of an optical beam is limited by the wavelength of the used light, most optical techniques become less effective as the dimensions of the resonator are reduced below 1 micron, i. e., enter the nanoscale.[1] Another common drawback of optical detection is the need for macroscopic optical components and careful alignment. Nevertheless, optical and, in particular, interferometric optical detection are widely used because they provide a large measurement bandwidth and displacement sensitivities down to ~ 100 fm/Hz$^{1/2}$ in nanoscale resonators [8, 13].

Capacitive detection, also called electrostatic detection, is very popular in microscale devices since it is easy to integrate into a microfabricated device, consumes little power, and in addition, provides

[1] Recently, an alternative technique of *local* optical detection has been demonstrated [14]. It is based on the coupling between evanescent fields of parallel optical waveguides and is therefore not limited by the laser spot size.

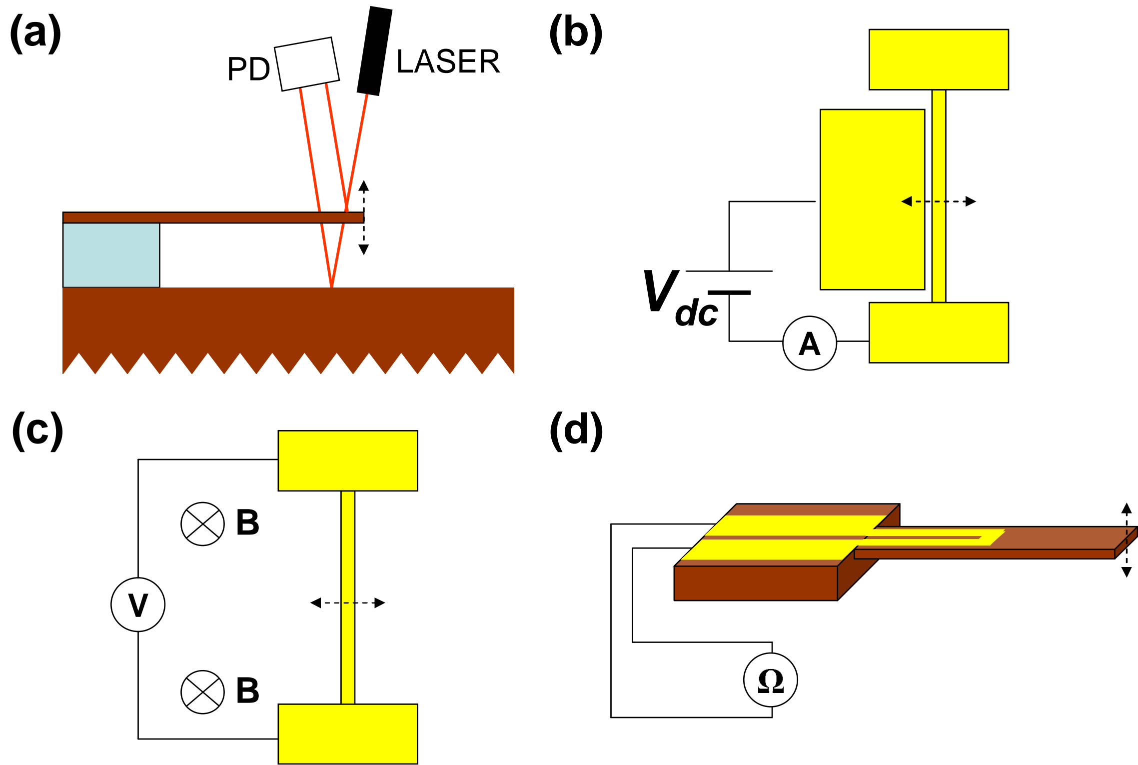

Figure 1.1: Popular detection schemes for nanoscale devices. (a) Schematic side view of a typical laser optical detection technique. The cantilever motion can be detected either though the resulting angular deflection of the reflected beam or through the variation of reflected power due to interference of light reflected from the beam itself and the underlying substrate. (b) Schematic top view of the capacitive detection technique. Periodic motion of the beam resonator changes the capacitance between the beam and the DC-biased side electrode, resulting in detectable AC current flowing through the ammeter. (c) Schematic top view of the magnetomotive detection technique. Periodic motion of the beam resonator changes the magnetic flux through the conducting loop formed by the beam and the outside wires, resulting in AC voltage that is detected by the voltmeter. (d) Schematic view of the piezoresistive detection technique. The motion of the cantilever strains the piezoresistor loop on the top surface of the cantilever. The resulting changes in the resistance can be detected by a number of measurement techniques.

a way to actuate the device at the same time [2]. Scaling capacitive detection and actuation to nanoscale dimensions, however, is challenged by the increasing importance of parasitic capacitances and their deleterious effects.[2] Still, capacitive detection can achieve high displacement sensitivity and can work at a very wide range of temperatures, down to the milliKelvin range of dilution refrigerators.

Magnetic detection of the motion of microscale structures is typically based on the Faraday effect, i. e., generation of a voltage in a loop with a changing magnetic flux. A variety of microcoil structures have been used in *microscale* devices for detection of motion [2]. In comparison, *nanoscale* magnetic sensing structures are typically very simple. One popular magnetic sensing technique, called magnetomotive detection, simply uses the Faraday effect of a nanoscale wire moving in a strong field of a magnetic source [16]. The main drawback of the magnetomotive technique is the need for a large magnetic field, which is usually created by a superconducting solenoid. Nevertheless, magnetomotive detection and its associated actuation technique are simple to use, feature low power consumption, and have been demonstrated to work at frequencies above 1 GHz [17].

The piezoresistive effect in doped silicon and metals forms the basis of another popular detection technique in microscale devices [2]. Semiconductor piezoresistive devices, usually made of doped silicon, offer very high sensitivity, but are more difficult to fabricate. The sensitivity of metal piezoresistors is lower, but this is compensated by the simplicity of fabrication and ease of impedance matching at high frequencies due to their intrinsically lower resistance. Importantly for nanoscale devices, piezoresistive detection in general and piezoresistive detection using metal piezoresistors in particular, scale very favorably to smaller dimensions. In addition, piezoresistive NEMS have the advantages of being fully integrated sensors that operate from room temperature down to at least 4 K and do not require a magnetic field. The main drawback of piezoresistive detection lies in its relatively high power consumption, which limits the usefulness of piezoresistive devices at cryogenic temperatures.

Figure 1.1 shows the schematics of the four popular detection schemes described above. Ad-

[2] One way to address this challenge is by doing careful on-chip impedance matching [15], tuning the detection circuit to the particular frequency range of the detected resonator.

ditional techniques of detecting nanoscale motion are based on motional changes in the tunneling barrier of a quantum point contact [18], the gate voltage of a single electron transistor [10, 11, 12], and the conductivity of individual nanotubes [19, 20]. As of this writing, these techniques primarily address niche applications and are not as widespread. In this chapter I will focus on piezoresistive detection and its downmixing variant, which we have developed for measuring high-frequency NEMS devices.

1.1 Piezoresistive detection using semiconductors and metals

When a resistor is deformed by applying an external stress, its resistance generally changes, a phenomenon known as the piezoresistive effect. The effectiveness of this strain-resistance transduction mechanism is characterized by the gauge factor of the piezoresistor, defined as $G = \frac{\Delta R/R}{\epsilon}$, where $\Delta R/R$ is the relative change in the device's resistance and ϵ is the strain component of interest. The change in piezoresistor's resistance is caused by two mechanisms: a change in its shape and a change in the resistivity of piezoresistor's material. Correspondingly, the gauge factor can be written as

$$G = (1 + 2\mu) + (\partial\rho/\partial\epsilon), \tag{1.1}$$

where μ is the piezoresistive material's Poisson ratio and ρ is its resistivity.

For metals, the geometrical contribution usually dominates and the change in resistivity can be neglected, which leads to $G = (1 + 2\mu) \sim 2$. Conversely, in doped semiconductors, the changes in resistivity plays the dominant role and the geometric contribution can be neglected. In semiconductors, the changes in resistivity are caused by the carrier transfer mechanism and changes in the effective mass of carriers, both a consequence of the deformation of the band-gap structure [21]. The typical gauge factors of doped semiconductor materials used in piezoresistive gauges vary between a few dozen to over one hundred.

Piezoresistive strain sensors have been previously integrated directly into microscale cantilevers [22, 23] and have been used, for example, in atomic force microscopy [22], data storage [24, 25], and

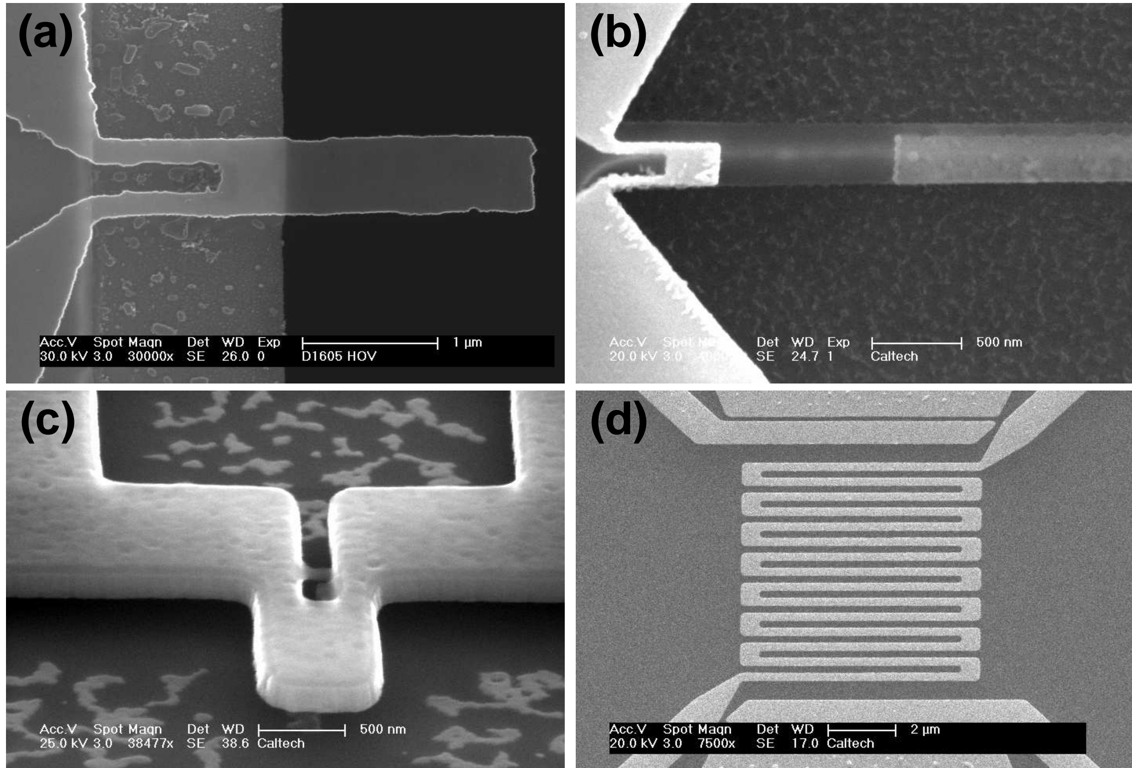

Figure 1.2: Typical geometries of piezoresistive devices. (a) Silicon cantilever with integrated piezoresistor. Only the top p-doped layer conducts electricity. (b) Gold piezoresistor on one side of a suspended silicon-carbide doubly clamped beam. (c) Suspended silicon cantilever with integrated metal piezoresistor, made of $Al_{0.96}Si_{0.04}$ alloy (fabricated at LETI, Grenoble, France). (d) Patterned multiple-loop piezoresistor for integration in plate-type resonators.

biosensing [26, 27]. These devices achieved great strain sensitivity by using semiconductor-based piezoresistors, primarily doped Si [21] or AlGaAs [28]. Resonance detection of cantilevers up to 9 MHz has been previously achieved using doped Si piezoresistors [24].

A typical piezoresistive detector consists of a single conducting loop or multiple loops preferentially oriented in the direction of the detected strain, usually along the length of the resonator. In our experiments, we used both metal and semiconductor piezoresistors. Figure 1.2 shows the geometries we used. The use of metal rather than semiconductor piezoresistors in nanoscale resonators has been recently pioneered in the Roukes group [5, 29]. While semiconductors often boast a gauge factor of over one hundred, gauge factors of metal piezoresistors are much lower, typically about two. Nevertheless, metal piezoresistors can overcome this large handicap in gauge factor by offering a number of other advantages. One such advantage is the ease of fabrication. Patterned thin metal

films are among the simplest nanostructures to fabricate. In addition, films of inert metals, such as gold or palladium, are generally very robust with respect to necessary additional fabrication steps, such as lithography and etching.

Another important advantage of metal piezoresistors is their low resistance—no more than a few hundred Ohm in our experiments, compared to 5–100 kΩ or more for semiconductor piezoresistors. The high resistance of semiconductor devices not only results in large Johnson noise but also leads to frequency-dependent signal attenuation at MHz frequencies if the conventional direct-current (DC) biasing is used. The piezoresistive downmixing technique described in the next section alleviates this problem of signal attenuation, but using low-resistance metal piezoresistors allows one to avoid it altogether.

The final argument in favor of metal piezoresistors is the significant reduction in $1/f$ noise. In resistors, including piezoresistors, the spectral density of the resistance fluctuations usually obeys Hooge's relation, $S_{1/f}(f) = \frac{R^2\zeta}{Nf}$, where R is the resistance, f is the frequency, N is the total number of mobile charge carriers, and the parameter ζ characterizes the resistor material [30]. The parameter ζ is of the same order of magnitude in metals and semiconductors [31], but the number of carriers in metals is larger by several orders of magnitude. As a result, the $1/f$ noise in piezoresistors becomes important only at frequencies below the corner frequency of $\sim$ 10 Hz [32], far below the typical resonance frequencies of nanomechanical resonators.

1.2 Piezoresistive downmixing[3]

Figure 1.3 shows the conventional low-frequency circuit for measuring piezoresistive devices. The piezoresistor R_c is placed in a bridge or half-bridge configuration with a fixed dummy resistor R_d; for simplicity we will assume $R_c = R_d = R$ when the NEMS is at rest. The ends of the resistors are oppositely DC-biased at $+V_b/2$ and $-V_b/2$, so that the voltage at the bridge point is zero when the NEMS is not moving. When the NEMS is driven at a frequency ω_d, R_c gains a time-dependent component: $R_c = R + \Delta R \cos(\omega_d t + \phi)$; typically $\Delta R/R \leq 10^{-5}$. This resistance variation produces

[3] Measurements described in this section were performed in collaboration with E.B. Myers.

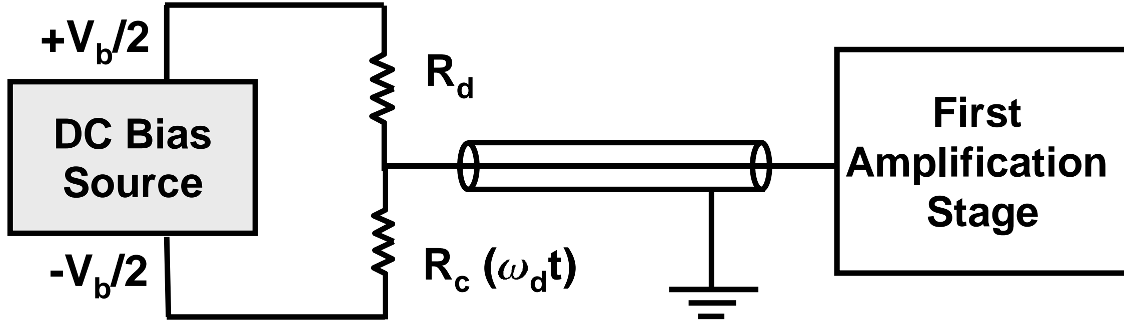

Figure 1.3: Direct-current piezoresistive readout schematic. A DC bias V_b is applied to the NEMS resistor R_c and dummy resistor R_d. The parasitic capacitance C_{par} across the amplifier input, combined with the resistors, filter the AC output voltage at high frequencies.

the standard resistance-bridge voltage $V_{out} \approx V_b(\Delta R/4R)\cos(\omega_d t + \phi)$ at the bridge point.

To measure V_{out} the bridge output must be connected in some way to a circuit, e.g., the input of a high-input-impedance preamplifier. At moderately high frequencies ($<$ 30 MHz), this introduces capacitances C_{par} to ground in parallel with the cantilever and dummy, effectively forming a low-pass filter with a cut-off frequency of $(\pi R C_{par})^{-1}$. With typical amplifier-input and cable capacitances $C_{par} \geq 50$ pF, and $R \geq 10$ kΩ, the AC output is strongly attenuated at $\omega_d/2\pi > 400$ kHz. At very high frequencies ($>$ 30 MHz), the measurements are further complicated by cable resonances. The conventional direct-current technique is, therefore, not suitable for measurements of NEMS devices, whose frequencies are in the MHz or even GHz range.

To address these difficulties, we have developed the piezoresistive downmixing scheme. Our technique utilizes AC biasing and the intrinsic properties of the piezoresistor to perform heterodyne downmixing of the signal to a much lower frequency, which can then be detected by standard circuitry without significant signal loss. Not only does this increase the detected signal, it also greatly reduces unwanted background from the cross-talk between the detector and actuator circuits. As proof of principle, we have applied this downmixing scheme to the detection of cantilever NEMS with fundamental mode frequencies of 5–25 MHz. We achieve thermal noise-limited detection of mechanical resonances in these devices at room temperature, demonstrating the ultimate sensitivity of downmixed piezoresistive signal detection in resonant high-frequency NEMS applications.

Our circuit, depicted in Figure 1.4, uses the piezoresistor to downmix the displacement signal

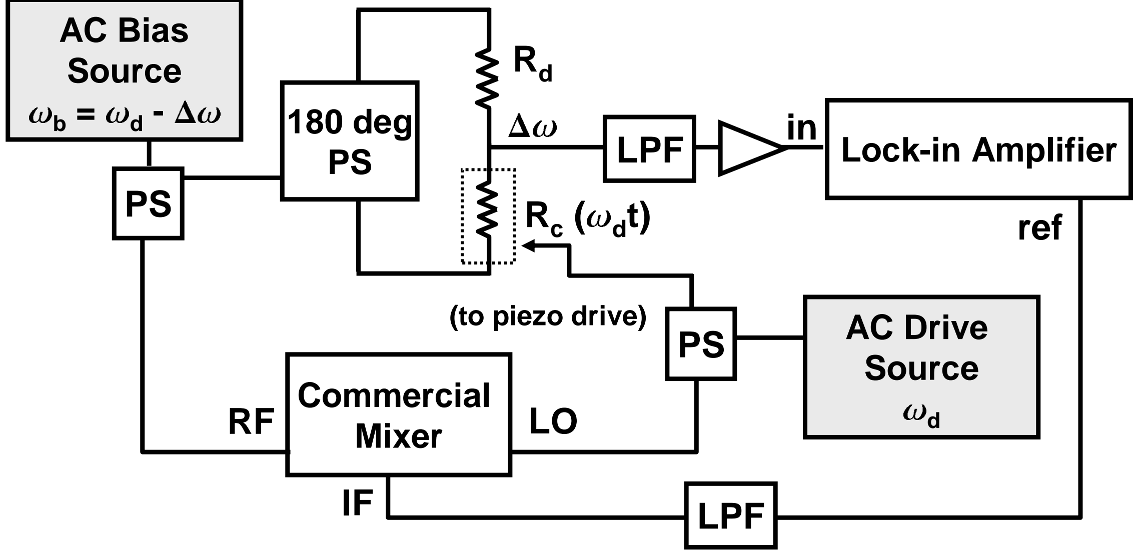

Figure 1.4: Diagram of downmixing circuit. The NEMS (within the dotted lines) is actuated by an AC source at frequency ω_d. A second AC source at frequency ω_b is used to apply balanced biasing to the resistors. The resulting downmixed output is sent through a low-pass filter (LPF), amplified, and fed into a lock-in amplifier. Power splitters (PS) and a commercial mixer are used to create a downmixed reference for the lock-in.

to a lower frequency. This is achieved by applying an AC voltage $V_b(t) = V_{b0}\cos(\omega_b t)$ across the resistors at a frequency ω_b, offset from the drive frequency by an amount $\Delta\omega \equiv \omega_d - \omega_b$. Using a 180° power splitter (PS), the voltage is applied oppositely to the ends of the resistors, to null the bias voltage at the bridge point [33]. The bias produces an AC current $I(t) = V_{b0}\cos(\omega_b t)/(R_d + R_c)$; to leading order in $\Delta R/R$, V_{out} then becomes

$$\begin{aligned} V_{out}(t) &\approx \frac{V_{b0}\cos(\omega_b t)}{4R}\left(\Delta R\cos(\omega_d t + \phi)\right) \\ &= V_{b0}\frac{\Delta R}{8R}\left[\cos(\Delta\omega t + \phi) + \cos\left((2\omega_d - \Delta\omega)t + \phi\right)\right]. \end{aligned}$$

Thus the output signal at the bridge point contains two frequency components, at the sum and difference of the drive and bias frequencies. With $\Delta\omega$ sufficiently small (< 100 kHz), the downmixed frequency component is attenuated minimally by the parallel capacitances. The output is then sent through a low-pass filter (LPF) to remove the upper sideband and any residual carrier, amplified, and finally fed into a lock-in amplifier for detection. The lock-in reference is generated by splitting off the bias and drive voltages with power splitters and sending the voltages into a commercial mixer,

which generates a downmixed signal in parallel with the NEMS.

This electromechanical downmixing effect, while functionally similar to that of commercial diode-based mixers, is a fully linear property of the piezoresistor. Unlike regular mixers, where a minimum threshold signal is required to access the nonlinear response, the piezoresistor downconverts any signal to an amplitude half that of the signal that would be generated with a DC bias of the same magnitude. In contrast, any parasitic cross-talk signal from the actuation circuit would need to pass through an element with a nonlinear I–V response in order to mix with the bias voltage down to the frequency $\Delta\omega$. We have found that the I–V nonlinearity of our piezoresistors is quite small, so that even extremely weak displacement signals can be downmixed and extracted from the device with minimal attenuation and background.

We have tested this downmixing scheme using high-frequency piezoresistive cantilevers as the NEMS device. The cantilevers are fabricated from silicon-on-insulator (SOI) wafers, where the top Si layer consists of 80 nm Si plus a 30 nm layer of boron-doped p-Si to act as the piezoresistive strain sensor. The cantilevers were fabricated in a manner similar to that of Harley and Kenny [23], where a backside KOH etch suspends the top Si layer as a membrane, and a combination of electron beam lithography, liftoff, and fluorine/chlorine-based plasma etching steps forms the cantilever from the membrane. The particular details of the fabrication method are described in an earlier publication [27]. A typical cantilever is shown in Figure 1.5(a); lengths ranged from 2–3 μm and widths were approximately 700 nm. As shown in Figure (1.5)(b), the dummy resistor was fabricated on-chip using the same p-Si material that provides the cantilever strain sensor, in order to minimize parallel capacitances. The cantilever and dummy resistances varied from device to device, and were in the range of 50–150 kΩ. The cantilever chip was mounted onto a piezoelectric ceramic actuator disk with a thickness of approximately 80 μm, corresponding to a thickness-mode resonance frequency of about 25 MHz. This assembly was in turn mounted onto a circuit board and placed into a vacuum chamber for measurements at room temperature.

Figure 1.6(a) displays a resonance curve for a 1.7-μm-long cantilever using our downmixing method. Here $V_{b0} = 3$ V, $\Delta\omega/2\pi = 100$ kHz, and a peak-to-peak voltage of 1.9 V is applied to

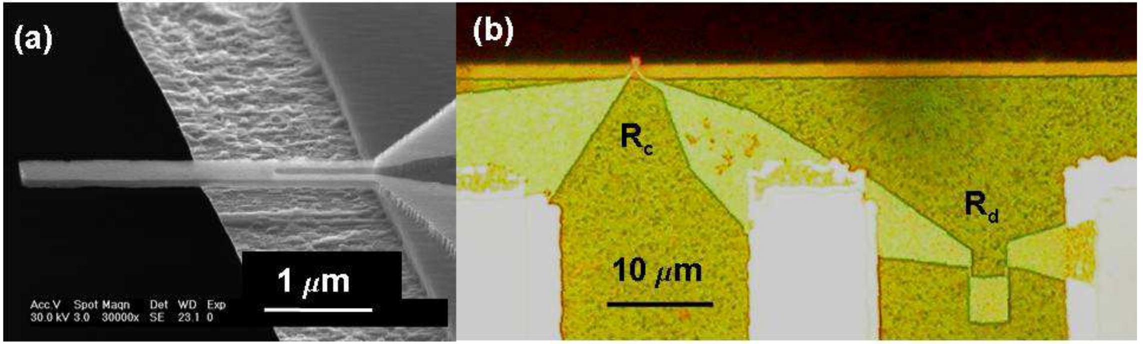

Figure 1.5: (a) Scanning electron micrograph of a cantilever of dimensions 3.2 μm long x 700 nm wide x 110 nm thick. (b) optical micrograph of a cantilever and dummy resistor. Three gold leads at the bottom of the image connect the resistors to the rest of the circuit.

the piezo actuator. The resonance is approximately $f_c = 24.4$ MHz, close to but somewhat below the theoretically predicted fundamental-mode resonance frequency of 27 MHz. The square of the voltage signal is proportional to the energy in the cantilever; fitting this quantity to a Lorentzian yields a width of 18.2 kHz, implying a quality factor of $Q \approx 1300$. For comparison, Figure 1.6(b) shows the same cantilever resonance measured in the standard DC half-bridge configuration [22], using a DC bias of 5 V across R_c and R_d and a 50 Ohm, high-frequency network analyzer for drive (approximately 1 V_{pp}) and detection. In both measurements no impedance matching had been performed, and the signal was normalized by the drive and bias levels. The resonant signal in the downmixing scheme is approximately 1000 times larger than in the direct measurement scheme. In addition, the relative magnitude of the background, caused by parasitic coupling of the drive signal to the detection circuit, is nearly three orders of magnitude smaller in the downmixing case. As a result, the downmixed resonance is essentially Lorentzian, while the network analyzer resonance is highly distorted.

This technique is sensitive enough to detect the thermomechanical fluctuations of the cantilever when it is not driven externally. This is done by applying only a bias voltage and, while sweeping the bias, detecting narrowband noise at the offset frequency $\Delta\omega$. Figure 1.7 shows the thermomechanical noise for a 2.6-μm-long cantilever with fundamental mode frequency $f_c = 11.9$ MHz, using $\Delta\omega/2\pi = 50$ kHz. The noise appears as two peaks spaced 100 kHz apart because the noise in the

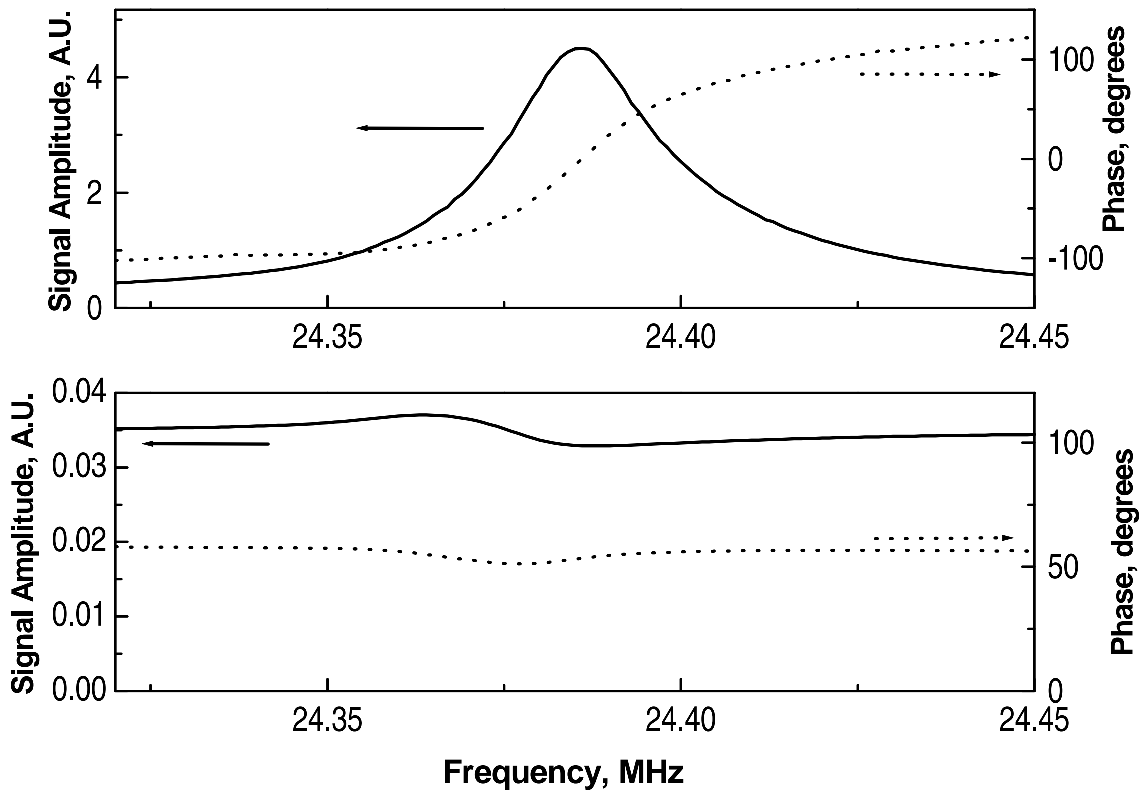

Figure 1.6: (a) Signal amplitude (solid line) and phase (dotted line) of resonance of first vibration mode of a 1.7-μm-long cantilever, as measured using downconversion, using an offset frequency $\Delta\omega/2\pi = 100$ kHz. The amplitude is normalized to the drive and bias levels. (b) Signal amplitude and phase as measured directly with a network analyzer.

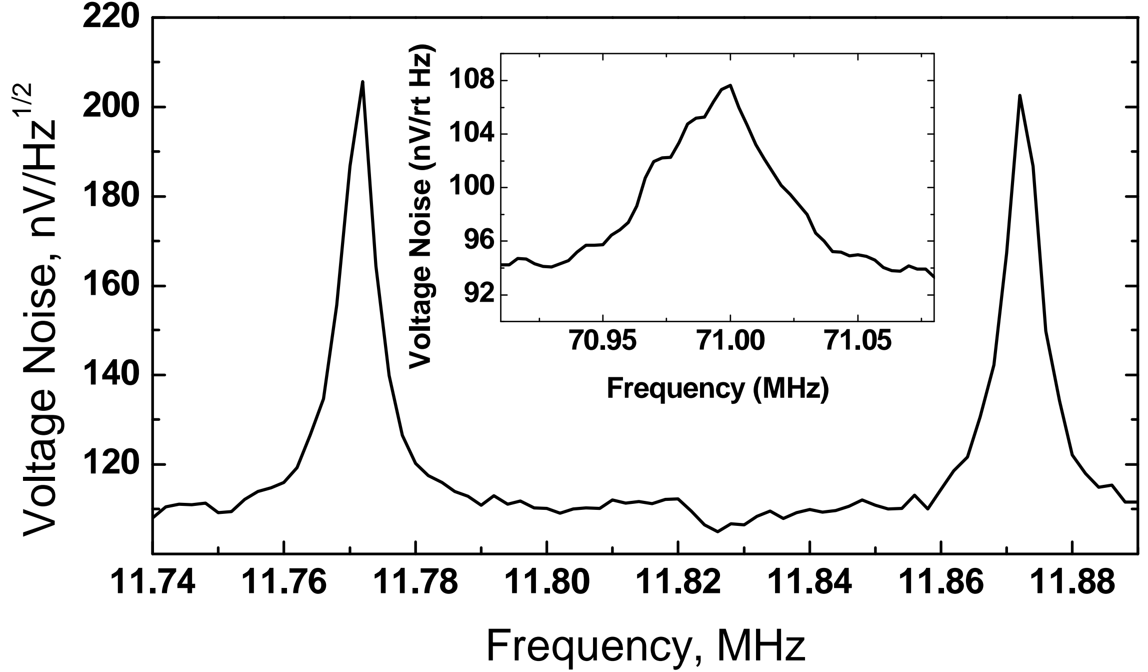

Figure 1.7: Thermomechanical noise peaks from the fundamental vibration mode of a 2.6-μm-long cantilever. Inset: One of the thermomechanical noise peaks from the second vibration mode of the same cantilever.

cantilever at the resonance frequency is mixed to the 50 kHz reference when the bias is either 50 kHz above or below the cantilever resonance. The peak noise amplitude agrees with the theoretical estimate based on the previously measured piezoresistive gauge factor of similar cantilever devices [27]. Note that the thermal conduction calculations predict the cantilever to be approximately 20 K hotter than the room-temperature environment due to Joule heating of the piezoresistor in this experiment. The off-resonance noise floor of 110 nV/$\sqrt{\text{Hz}}$ is approximately twice that expected from a combination of thermomechanical noise and Johnson noise (the preamplifier input noise, at 0.6 nV/$\sqrt{\text{Hz}}$, is negligible). The precise origin of this excess noise is unclear; however, we have found that we can reduce the noise floor to the expected Johnson noise level ($\sim$ 60 nV/$\sqrt{\text{Hz}}$) by increasing the offset frequency and decreasing the bias voltage, while still maintaining the visibility of the thermomechanical noise peak on resonance. We note by comparison that our network analyzer measurement has input-referred noise amplitude of about 7 nV/$\sqrt{\text{Hz}}$. The thermomechanical noise peak, attenuated by more than three orders of magnitude because of the low 50 Ohm input impedance of the network analyzer, would be nearly undetectable against this background.

The fact that the peak noise amplitude in Figure 1.7 is about twice larger than the off-resonant noise floor allows us to conclude that the thermal excitation is the main source of noise in resonant experiments with this device. The corresponding force sensitivity can be calculated [34] by using a value of the spring constant $k \approx 0.5$ N/m determined from the device dimensions and the elastic properties of Si [22]; when Johnson noise is included, the overall resonant force sensitivity at 11.9 MHz is $F_N \approx 350$ aN/$\sqrt{\text{Hz}}$ at room temperature, comparable to the lower-frequency cantilever devices studied previously [23].

The thermomechanical noise peak remains visible in the downmixed scheme at even higher frequencies, as demonstrated by detection of the thermal noise peak from the second vibration mode of the 11.9 MHz cantilever (inset to Figure 1.7), whose driven resonance we have detected at approximately 71 MHz. This demonstrates that the technique as presented here is viable for even smaller NEMS whose fundamental modes lie in the VHF range.

Chapter 2

Actuation techniques for nanomechanical resonators

As with detection, there are a number of techniques for actuating nanoscale mechanical resonators, each with its own advantages and disadvantages. In the field of MEMS, the most popular actuation techniques are capacitive, thermoelastic, piezoelectric, and magnetic. All of these techniques—in adapted form—have been used in nanoscale devices.

Piezoelectric actuation of nanoscale oscillators can take two forms: inertial actuation using a macroscopic piezoshaker; and direct piezoelectric actuation using an integrated micro- or nanoscale piezoelectric actuator. Piezoshaker actuation is often the easiest actuation mechanism to implement and is widely used for lower-frequency devices. Integrated piezoelectric actuation of multilayer GaAs cantilevers and beams, which uses the piezoelectric properties of GaAs itself, has recently been demonstrated in Ref. [36]. Integrating bimorph piezoelectric actuators into other types of resonators remains challenging, but holds the promise of highly efficient low-power actuation for nanoscale resonators in the high-frequency range and above.

Capacitive actuation uses the attractive force existing between two electrodes of a charged capacitor. If the attractive force is modulated by applying an AC voltage to the opposing electrodes, this force can be effectively used to drive the motion of a nanoscale resonator. Capacitive actuation is relatively simple to realize and has the advantage of low power dissipation. It has been demonstrated for both semiconductor-material NEMS devices [15] and more exotic mechanical oscillators like carbon nanotubes [19, 20].

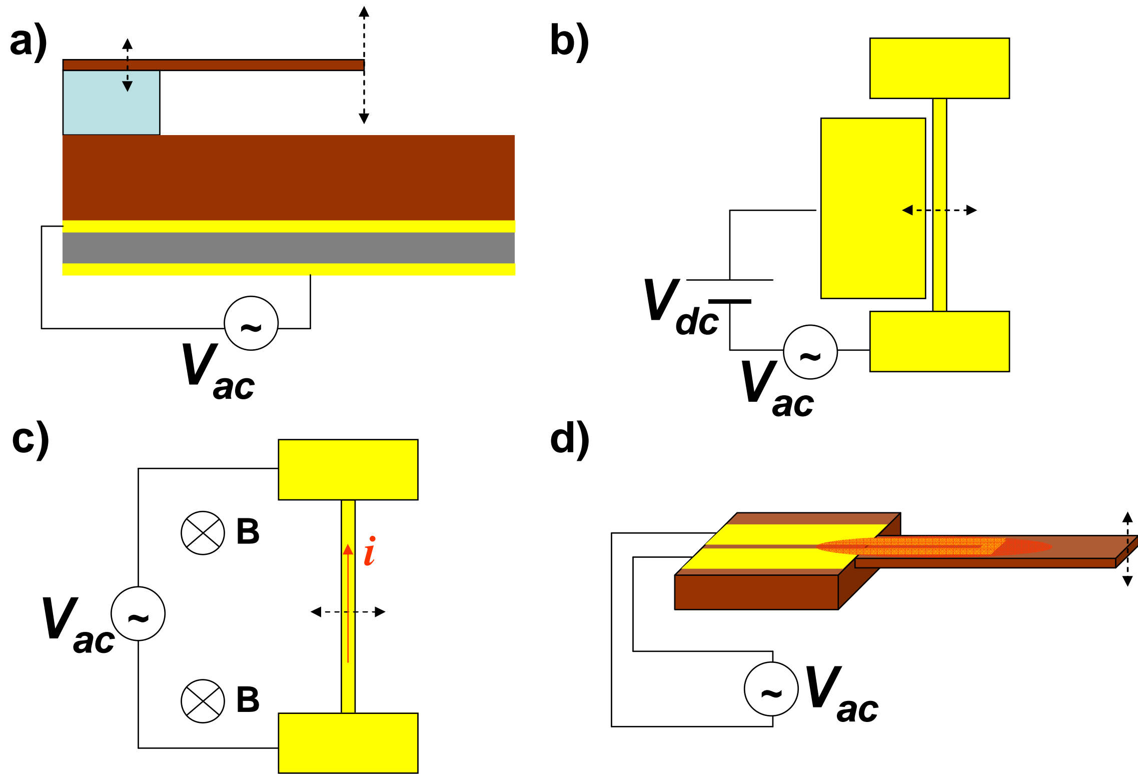

Figure 2.1: Common actuation schemes for nanoscale devices. (a) Schematic side view of a typical inertial piezoshaker actuation setup. AC voltage applied to the piezoshaker induces the motion of the entire cantilever chip. In the moving frame of the cantilever chip, a periodic inertial force acts on the cantilever's center of mass and drives its motion. Both in-plane and out-of-plane cantilever motion can be excited in this way. The range of motion of the cantilever tip typically exceeds that of the cantilever base by a factor on the order of Q, the resonator's quality factor. (b) Schematic top view of the capacitive actuation technique. The beam and the side gate form the opposing electrodes of a capacitor. The electrostatic attractive force between these electrodes can be modulated by the applied AC voltage which drives the in-plane motion of the cantilever. (c) Schematic top view of the magnetomotive detection technique. Applied AC voltage drives periodic current i through the beam, which leads to a periodic Lorentz force in the external magnetic field B. Depending on the orientation of the static magnetic field, both in-plane and out-of-plane cantilever motion can be driven this way. (d) Schematic view of the electrothermal actuation technique. The Joule heating due to applied AC voltage induces periodic changes in the temperature of the cantilever base. The difference in the temperature coefficient of linear expansion causes the bilayer structure to flex, driving the periodic motion of the cantilever.

Magnetomotive actuation uses the Lorentz force acting on a conducting wire with a current in a static magnetic field. This technique usually employs a superconducting solenoid at cryogenic temperatures [16] and is often combined with magnetomotive detection, i. e., the measurement of the Faraday voltage generated by a moving loop in a static magnetic field. This combined magnetomotive actuation-detection scheme has been been used to detect mechanical resonances at frequencies up to 1 GHz [17], but it becomes increasingly difficult to push this actuation technique to even higher frequencies. Although most magnetomotive actuation and detection experiments have been done at cryogenic temperatures, this technique has been shown to work in the field of a permanent magnet at room temperature as well [37, 38].

Thermoelastic actuation uses the difference in the coefficients of linear expansion of different materials, and, similarly to macro-scale applications, usually employs a bimorph structure. The heating needed for thermoelastic actuation can be provided by intense light, which is known as photothermal actuation, or electricity, known as electrothermal actuation. Photothermal actuation has been successfully used in both micro- and nanoscale devices [39, 40, 41], usually in combination with optical detection. Electrothermal actuation has been used extensively in microscale devices [2, 42, 43] but not in nanoscale devices prior to the work described in this thesis.

Figure 2.1 shows the schematics of the four popular actuation schemes described above. In my studies, I used three of them: inertial actuation with a piezoshaker, magnetomotive actuation in the field of a permanent magnet, and electrothermal actuation. They will be considered in more detail in the following sections.

2.1 Piezoshaker actuation

Conceptually, piezoshaker actuation is probably the simplest actuation technique: the NEMS chip is physically shaken by applying periodic voltage to a piezoelectric actuator (piezoshaker). Figure 2.1(a) shows a typical setup using piezoshaker actuation. In the moving frame of the chip, inertial forces act on the center of mass of the cantilever, creating a periodic drive that excites the resonance. If the quality factor of the resonator is large, $Q \gg 1$, the amplitude of motion on

resonance is given by

$$a_{res} = Q\frac{F_{in}}{k_{eff}} = Q\frac{m_{eff}z_s\omega_R^2}{m_{eff}\omega_R^2} = Qz_s,$$

where F_{in} is the inertial force acting on the center of mass of the cantilever, k_{eff} is its effective spring constant, m_{eff} is its effective mass, ω_R is its resonance frequency, and z_s is the amplitude of motion of the substrate surface at the clamping point of the resonator.

Depending on the parameters of the resonator, a piezoshaker may or may not be convenient to use in practice. Generally, piezoshaker actuation is very convenient for low resonance frequencies, typically below 1 MHz. At these frequencies, the piezoshaker motion is usually quasi-static, i. e., the displacement amplitude for a given applied voltage is uniform across the shaker surface and is equal to the static displacement for this voltage. Above a certain characteristic frequency, however, acoustic resonances of the piezoshaker element and the NEMS chip itself become important. This characteristic frequency is determined by the typical dimensions of used silicon chips and piezoshaker (a few millimeters) and the typical speed of sound in solid materials (a few kilometers per second), resulting in the typical acoustic resonance frequencies of $\sim$ 1 MHz.[1] Above these frequencies, the dynamics of piezoshaker displacement is no longer quasi-static. In order to understand it, it is more appropriate to think of ultrasound waves propagating inside the shaker and the substrate. These ultrasound waves will undergo multiple reflections and refractions inside the piezoactuator, the NEMS chip, and the glue between them. The interference of these waves will result in a complicated spatial and frequency dependence of the amplitude z_s of the periodic vertical motion on the chip surface.

As a result of multiple-wave ultrasound interference, the drive z_s will vary as a function of frequency on some characteristic scale $\Delta\omega_{ch}$. If the width of the measured resonance ω_R/Q is smaller than this characteristic scale, $\Delta\omega_{ch}$, the drive z_s may be approximately constant over the narrow range of frequencies used to measure the resonance. The resonance curve will then look like a well-behaved Lorentzian. Conversely, if the width of the resonance is larger than the characteristic scale,

[1] In our experiments, we tried to maximize this frequency by using the smallest available piezoshaker actuators, manufactured by TRS Technologies, Inc (State College, PA). The typical actuators we used were single-crystal discs a few millimeters in diameter and approximately 100 microns thick.

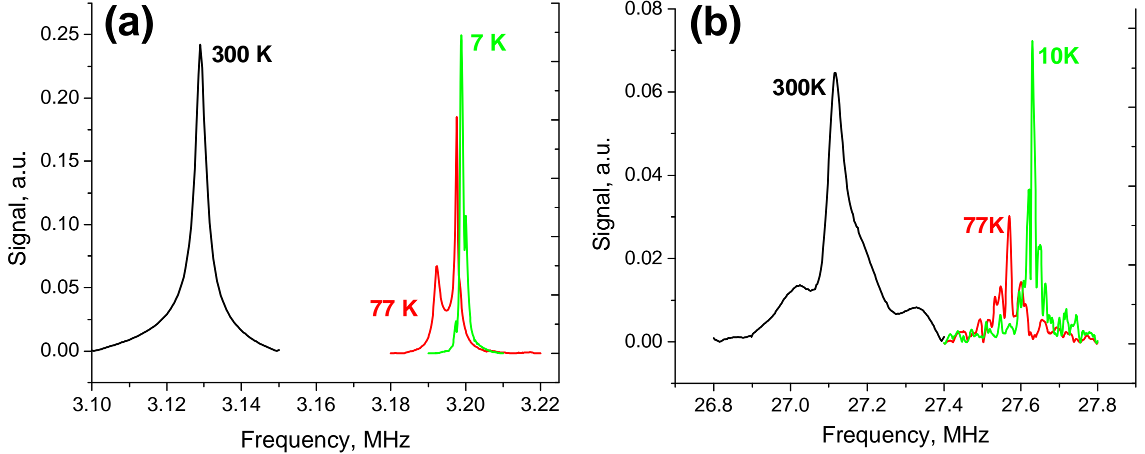

Figure 2.2: Resonance curves of the first (a) and second (b) mode of a 4-μm-long silicon cantilever (device no. 27-7) obtained using piezoshaker actuation. The measurements were done in vacuum at room (300 K), liquid nitrogen (77 K), and liquid helium temperatures (10 K).

the resonance curve will be severely distorted. Figures 2.2 illustrate these situations using the resonance curves of a 4-μm-long silicon piezoresistive cantilever. The room-temperature resonance curve of the fundamental mode in Figure 2.2(a) looks more or less like a normal Lorentzian peak because it is narrow enough that we can ignore the frequency dependence of the drive. However, the same does not apply to the second mode of the device shown in Figure 2.2(b). The peak becomes distorted as it is modulated by the varying amplitude of the drive. These distortions become even more obvious at cryogenic temperatures even though the width of the mechanical resonances generally becomes smaller at low temperatures (due to increasing quality factor). Evidently, the frequency dependence of the piezoshaker drive amplitude features even more rapid variations at cryogenic temperatures than at room temperature. This is probably due to the fact that acoustic resonances inside the piezoshaker and the resonator chip have higher quality factors at low temperatures, which results in a sharper dependence of drive on frequency.

We obtained additional information about the frequency dependence of the piezoshaker drive by tuning the frequency of the mechanical resonance. Absorptive tuning at liquid helium temperatures, described in Section 3.2, was the most convenient way to perform these measurements. The typical results are shown in Figure 2.3 in the form of a a density plot and a 3D plot. Both plots are simply collections of resonance curves taken one after the other as the frequency of the cantilever resonance

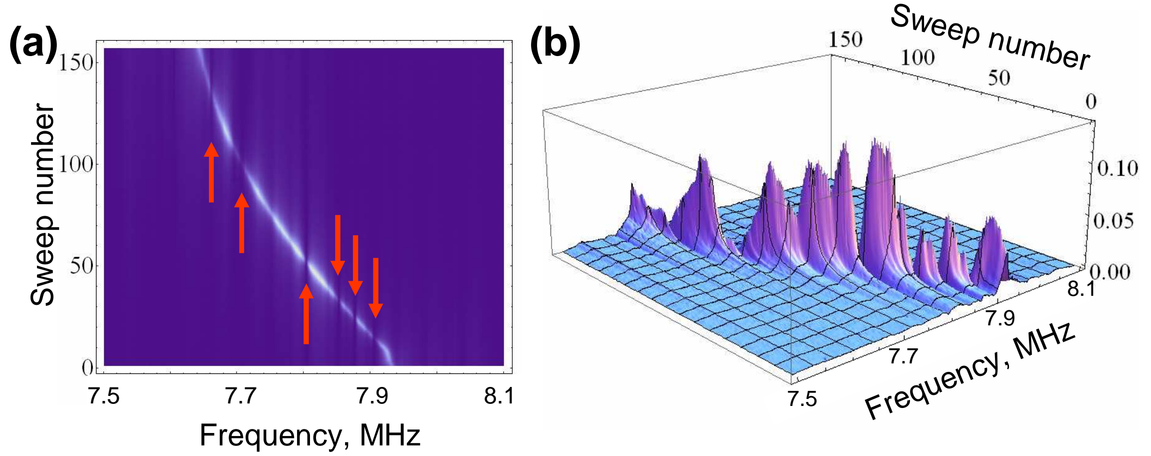

Figure 2.3: Density (a) and 3D (b) plots of cantilever resonance signal (device no. 23B8) obtained using piezoshaker actuation at a temperature of 10 K. Brighter points in the density plot correspond to higher cantilever amplitudes. The resonance curve was measured repeatedly as the frequency of the cantilever resonance was slowly tuned down using absorptive frequency tuning technique (Section 3.2). The red arrows indicate frequencies at which the piezoshaker drive apparently vanishes.

was continuously tuned down by the added mass of physisorbed nitrogen molecules. The broad bright streak in the density plot (Figure 2.3(a)) traces the resonance frequency of the cantilever as it monotonically decreased in time. The rate of frequency tuning was slow at the beginning, then was manually increased to a much larger value, and then continuously decreased due to natural adsorption-desorption dynamics.

It is clear that the resonance response of the cantilever does not follow a simple Lorentzian response but rather is modulated by the frequency-dependent amplitude of the drive z_s. In particular, at some frequencies the drive vanishes completely. Some of these frequencies are indicated by red arrows in Figure 2.3(a) and are also obvious in Figure 2.3(b). In between the frequencies of vanishing drive, the drive amplitude is not constant either, which can be seen from the varying height of peaks in Figure 2.3(b). Overall, these measurements support the explanation that the measured response is a product of the simple Lorentzian function and a rapidly varying function describing the frequency dependence of the piezoshaker drive z_s.

An illustration of the *spatial* variation of the piezoshaker drive was provided by another experiment in which I measured two nominally identical resonators situated approximately 200 μm away form each other on the same chip. The cantilevers were designed for studying in-plane modes and

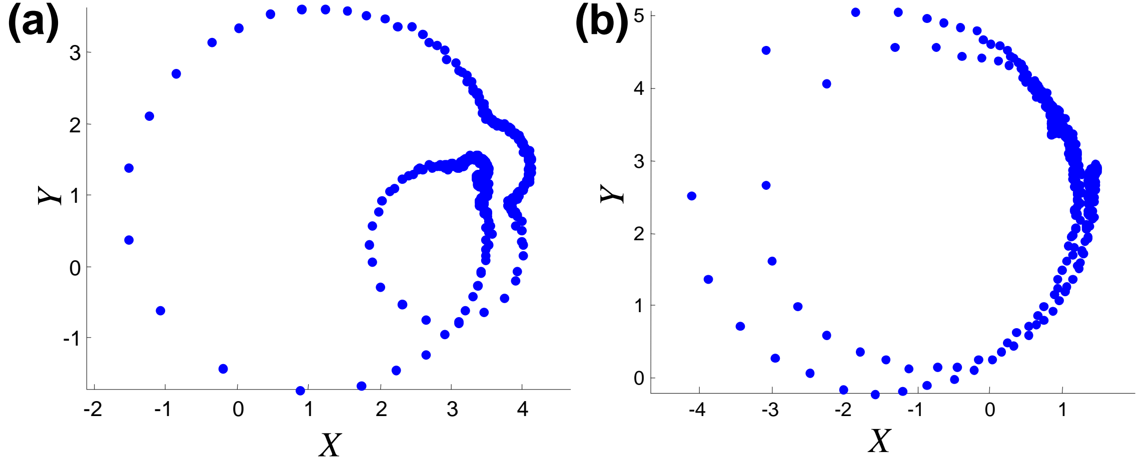

Figure 2.4: Parametric plots of X and Y quadratures obtained simultaneously from two in-plane resonators (devices nos. A1D1 and A1D3) using piezoshaker (a) and thermoelastic (b) actuation.

are described in more detail in Section 5.3. Even though the two resonators were nominally identical, their resonance frequencies were slightly different, 20.5 and 20.7 MHz. This difference in frequencies allowed us to measure the two devices in parallel while still observing a separate resonance peak for each resonator. Figure 2.4(a) shows the parametric plot of the measured X and Y quadratures of the signal obtained using piezoshaker actuation. For each resonance, such a parametric plot normally forms a circle (see Appendix A for more detail), and in fact there are two circles visible in Figure 2.4(a). However, the two circles have different diameters and are rotated with respect to each other, which means that the amplitudes and relative phases of the two resonances are quite different. This will happen if the phase and amplitude of the piezoshaker drive are different for the two resonators. In addition, the plots feature additional arc-like features on the right side of the plot which can be attributed to the acoustic resonances that produce frequency dependence of the piezoshaker drive.

There is an alternative explanation for the observed difference in the phase and amplitudes of the detected resonances: a difference in the properties of the resonators themselves. In other words, even though the two resonators were nominally identical, they could still produce different piezoresistive signals because of fabrication-related imperfections. Differences in the piezoresistor geometry may indeed introduce small differences in the amplitudes of the detected resonances, even if the drive is

the same, but it is difficult to imagine how these imperfections would affect the phase of the detected resonance.

I have also measured these devices using thermoelastic actuation (Section 2.3), with the results shown in Figure 2.4(b). In contrast to piezoshaker actuation, thermoelastic actuation is expected to be spatially phase-uniform. Accordingly, there is no noticeable differences in the phases of the two circles, nor are there any additional arc-like features in these parametric plots. The two circles have slightly different amplitudes, probably due to the fabrication imperfections. These measurements therefore support the hypothesis that the piezoshaker drive is highly non-uniform in both frequency and space in the typical frequency ranges of NEMS devices.

In summary, the piezoshaker drive is simple to realize but has many shortcomings, which limits its usefulness in high-frequency sensor applications, especially at low temperatures and for devices with low quality factors. This has motivated us to look for alternative methods of actuation described in the following sections.

2.2 Room-temperature magnetomotive actuation[2]

In the course of looking for alternatives to piezoshaker actuation, we have briefly studied room-temperature magnetomotive actuation. Magnetomotive actuation has been used extensively at liquid helium temperatures (see, for example, Refs. [4, 17, 16, 33]) and less often at room temperature [37, 38]. Typically, magnetomotive actuation is combined with magnetomotive detection so that the measurement can be done using a simple network analyzer. However, magnetomotive detection of nanoscale resonators usually requires a magnetic field $B_0 \geq 1$ Tesla, which is achieved either with a superconducting solenoid at cryogenic temperatures or with a carefully designed permanent-magnet system at room temperature. Such large fields are required because the magnetomotive detection voltage scales as $V_m \sim B_0 l \Delta x \omega_R$, where l is the length of the resonator beam, Δx is its maximum displacement, and ω_R is the resonance frequency. As the resonator gets smaller, the decreases in the length l and maximum displacement Δx typically dominate the increase in ω_R. As a result, a

[2]Measurements described in this section were performed in collaboration with I. Kozinsky.

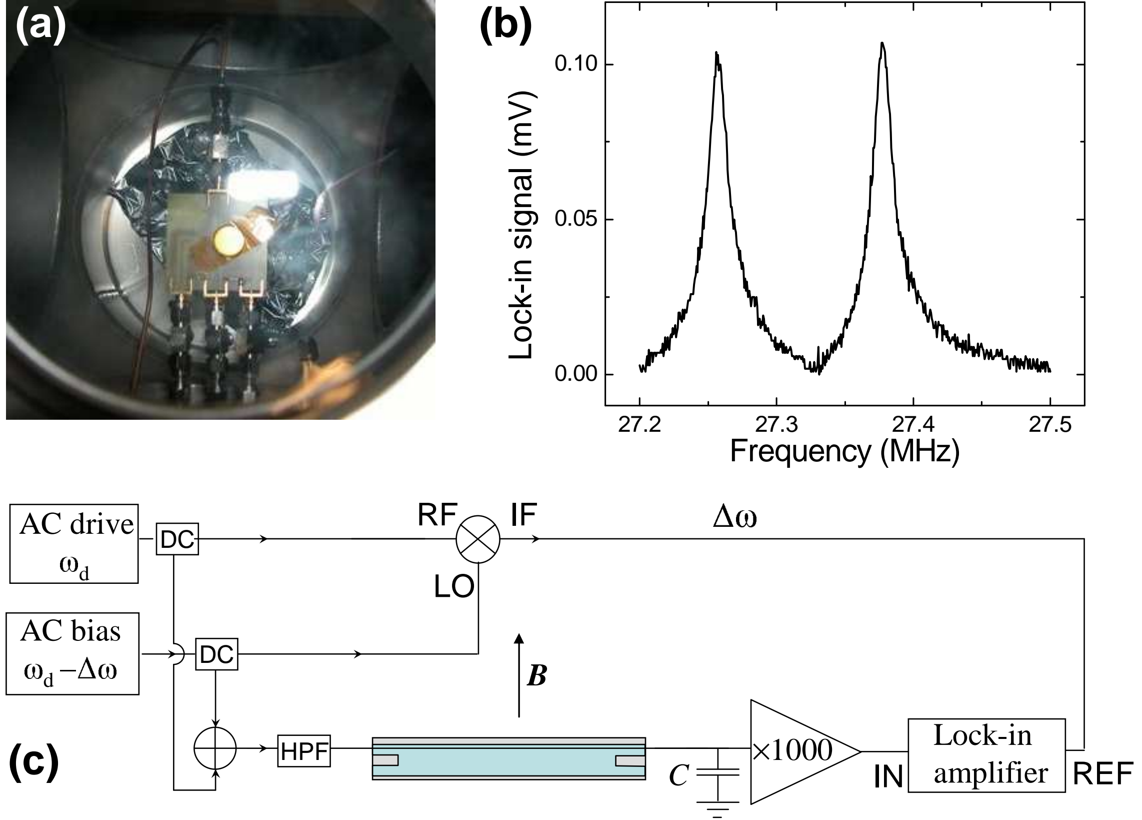

Figure 2.5: (a) Schematic of a magnetomotive actuation setup inside a room-temperature vacuum chamber. The bright circle in the center of the image is the permanent magnet. (b) Resonance signal of the fundamental in-plane mode obtained using magnetomotive actuation and piezoresistive detection. (c) Schematic of the setup using magnetomotive actuation and piezoresistive detection.

larger magnetic field is required to maintain the same voltage level of the signal.

Magnetomotive actuation of nanoscale resonators does not require such large magnetic fields because the actuating Lorentz force is given by $F_L = B_0 I l$, where I is the actuating current. Therefore, we can simply increase the current flowing through the device to compensate for a smaller length or field. Combining magnetomotive actuation with piezoresistive detection allowed us to use a compact cobalt-samarium permanent magnet with the saturation magnetization of 1 Tesla and magnetic field of ~ 0.1 Tesla at the location of the resonator.

The photograph in Figure 2.5(a) shows the circuit board with the resonator chip mounted upside down inside a room-temperature vacuum chamber. A cobalt-samarium permanent magnet was fixed on top of the circuit board with vacuum scotch tape. The position of the permanent magnet was deliberately off-center in order to create an in-plane field component at the location of the chip,

estimated to be approximately 0.1 Tesla (1 kilogauss).

Figure 2.5(c) shows the schematic of the electrical circuit used in these measurements. We used doubly clamped beams made of 100-nm-thick silicon carbide (SiC) structural layer with a 50-nm-thick gold-palladium film on top of the structural layer. The beams were similar to those used for magnetomotive measurements [45, 46] but had patterned legs on both ends of the beam, which allowed piezoresistive detection. The "bias" and "drive" currents were combined together using a power combiner and passed though the length of the beam. The Lorentz force acting on the resulting current in the external magnetic field induced out-of-plane motion of beams, which was detected using piezoresistive downmixing (Section 1.2).

Figure 2.5(b) shows the resonant peaks corresponding to the fundamental in-plane resonance of an 8.5-μm-long, 400-nm-wide beam. There are two peaks in the graph because the roles of the drive and AC bias are interchangeable in this setup. Therefore, a peak is observed when the resonance frequency equals either the drive frequency ω_d or the bias frequency $\omega_b = \omega_d - \Delta\omega_d$. In agreement with this explanation, the two peaks in Figure 2.5(b) are separated by the offset frequency, $\Delta\omega_d \approx 120$ kHz.

The combination of room-temperature magnetomotive actuation and piezoresistive detection described above was relatively easy to realize and does not require cryogenic temperatures or special permanent magnet setups. However, the need to mount a permanent magnet and the fact that each mechanical resonance produces two closely spaced peaks in this scheme is not always convenient. This motivated us to search for new, fully integrated ways of actuating nanomechanical resonators.

2.3 Thermoelastic actuation[3]

Thermoelastic actuation of bilayer structures has long been employed, for example, in thermostats [47], and relies on the fact that the coefficient of linear thermal expansion varies for different materials. For example, $\alpha_{Au} \approx 12 \times 10^{-6}$ K^{-1} and $\alpha_{SiC} \approx 4.8 \times 10^{-6}$ K^{-1} for gold and silicon carbide, respectively. Local heating of gold–silicon carbide bilayer that is integrated into a nanomechanical

[3]Measurements described in this section were performed in collaboration with I. Kozinsky.

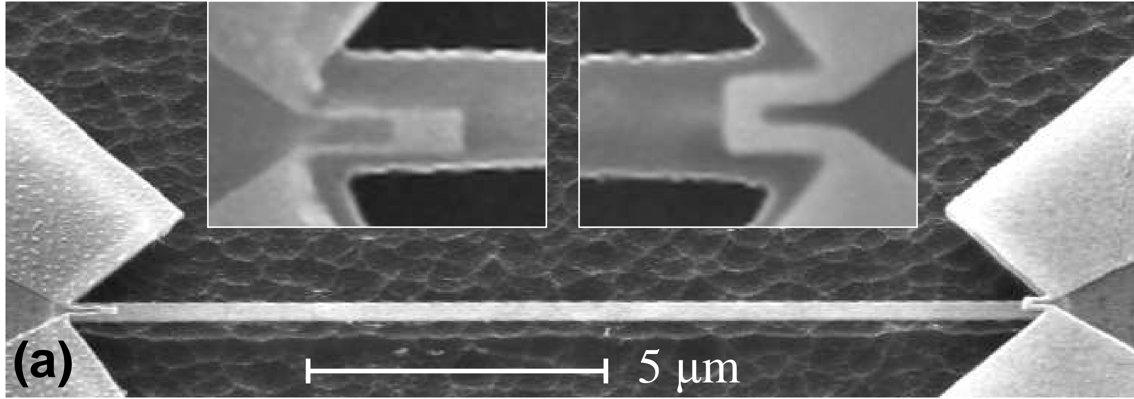

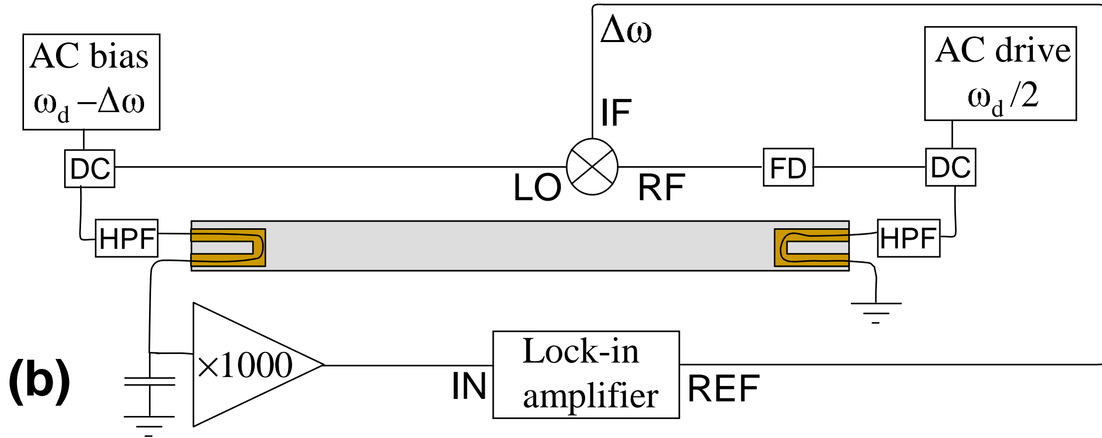

Figure 2.6: (a) Scanning electron micrograph of one of the devices used in the experiments (oblique view). The insets show top-view closeup images of the detection (left) and drive (right) metal loops. (b) Schematic of the experimental setup.

resonator therefore results in nonuniform expansion and thermal stresses that can flex the resonator. If the temperature changes periodically at the resonance frequency of one of the mechanical modes of the resonator, the amplitude of deflection will be greatly enhanced due to the large quality factors of nanomechanical resonators. The thermoelastic mechanism has been used previously to actuate microscale resonators by local Joule heating [42, 43] as well as NEMS resonators by local laser heating [39, 40, 41]. Most of these studies used optical detection. In contrast, we use piezoresistive downmixing detection, described earlier in Section 1.2, and thermoelastic actuation due to localized Joule heating of a metallic resistor. Our technique therefore offers the convenience of fully integrated, purely electronic actuation and detection, as well as the ability to detect dozens of vibrational resonances of the same NEMS structure, as shown below.

Figure 2.6(a) shows one of the doubly-clamped beam resonators used in the experiments. The

beams were made from a single-crystal silicon carbon (3C-SiC) thin film by multiple aligned steps of e-beam lithography, thin film evaporation, liftoff, and reactive plasma etching [45]. They had nominal lengths between 4 and 24 μm, a width of 400 nm, and a thickness of 80 nm. Two different thin metal film loops were patterned near the two ends of the beam. The 80-nm-thick, 100-nm-wide loop was patterned from thermally evaporated gold and formed a part of the thermoelastic bilayer actuator (right inset of Figure 2.6(a)). The thinner piezoresistor loop was patterned from a 30-nm-thick metal layer created by evaporating a 60%–40% gold-palladium alloy. It consisted of 250-nm-long, 50-nm-wide legs connected by a larger pad (left inset of Figure 2.6(a)). A 2-nm-thick chromium adhesion layer was used in both cases. Typical resistances of metal loops were 30 Ω for the actuation loop, and 300 Ω for the detection loop.

Figure 2.6(b) shows a schematic of the experimental setup. Periodic temperature variations at drive frequency, ω_d, are induced by applying a drive voltage at half the frequency, $\omega_d/2$, to the actuation loop. An AC bias voltage of frequency $\omega_d - \Delta\omega$ is applied to the detection loop on the other end of the beam. The downmixed signal voltage at frequency $\Delta\omega$ generated in the piezoresistor [44] is then amplified by a high-input-impedance preamplifier and detected with a lock-in amplifier. Fractions of the drive and bias signals are split off with directional couplers (DC) and fed to a broadband frequency doubler (FD) and mixer to produce the reference signal for the lock-in amplifier. Commercial 3 MHz high-pass filters (HPF), followed by 10 dB attenuators (not shown), are inserted in the bias and drive channels to reduce the parasitic background and noise in the detected signal.

Figure 2.7 shows the magnitude of the raw signal from a 16-μm-long beam detected as both the drive and bias voltages are swept over a very wide range of frequencies while keeping the downmixed frequency constant at 95 kHz. The large peaks correspond to the first eight out-of-plane flexural modes of the beam. The small peak near the second large peak corresponds to the first in-plane mode. On resonance, both quadratures of the lock-in signal fit the Lorentzian curve shape very well (inset of Figure 2.7). The noise floor of ≈ 3 nV/Hz$^{1/2}$ is largely due to the Johnson noise of the piezoresistor. The small background signal originates from the parasitic coupling between

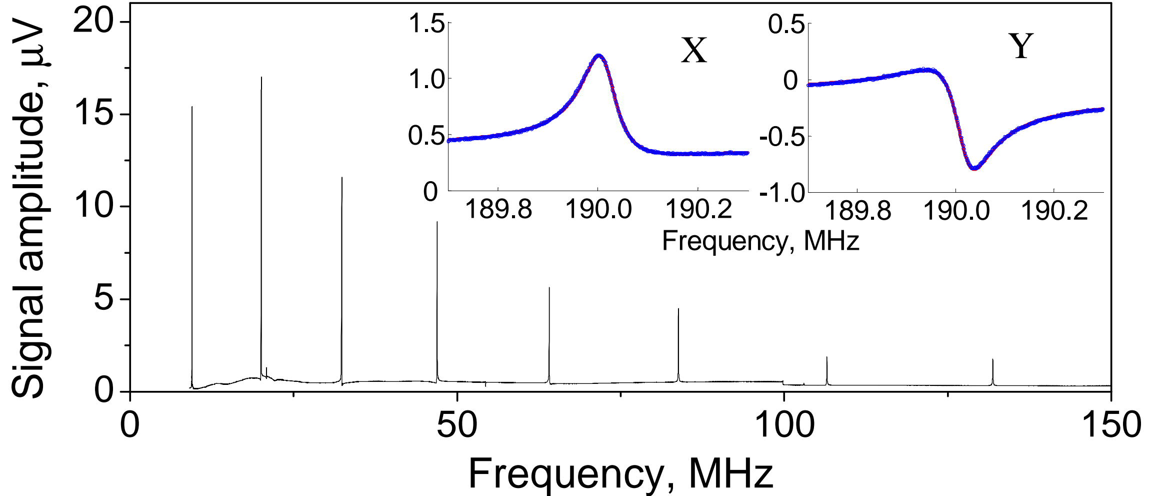

Figure 2.7: Raw signal, referred to the preamplifier input, from a 16-μm-long beam. The root-mean-square amplitudes of the drive and bias voltages are 22 mV and 118 mV, respectively. Inset shows both quadratures of the resonant response of the tenth out-of-plane mode (not shown in main panel) and the almost indistinguishable Lorentzian fit to the data.

bias, drive, and detection channels, and the slight nonlinearity of the piezoresistor and preamplifier response.

Table 2.1 lists the frequencies of the first seventeen vibrational modes of the 16-μm-long device predicted from FEMLAB finite element simulations, and also shows their measured frequencies and quality factors determined from Lorentzian fits. Discrepancies between predicted and observed frequencies do not exceed a few percent for all modes if the intrinsic strain, which presumably arises during fabrication of multilayer structures, is taken into account. The agreement is excellent for the lower modes and deteriorates slightly only for the highest modes. We attribute this to the difficulty of realistically modeling the imperfect clamping of our beams at their ends. We observe many more resonance peaks above the resonance frequency of the twelfth out-of-plane mode, up to a resonance at 1.094 GHz; however, these resonance peaks become progressively smaller and some of them overlap, which makes it difficult to identify the nature of the corresponding modes and fit the resonance peaks to Lorentzian curves.

As discussed in Section 1.1, the amplitude of the downmixed piezoresistive signal is approximately $V_s \approx V_b \Delta R/(2R) = V_b g \langle \epsilon_{xx} \rangle /2$, where V_b is the amplitude of the applied AC bias voltage, g is the effective gauge factor of the piezoresistor, and $\langle \epsilon_{xx} \rangle$ is the average longitudinal strain in

Mode	f_{sim}	f_{exp}	Q_{exp}
1st out	9.48	9.42	12000
2nd out	20.0	20.0	7750
1st in	20.7	20.8	3110
3rd out	32.3	32.3	5570
4th out	46.9	46.8	4410
2nd in	54.3	54.4	2630
5th out	64.1	63.9	3620
6th out	83.8	83.5	3220
3rd in	103	103	2210
7th out	106	107	2950
8th out	131	132	2700
9th out	158	160	2510
4th in	166	167	1740
10th out	187	190	2190
11th out	219	223	1970
5th in	244	243	1760
12th out	252	258	1660

Table 2.1: Predicted, f_{pred}, and experimental, f_{exp}, resonance frequencies, as well as quality factors in vacuum, Q_{exp}, for the lowest twelve out-of-plane (out) modes and lowest five in-plane (in) modes of a 16-μm-long beam E7A3. In simulations, we assume the following material properties for the SiC layer: Young's modulus 430 GPa, Poisson ratio 0.3, mass density 3.2 g/cm^3 [42], and intrinsic tensile strain 2.8×10^{-4}. The strain value was varied to obtain the best fit to the experimental frequencies.

the displacement transducer. If the temperature variations induced by the actuation voltage are sinusoidal and resonant with the vibrational mode n at frequency ω_n, the strain distribution in the piezoresistor is mostly determined by the corresponding mode shape, $\mathbf{u}^{(n)}(\mathbf{r})$, which specifies the vector displacement $\mathbf{u}$ of the infinitesimal volume element located at radius vector $\mathbf{r}$. The amplitude of motion in steady state can then be deduced from the condition of balance between the energy dissipated by the nanomechanical resonator due to its finite quality factor and the mechanical work done by the time-varying thermal stresses induced in the drive loop[4]:

$$\frac{c_n \omega_n^2}{Q_n} \int \rho(\mathbf{r}) \mathbf{u}^{(n)}(\mathbf{r})^2 d\mathbf{r} = \int \sum_{i,j} \sigma_{ji}^{th}(\mathbf{r}) \frac{\partial \mathbf{u}_i^{(n)}(\mathbf{r})}{\partial \mathbf{r}_j} d\mathbf{r}. \tag{2.1}$$

Here the summation is over all spatial coordinates and the integrals are over the volume of the bilayer resonator, c_n is the normalized mode amplitude, $\rho(\mathbf{r})$ the local mass density, and $\sigma_{ji}^{th}(\mathbf{r})$ the amplitude of the thermal stress tensor. If we assume, for simplicity, that gold and silicon carbide components are elastically isotropic, then $\sigma_{ii}^{th}(\mathbf{r}) \approx 3\alpha(\mathbf{r})\Delta T(\mathbf{r})B(\mathbf{r})$, where $\alpha(\mathbf{r})$ is the thermal coefficient of linear expansion, $\Delta T(\mathbf{r})$ is the amplitude of temperature change, and $B(\mathbf{r})$ is the bulk modulus. Solving Eqn. (2.1) for the mode amplitude c_n allows us to find the spatially averaged longitudinal strain in the piezoresistor $\langle \epsilon_{xx} \rangle = c_n \left\langle \frac{\partial \mathbf{u}_x^{(n)}(\mathbf{r})}{\partial x} \right\rangle$, and hence the corresponding downmixed voltage signal.

For the higher flexural out-of-plane modes, the strain may change sign within the length of the actuation or detection loop (Figure 2.8, inset), resulting in partial cancellation of the r.h.s. integral in Eqn. (2.1) and the detected strain average. To study these cancellation effects, we can introduce an empirical efficiency of the combined electrothermal drive and piezoresistive detection. Since the resonance amplitude a is normally proportional to the bias voltage V_b, drive voltage squared V_d^2, and the quality factor Q, we will define the efficiency as $\eta = a/(QV_d^2 V_b)$ to cancel out these trivial dependencies. Defined in this way, the efficiency η depends only on the strain and temperature distributions in the resonator. Figure 2.8 shows that this efficiency η generally decreases with the mode number and, in this device, dips sharply for the 11th out-of-plane mode due to almost complete

[4] See Appendix C for more detail.

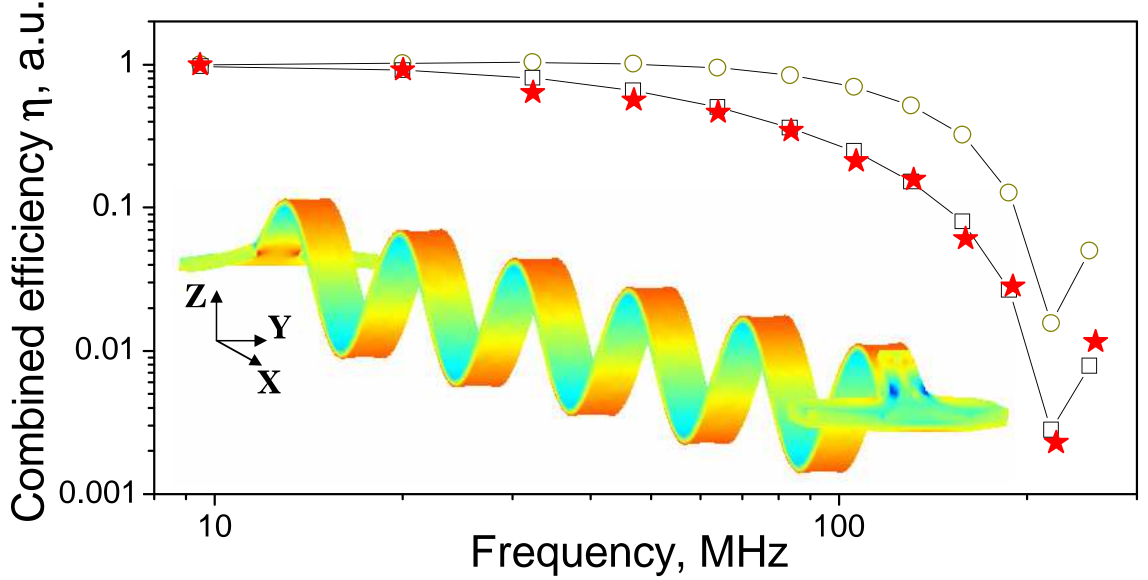

Figure 2.8: Efficiency of electrothermal drive and piezoresistive detection, normalized to that of the fundamental mode, for the first 12 out-of-plane modes of the 16-μm-long beam. The stars show experimental data, while the connected symbols show the results of finite element simulations excluding (circles) and including (squares) the effect of 40 MHz thermal rolloff. Inset shows the predicted shape of the 11th out-of-plane mode.

cancellation of drive integral in Eqn. (2.1). Note that for in-plane modes, the drive integral should cancel completely due to symmetry, and the efficiency η should, in principle, be zero. In practice, real devices are never perfectly symmetric, and we find that the in-plane modes are easily detectable with increased drive voltages. However, the measured efficiencies for in-plane modes are typically 1–2 orders of magnitude smaller than the efficiencies of out-of-plane modes of similar frequencies.

The efficiency η additionally decreases with frequency because of the delayed response of the temperature to Joule heating. In order to be most effective, the temperature must follow the drive voltage (squared) instantaneously, but in reality it takes a thermal time constant, τ_{th}, for the temperature to equilibrate. Therefore, above a certain drive frequency, the induced temperature variations will roll off since the device acts as a thermal low-pass filter, and the efficiency of thermal drive will decrease accordingly. The thermal time constant estimated from fitting finite-element simulations for efficiency to the experimental data is $\tau_{th} = (2\pi \cdot 40\text{MHz})^{-1} \approx 4$ ns (Figure 2.8). This number agrees with the theoretical estimate for τ_{th} we derive by directly considering the heat conduction dynamics in the bilayer actuator.

Electrothermal actuation and piezoresistive detection with large voltages can excessively heat the device. This becomes especially important for electrothermal drive above the thermal cutoff frequency, since only a fraction of the applied time-varying Joule heating power then results in useful periodic temperatures changes; the remainder simply raises the average temperature of the beam. While it is difficult to measure the temperature distribution of the beam directly, we can estimate the average temperature increase of the beam from the observed changes in resonance shapes at high applied voltages using separately determined temperature dependencies of resonance frequencies and Q factors. These measurements indicate that the devices are approximately one tenth of a degree Kelvin hotter than the environment for every microwatt of dissipated Joule power. The majority of data collected in this experiment was thus taken with the beams only a few degrees Kelvin hotter than the environment.

The combination of electrothermal actuation and piezoresistive detection thus provides a convenient and efficient all-electronic measurement technique for NEMS devices and will be beneficial in applications such as mass sensing, where obtaining data from multiple modes can improve the accuracy and speed of measurements. Both thermal actuation and piezoresistive detection scale more favorably with the device dimensions than many alternative techniques, allowing future experiments with even smaller nanomechanical devices.

Chapter 3

Frequency tuning techniques for nanomechanical resonators

In many experiments, we need to tune the frequency of the nanomechanical resonator. The necessary tuning may be small, as when we try to compensate for the variation in resonance frequencies due to fabrication imperfection, contamination, or aging. The needed tuning may also be large, as when we need to observe the changes in resonance parameters over a wide range of frequencies. Since the resonance frequency of a nanomechanical resonator is determined by its effective mass and the effective spring constant, there are two basic methods of tuning the frequency: changing the effective mass and changing the effective spring constant of the resonator.

Both of these approaches have been explored in microelectromechanical resonators. One popular way to reversibly tune the restoring force is to add electrostatic terms to the equations of motion of the resonator, usually done by applying a DC voltage to a nearby gate. The electrostatic tuning mechanism (also known as capacitive tuning) has been demonstrated for many different types of MEMS resonators (see, for, example Refs. [49, 50, 51, 52]). The restoring force of MEMS resonators has also been reversibly tuned using thermally induced stresses [53]. The mass of MEMS resonators has been tuned by focused-ion-beam deposition [54] and laser ablation [55]. These methods of mass tuning produce permanent frequency changes and cannot be easily reversed.

Many of these techniques have been demonstrated for nanomechanical resonators as well. Electrostatic tuning has been demonstrated for carbon nanotube resonators [56]. Electrothermal tuning has been demonstrated for nanoscale doubly clamped beams [38]. The mass of nanomechanical

resonators has been irreversibly tuned in situ by metal deposition [57]. Nanomechanical resonators have also been reversibly tuned by bending the substrate [58] and changing the clamping conditions with a scanning tunneling microscope [59].

In our experiments, we have used two frequency tuning techniques: electrostatic tuning using a side gate; and reversible gas-adsorption tuning at low temperatures. They are described in more detail in the following sections.

3.1 Electrostatic tuning[1]

In microscale devices, capacitive tuning can be realized with electrodes of many different geometries. However, in nanoscale devices, the possible geometries are limited by the available nanofabrication techniques. One way to realize electrostatic tuning is to use the chip substrate itself as a tuning electrode. This approach has been taken in the nanotube resonator experiments [56]. In this section, we describe an alternative approach, in which the tuning electrode is lithographically defined using the same fabrication techniques as for the resonator itself. In our experiments, we were able to study the effect of in-plane gate voltage on the properties of both out-of-plane and in-plane fundamental modes of a doubly clamped beam.

Figures 3.1(a) and 3.2(a) show two scanning electron micrographs of the resonator used in these experiments. The beam is made out of 100-nm-thick silicon carbide with a 40-nm-thick gold-palladium metal film on top. The beam was 150 nm wide, 15 μm long, and positioned 300 nm away from the in-plane gate electrode. The beam resonances were measured using magnetomotive actuation and detection in a 7 Tesla magnetic field created by a superconducting solenoid. The fundamental in-plane and out-of-plane modes have resonance frequencies of 7.60 MHz and 8.78 MHz, respectively.

There are two basic mechanisms by which the electrostatic forces between the beam and the tuning gate can alter the resonance frequency the of beam. First, the attraction between the beam and the nearby gate can stretch the beam and create additional tension that will increase the

[1] Measurements described in this section were performed in collaboration with I. Kozinsky.

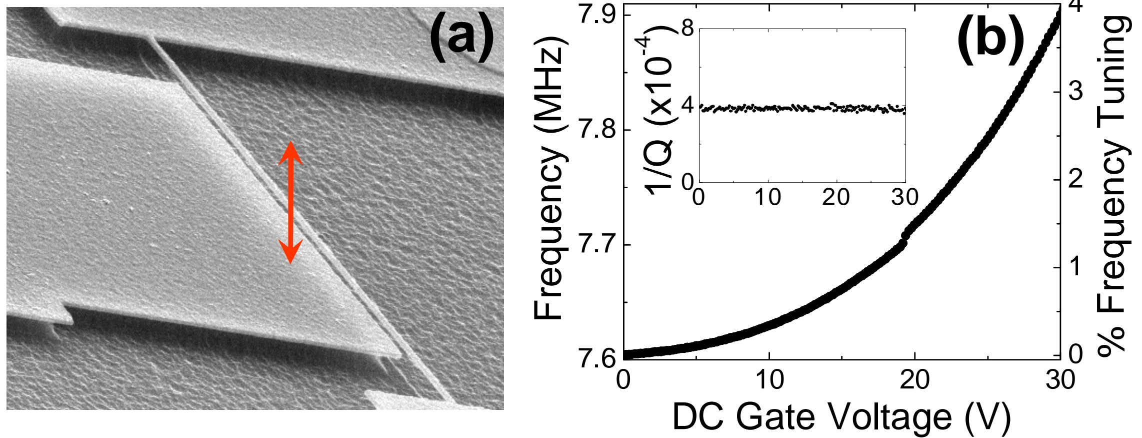

Figure 3.1: (a) Scanning electron micrograph of the SiC doubly clamped beam used in the tuning experiments. The red arrow indicates the direction of motion for the out-of-plane resonance. (b) Frequency of the fundamental out-of-plane mode versus applied gate voltage. The inset shows the mechanical losses versus the tuning voltage.

resonance frequency. Second, the dependence of the electrostatic attraction on the distance between the beam and the gate can change the effective restoring force for the beam, which can tune the frequency down. The detailed theory of the capacitive tuning in this system was developed by Inna Kozinsky [46, 60], and here I will only discuss qualitative aspects of the theory.

These two mechanisms affect the out-of-plane and in-plane modes differently. The out-of-plane mode is primarily affected by the stretching of the beam. The spatial dependence of the attractive force does not affect its frequency because the distance between the beam and the gate is nearly unchanged during out-of-plane oscillation. As a result, the frequency of the out-of-plane mode increases with increasing tuning gate voltage. Figure 3.1(b) shows that the frequency of the out-of-plane mode depends on the voltage applied to the tuning gate. The inset shows that the tuning does not noticeably affect the mechanical quality factor.

For the in-plane mode, the spatial dependence of the attractive force between the beam and the gate is the dominant effect. As a result, the frequency of the beam decreases with increasing gate voltage. At high applied voltages, the gate voltage also significantly reduces the quality factor of the resonance. This is because the changing distance between the beam and the gate modulates the capacitance between them and therefore the charge accumulated on the beam. The modulation of charge induces additional currents in the beam that produce a Lorentz force that provides additional

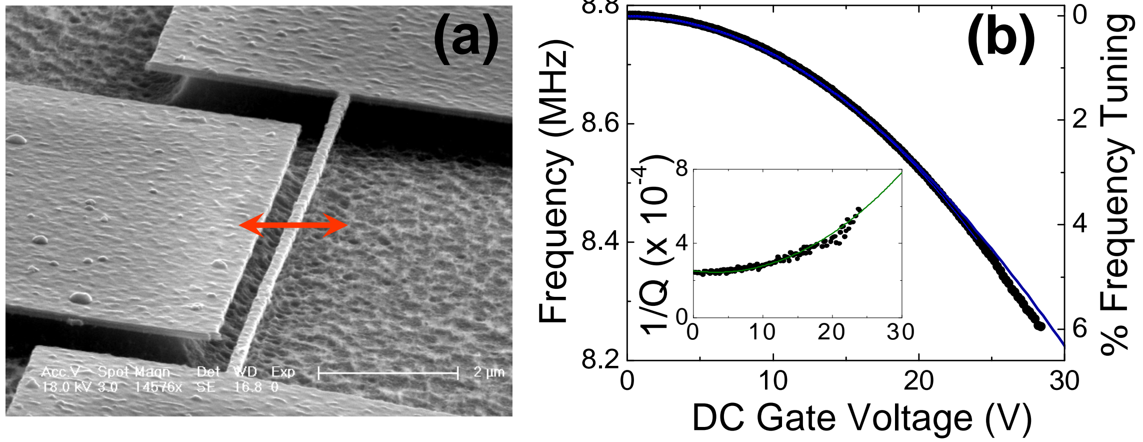

Figure 3.2: Same as Figure 3.1 for the fundamental in-plane mode. The blue curve in (b) is the prediction of the theoretical model for the capacitive frequency tuning.

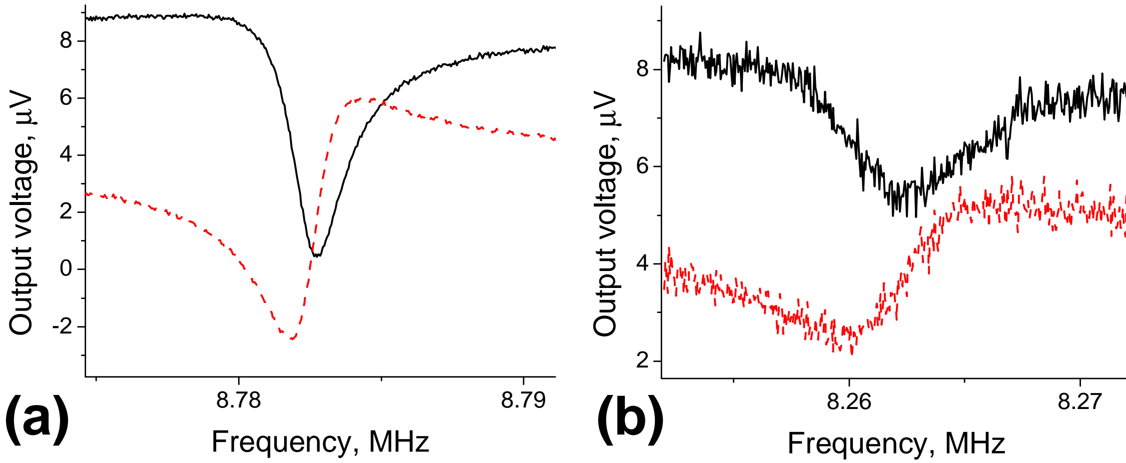

Figure 3.3: Resonance curves of the in-plane mechanical mode for a tuning voltage of zero (a) and 28 V (b). Both quadratures of the signal are shown. The amplitude of the resonance peak is smaller in (b) because of the reduced quality factor.

damping. At the highest applied tuning voltages, the quality factor was less than half the quality factor without any tuning voltage. The broadband electrical noise also depended on the applied voltage, increasing by approximately a factor of five as the tuning voltage increased from 0 V to 28 V (Figure 3.3). Although the reasons for the increase in the broadband noise are not entirely clear at this point, they are most likely related to the parasitic leakage currents between the the gate and the beam at high tuning voltages.

The maximum change in frequency we have observed with capacitive tuning is approximately $+4\%$ for the out-of-plane mode and -6% for the in-plane mode. These changes in frequency occurred

when DC voltage of approximately 28 V was applied to the tuning gate. Gate voltages higher than 35 V typically destroyed similar devices either because of snap-in of the beam into the tuning electrode or because of dielectric breakdown. Thus, electrostatic tuning can produce significant changes in resonance frequencies of a doubly clamped beam but has some important limitations. In particular, the in-plane mode suffers from a decrease in the quality factor, and both modes suffer from an increase in broadband electrical noise at high tuning voltages.

The capacitive tuning also becomes less effective for resonators of higher frequencies, as these resonators are stiffer and need larger forces to change the spring constant by the same percentage. To illustrate this, we have theoretically modeled the response of a beam that is three times shorter than the one described above, i. e., 5 μm long, and has all other dimensions the same. According to these calculations, the resonance frequency of the in-plane mode would change from 47.12 MHz at zero tuning voltage to 47.02 MHz at 30 V tuning voltage—a tuning range of only 0.2%. This tuning range can be increased by proportionally reducing the gap between the beam and the electrode. For example, if we reduce the gap from 300 nm to 100 nm, the same 5-μm long device will tune from 47.12 MHz to 45.18 MHz—a tuning range of 4%, which is comparable to the tuning range demonstrated above. Scaling capacitive tuning to even shorter beams and higher frequencies is problematic, however, as it would require electrode gaps of less than 100 nm, which would be difficult to fabricate using the present e-beam lithography techniques.

3.2 Adsorption tuning

As discussed in previous section, capacitive frequency tuning becomes less effective at higher frequencies. It is also difficult to engineer appropriate electrodes for tuning of higher flexural modes since the electrode geometry most effective for one flexural mode may be completely ineffective for another. For these applications, it is easier to perform frequency tuning by changing the effective mass of the resonator.

In this section, I describe a mass tuning mechanism based on adsorption of inert gas molecules at low temperatures. If a resonator is kept at typical liquid helium temperatures ($T < 30$ K),

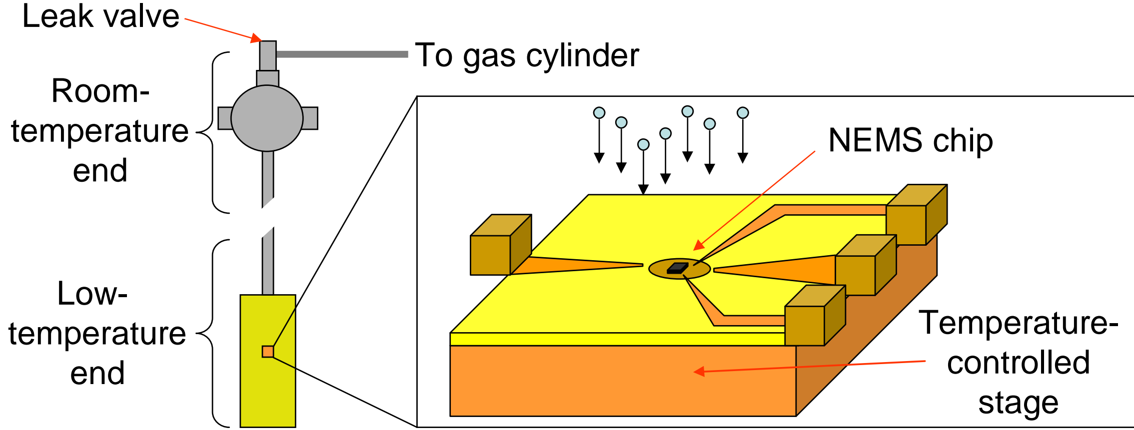

Figure 3.4: Schematic of the adsorptive tuning setup

a large variety of nonreactive gases will readily physisorb, i. e., freeze onto its surface, thereby increasing its mass. In my experiments, I have used nitrogen, argon, carbon dioxide, and xenon gases. These gases were chosen because their melting temperatures were significantly higher than the estimated temperature of the resonator, but lower than room temperature. Under such conditions, the spontaneous evaporation of adsorbent gas from the resonator was negligible at low temperatures, but the adsorbed molecules could be easily removed by a quick local heating of the resonators.

Figure 3.4 shows a schematic of the relevant part of the experimental setup. The cryogenic dipper consists of a low-temperature end, a room-temperature end, and a 6-foot stainless steel tube that connects the two. The nanomechanical resonator is mounted on a temperature-controlled sample stage inside the low-temperature end. The low-temperature part of the dipper can be lowered into a dewar with liquid helium, bringing the temperature of the sample stage to less than 10 K.

The room-temperature end houses the feedthroughs necessary for resonance measurements and temperature control, a pressure gauge, and a variable leak valve (MDC Vacuum Products Corp., Hayward, CA), which can deliver steady flows from 7.5×10^{-3} to 7.5×10^{-8} Torr·l/s. The tube connecting the two ends of the dipper is straight and provides a clear line of sight between the mounted resonator and the room-temperature end of the dipper. The cables used for measurements and temperature control were positioned to prevent them from blocking this line of sight.

Figure 3.5 shows the resonance curves of the seventh out-of-plane mode of a doubly clamped

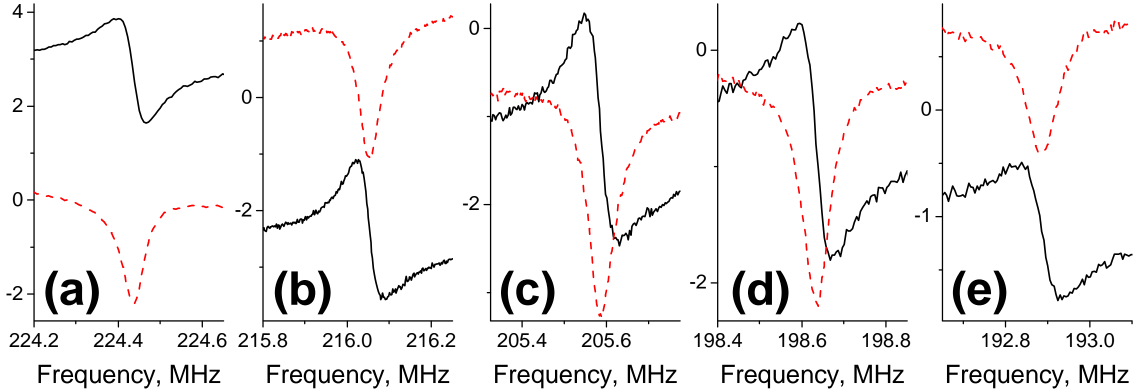

Figure 3.5: Results of adsorption tuning for the seventh out-of-plane mode of a SiC doubly clamped beam (device no. E7D1) using argon gas. Panels (a)–(e) show both quadratures of the resonance response at various stages of the tuning process.

beam obtained by continuously leaking argon gas into the dipper. In these experiments, I used a 10-μm-long silicon-carbide beam similar to the devices described in Section (2.3). The typical rate of frequency tuning I used was a few hundred Hertz per second, corresponding to a tuning by 1 percent in 3 hours. Due to time constraints, I stopped taking data when the frequency was tuned down by approximately 14%, although the tuning process could be continued further.

As can be seen from Figure 3.5, there are significant changes in the background in both quadratures during the tuning, but the resonance curves themselves do not change much. The broadband electrical noise increased from approximately 3 nV/$\sqrt{\text{Hz}}$ at the beginning of the tuning process (Figure 3.5(a)) to approximately 6 nV/$\sqrt{\text{Hz}}$ at the end (Figure 3.5(b)). This twofold increase in noise is much smaller than the fivefold increase in the case of capacitive tuning, but the reasons for the increase in noise are not clear in this case either.

As the frequency of the resonance was tuned down, the quality factor of the resonance generally decreased, as shown in Figure 3.6. In the case of argon, the quality factor apparently increased slightly at the beginning of the tuning process, but then decreased as with other adsorbents. For xenon tuning, the quality factor changed from approximately 3600 to approximately 2500 as the frequency was tuned down by more than 16%, which compares favorably to the results of capacitive tuning of the in-plane mode. For large tunings, the decrease in the quality factor depended on the chosen adsorbate, with xenon producing the smallest relative decrease in quality factor and carbon

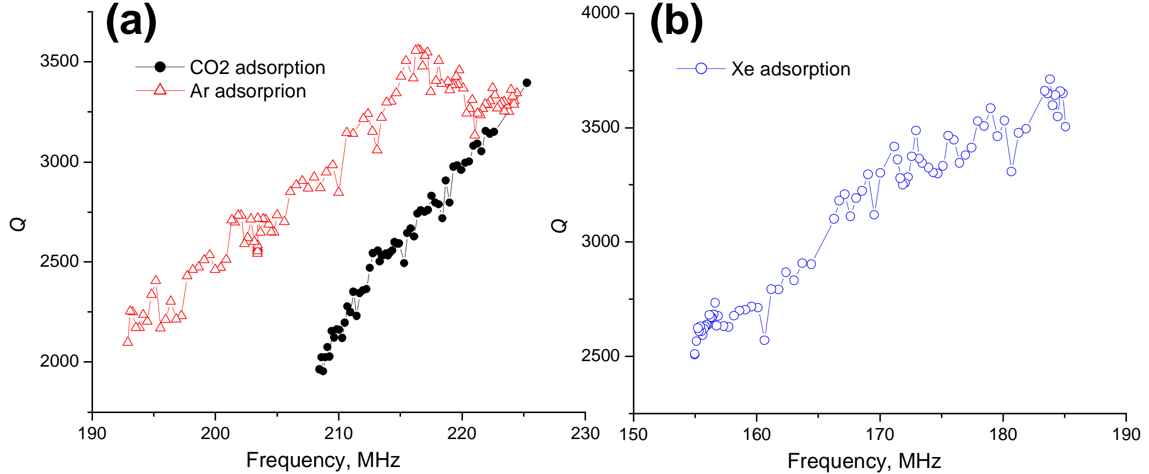

Figure 3.6: The quality factor of the tuned resonance as a function of resonance frequency for the experiments using carbon dioxide, argon, and xenon. Panel (a) shows results for the 7th out-of-plane mode of a 10-μm-long silicon-carbide beam (device no. E7D1). Panel (b) shows results for the 7th out-of-plane mode of a 10-μm-long silicon-nitride beam (device no. N3C1). The quality factor was obtained by fitting the resonance curves like those shown in Figure 3.5. The uncertainty in the fitted quality factor was approximately 3%.

dioxide, the largest.

As mentioned before, the results of adsorption tuning are easily reversible. All that is necessary to reset the experiment is to briefly heat the sample stage to a temperature above the boiling temperature of the particular gas used. This procedure results in quick desorption of all gas molecules, which restores the original frequency and quality factor of the resonator. This can be seen in Figure 3.6, where I first tuned the frequency down using carbon dioxide, then briefly heated the sample to 220 K, and then repeated the experiment using argon as the adsorbate. After heating, the frequency and the quality factor returned to the original values.

Because of time constraints, the maximum demonstrated range of frequency tuning in these experiments was approximately 15%.[2] However, the decrease in frequency can become saturated much earlier if the resonator is not sufficiently cold. Generally, the temperature of the resonator was determined by the temperature of the sample stage, typically kept at 8 K, and the temperature increase due to Joule heat dissipation inside the resonator itself. Some amount of Joule heat dissipation is necessary for the thermoelastic actuation and piezoresistive detection. In the majority of

[2] I chose this maximum value of 15% because it would be sufficient for the spin-sensing experiments described in Chapter 4.

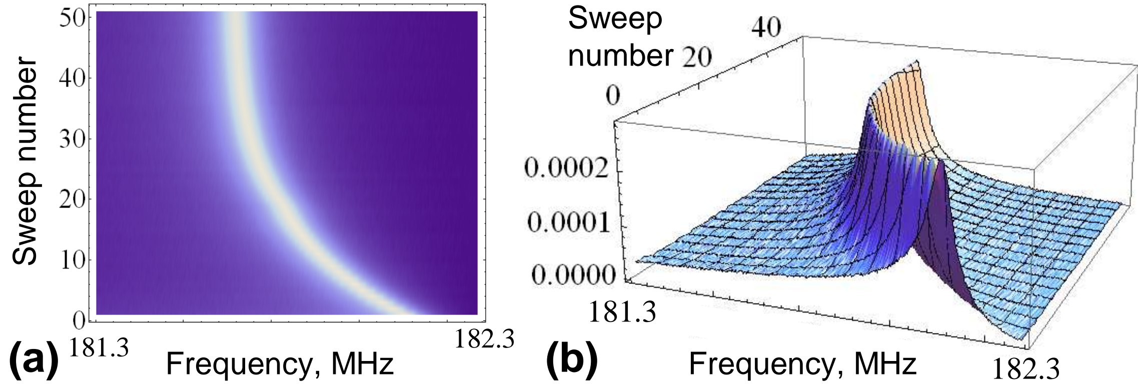

Figure 3.7: Saturation of xenon adsorption tuning for the 7th mode of a 10-μm-long doubly clamped beam (device no. N3C1). The panels show density (a) and 3D (b) plots of the amplitude of the resonance response. Brighter points in the density plot correspond to higher amplitudes. The resonance curves were measured repeatedly as the frequency of the resonance was slowly tuned down.

the experiments, I kept the estimated temperature increase due to Joule heating to less than 10 K, meaning that the temperature of the resonator was less than 20 K. However, in some experiments, I increased the bias and drive voltages to the point where the estimated temperature of the resonator reached approximately 50 K. At such high temperatures, the maximum amount of tuning I could obtain was typically limited to less than 1%.

Figure 3.7 shows the saturation of frequency tuning using xenon gas and a resonator at an estimated temperature of 50 K. The maximum tuning of frequency in this case is only about 0.3%. This amount of frequency tuning corresponds to mass loading by approximately one monolayer of xenon atoms. This data suggests that the first monolayer readily adsorbs to the resonator even at these high temperatures, but the subsequent monolayers do not.

It must be noted that, even at low temperatures, not all incident gas molecules stick to the surface of the resonator. According to our experimental estimates, only about 1% of the incident molecules do. The reason why the sticking coefficient was so low is not clear, but the fact that the incident molecules have an average thermal speed corresponding to room temperature (300 K) may play a role in the explanation. From the perspective of the low-temperature resonator, its surface is bombarded by molecules with a high kinetic energy, which may produce some sputtering of the already adsorbed gas molecules and a reduction of the overall sticking coefficient.

In summary, adsorption tuning of nanomechanical resonators works well at low temperatures, regardless of the resonance frequency and the mode used. The best results are obtained with noble gases like argon or xenon, although other gases with high melting points may be used also. During the tuning process, the temperature of the resonator must be kept low to avoid saturation of mass loading at approximately one monolayer coverage.

Chapter 4

Nanomechanical sensing of spin systems

Since its discovery in 1938 [61], magnetic resonance of spin systems has been one of the most important tools in studying properties of matter [62]. Nuclear magnetic resonance (NMR) has been used to elucidate the chemical structure of many molecules—most recently proteins and other complex biomolecules. NMR has also been used in manufacturing control, nondestructive testing and identification of samples, and gave rise to magnetic resonance imaging (MRI), with its own myriad of technical and medical applications. Electron spin resonance (ESR), although less famous than its nuclear cousin, is a powerful tool for studying free radicals and paramagnetic centers and has also found many applications in chemistry, physics, and biology. Finally, ferromagnetic resonance (FMR) has been used to study ferromagnetic materials and devices and thus has played a role in the development of magnetic storage media.

Despite the continuing progress in the sensitivity of magnetic resonance instruments, conventional magnetic resonance essentially remains a bulk technique, i. e., it is normally used to study a sample of macroscopic dimensions. Extending magnetic resonance techniques to the micro- or even nanoscale would open the possibility of studying the magnetic, chemical, and structural properties of individual nanoscale objects or even individual molecules. In 1991, John Sidles proposed to do exactly that by detecting magnetic resonance with microscale mechanical resonators rather than conventional RF coils [63]. The resulting system combined the essential features of MRI and atomic force microscopy (AFM) and therefore acquired the name magnetic resonance force microcopy (MRFM).

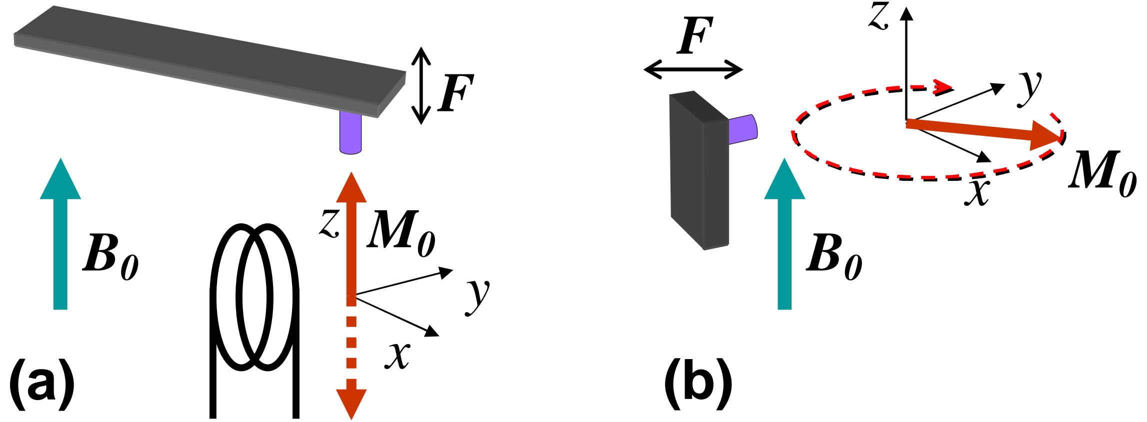

Figure 4.1: Schematics of the longitudinal (a) and transverse (b) MRFM configurations. Both schemes use the dynamics of magnetization M_0 in the external field B_0. The time-dependent magnetization creates a force F on the magnetic tip that affects the motion of the cantilever. In the longitudinal case, the magnetization is modulated with the help of the RF field created by an external coil.

Shortly after the proposal, the first MRFM experiments were performed, detecting magnetic resonance of electron [64] and nuclear [65] spins. The sensitivity of MRFM experiments has been steadily progressing since, improving by a factor of more than one million by now. Recently, Rugar and coworkers demonstrated detection of a single electron spin [8] and nuclear magnetic resonance imaging with 90 nm resolution [9]. Experimenters are now closer than ever to the single-nuclear-spin sensitivity and the holy grail of MRFM—three-dimensional imaging of individual biomolecules and other nanoscale objects with atomic resolution. The progress towards this goal over almost two decades has been reviewed early in Ref. [66] and more recently in Ref. [67].

Fundamentally, MRFM experiments can be done in two different ways [68]: the motion of the mechanical resonator can be coupled to either longitudinal or transverse part of the magnetization of spins (see Figure 4.1). The main difference between them stems from the fact that, for spins in a strong magnetic field B_0, the longitudinal component of the magnetization evolves slowly, whereas the transverse component performs fast precession at the Larmor frequency $\omega_L = \gamma_s B_0/\hbar$, where γ_s is the gyromagnetic ratio of the spin [62]. Correspondingly, longitudinal MRFM uses low-frequency resonators, typically in the kilohertz range. Transverse MRFM should use resonators that resonate at the Larmor frequency, which is typically in the megahertz range or higher.

In practice, all MRFM experiments published so far have used the longitudinal scheme. In these

experiments, the longitudinal magnetization is typically modulated at the resonance frequency of the cantilever with the help of an external source of electromagnetic field. The resulting time-dependent longitudinal magnetization exerts a periodic force on the magnetic tip of the cantilever, which measurably affects the motion of the resonator.

Experiments using transverse magnetization proved much more difficult. One reason is that transverse MRFM requires resonators that have high resonance frequencies and, at the same, are compliant enough to detect the tiny forces produced by spins. These two requirements conflict with each other because the frequency of a resonator is given by $\omega_R = \sqrt{k_{eff}/m_{eff}}$, where k_{eff} is the effective spring constant and m_{eff} is the effective mass of the resonator. For a resonator of a given mass, the resonance frequency can only be increased by making the resonator stiffer (less compliant). Looking at the same expression another way, we obtain $m_{eff} = k_{eff}/\omega_R^2$, which means that achieving a high resonance frequency and a small spring constant (high compliance) at the same time can only be done by minimizing the effective mass. Since nanomechanical resonators are currently the smallest and lightest mechanical resonators available, they are a natural choice in this situation, but even with nanoscale resonators transverse MRFM remains extremely challenging.

In this chapter I describe our work towards demonstrating a system in which the motion of a nanomechanical resonator is coupled to the transverse rather than longitudinal component of magnetization of nuclear spins.[1] In the following sections, I analyze in more detail the transverse MRFM system as well as other physical systems in which such coupling may be realized and describe our attempts to detect the signatures of such coupling in experiment. I conclude the chapter by exploring the theoretical analogy between the coupled spin-resonator system and the quantum optical model of a laser.

[1] I focused on nuclear spins because it is currently possible to fabricate devices that resonate at nuclear Larmor frequencies, which are typically in the range of 1–100 MHz for an external field of a few Tesla. For electron spin resonance, the Larmor frequencies would be 30 GHz or higher, which far exceeds the frequency range of the currently feasible nanomechanical resonators.

4.1 Mechanisms of coupling between spins and mechanical motion

One way to make a mechanical resonator interact with transverse magnetization of nuclear spins in a nearby sample is to attach a permanent magnet to a cantilever, as shown in Figure 4.2(a). This is basically the transverse MRFM (T-MRFM) system [68]. Note that in this case the ferromagnet on the cantilever tip creates a constant magnetic field of its own, which can be approximated as the field of a magnetic dipole. When superposed on the uniform external field B_0, this field modifies the total magnetic field seen by the spins and, therefore, their Larmor frequency. As a result, only a certain slice of the sample, known as the sensitive slice, will have the Larmor frequency equal to the resonance frequency of the cantilever. The position of this resonant slice will generally depend on the value of the external field B_0, and at some values of the field, the resonant slice may be outside the sample or not exist at all.

In this case of Larmor-frequency resonators, there are two aspects to the interaction between the spins and the resonator. First, the rotating transverse component of nuclear magnetization exerts a magnetostatic force on the ferromagnetic tip, which can drive or otherwise affect cantilever oscillations. Secondly, a moving ferromagnet creates an AC magnetic field, oscillating at the frequency of the cantilever motion, inside the nearby sample. At a point characterized by the radius vector $\vec{r}$, this RF field is given by $A\frac{\partial B_\perp(\vec{r})}{\partial x}$, where A is the amplitude of cantilever motion and $\frac{\partial B_\perp(\vec{r})}{\partial x}$ is the derivative of the transverse component of the ferromagnetic tip's magnetic field with respect to the direction of the cantilever motion x (see Figure 4.2(a)). We can therefore use the cantilever itself to create the RF field that will drive transitions between Zeeman levels of nuclear spins, obviating the need for an RF coil that is used in the longitudinal MRFM experiments.[2]

In principle, we could still use an external RF coil to control the magnetic spins, similar to the case of longitudinal MRFM, and use the cantilever only to detect the spin dynamics. However, because the RF field created by the coil would oscillate at the Larmor frequency, this field will

[2]This method of producing local RF was used in Ref. [69], where a cantilever with a magnetic tip was used to create an RF field inside a small volume of a cell containing cesium vapor. This RF field then affected the populations of Zeeman levels of cesium atoms, which was detected optically.

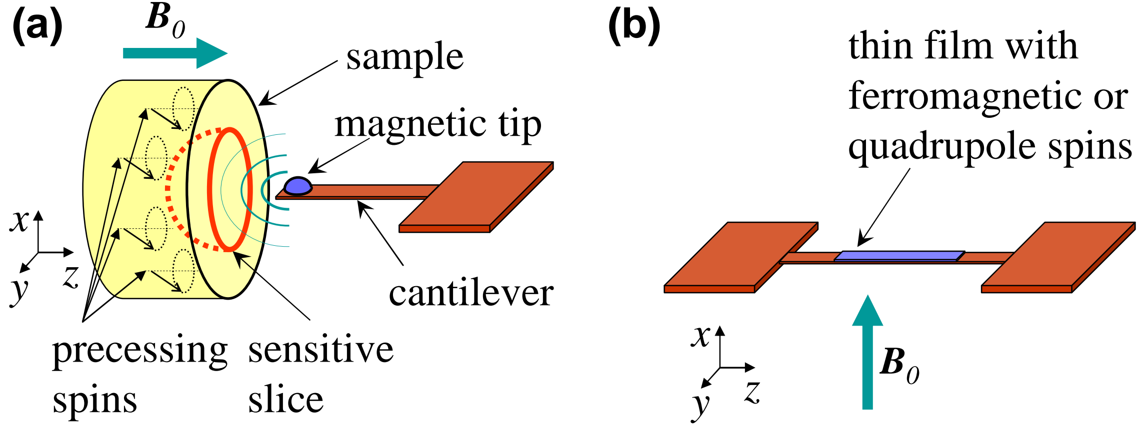

Figure 4.2: (a) Schematic of the transverse MRFM experiment. (b) Schematic of experiments with quadrupole-spin and ferromagnetic materials. A thin film of these materials can be deposited on the surface of the resonator during the fabrication process.

inevitably produce parasitic forces and moments acting on the magnetic tip of the cantilever. This will produce a large parasitic motion of the cantilever that has nothing to do with the spin dynamics.

In order to avoid this problem, we will instead consider the situation when both aspects of the interaction between the spins and the resonator are used: The cantilever is used to generate the local RF field that drives the cantilever dynamics, and the same cantilever is used to detect the dynamics of the spins. This situation is very similar to the standard NMR setup, with the RF cantilever playing the role of an RF coil. Because of this similarity, we can perform an analog of the early continuous-wave NMR experiments [62], in which the cantilever is always driven at resonance while the external magnetic field is swept through the value at which the Larmor frequency of the spins equals the resonance frequency of the cantilever. When the resonance condition is realized, the dynamics of the cantilever will be affected by the interaction with the spins. In particular, the amplitude of the cantilever motion will decrease because the excited magnetic spins will dissipate energy due to spin relaxation processes. This energy has to be replenished by the cantilever, which means that its effective quality factor and, correspondingly, its amplitude will decrease. The resonance frequency of the cantilever will also be changed slightly by the magnetostatic forces produced by the spins.

Similar to the case of continuous-wave NMR, we can write the modified complex amplitude of cantilever motion as

$$A = A_0/(1 + \chi),$$

where A_0 is the cantilever amplitude in the case when there are no spins and χ is the complex susceptibility of the spin system. The real part of the susceptibility describes the reduction in cantilever amplitude of motion due to the reduced quality factor and the imaginary part describes the the change in the phase of the cantilever response due to the modification of its resonance frequency.[3] Naturally, the susceptibility depends on the external magnetic field B_0 and the other parameters of the coupled cantilever–spin system.

Using the analogy to the coil-based NMR systems, we have derived the following formula for the susceptibility

$$\chi = \iiint \frac{Q_r \left(\frac{\partial B_\perp}{\partial x}\right)^2 \hbar^2 \gamma_n^3 B_s(\vec{r}) n(\vec{r})}{8 k_r k_B T \left[\Gamma_\perp + i(\gamma_n B_s(\vec{r}) - \omega_r) + \gamma_n^2 \left(\frac{\partial B_\perp}{\partial x}\right)^2 |A|^2/(4\Gamma_\parallel)\right]} \, d\vec{r}, \tag{4.1}$$

where the integration is over the volume of the spin sample. Here ω_r, k_r, and Q_r are the natural resonance frequency, spring constant, and quality factor of the cantilever; γ_n, $\Gamma_\perp = 1/T_2$, $\Gamma_\parallel = 1/T_1$, and $n(\vec{r})$ are the gyromagnetic ratio, transverse relaxation rate, longitudinal relaxation rate, and the local concentration of the nuclear spins; $B_s(\vec{r})$ is the static part of the magnetic field, which is the sum of the external field B_0 and the time-independent part of the field created by the ferromagnetic tip; k_B and T are the Boltzmann constant and the temperature of the nuclear spins. The temperature enters the expression because the equilibrium magnetization of nuclear spins decreases with increasing temperature according to the Curie law [62]. We have assumed spin-1/2 nuclei for simplicity, which means that $\frac{\gamma_n \hbar}{2}$ is the magnetic moment of one nuclear spin. The last term in the square brackets of the denominator in Eqn. (4.1) describes field saturation of the spin response.

In order to estimate whether we could actually detect the relative changes in the cantilever amplitude given by Eqn. (4.1), I have numerically calculated the susceptibility for the T-MRFM geometry shown in Figure 4.2(a) using the following realistic parameters: a cantilever with a resonance frequency $\omega_r = 2\pi \times 20$ MHz, a spring constant $k_r = 1$ N/m, and a quality factor $Q_r = 1000$; a cobalt ferromagnetic tip with saturation magnetization of 1.6 Tesla and a radius of 150 nm; and

[3] Note that this meaning of real and imaginary parts of χ is different from the case of electric and magnetic susceptibilities, where the imaginary part describes adsorption and the real part describes dispersion.

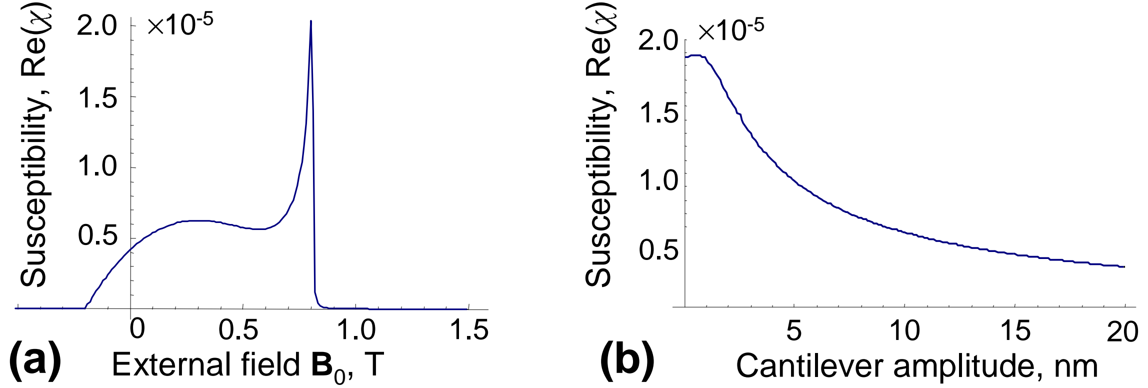

Figure 4.3: (a) Real part of the susceptibility versus external magnetic field. (b) Real part of susceptibility at resonance versus cantilever amplitude.

a temperature $T = 4.2$ K. For the spin sample, I modeled thallium metal, which has a large gyromagnetic ratio of $\gamma_n = 2\pi \times 25$ MHz/T, a transverse relaxation time $T_2 = 5\,\mu$s and a very short longitudinal relaxation time of $T_1 = 500\,\mu$s at 4.2 K. Fast longitudinal relaxation is important in this case because the faster the spins can dissipate energy to the lattice, the more energy they can suck out of the cantilever without getting saturated. As a result, thallium is expected to give the strongest signal for any elemental spin-1/2 system. Finally, I assumed a distance of 10 nm between the magnetic tip and the surface of the sample.

Substituting the parameters above, I have numerically integrated Eqn. 4.1 using the Mathematica software package. The results of the simulation are shown in Figure 4.3. The largest fractional change in the amplitude of the cantilever we can expect for these parameters is approximately 2×10^{-5}, which happens when the external field is given by $B_0 = \omega_r/\gamma_n = 0.8$ T.[4] The saturation of spin response starts at cantilever amplitudes of approximately $A_{sat} \approx 2$ nm. The maximum change in the cantilever amplitude is therefore approximately $A_{sat} \times \mathrm{Re}(\chi) \approx 4 \times 10^{-14}$ m. This expected signal should be compared to the amplitude of thermomechanical noise of $\sqrt{\frac{4k_BTQ}{k_r\omega_r}} \approx 4.5 \times 10^{-14}$ m$/\sqrt{\mathrm{Hz}}$, which means that the simulated change in the amplitude is just barely detectable.

In practice, the signal-to-noise ratio would be affected by many other sources of noise. In our measurements of silicon cantilever resonances, Johnson noise and other types of broadband excess noise were often significantly larger than the thermomechanical noise. Also, the stability of the

[4]Figure 4.3(a) shows only the real part of the susceptibility, but the maximum value of the imaginary part of the susceptibility is approximately the same.

cantilever amplitude, measured piezoresistively, was usually on the order of 10^{-4}, effectively preventing us from measuring relative changes in the amplitude on the order of 10^{-5}. Finally, thallium is an extremely toxic metal and would require extensive safety precautions. Other, safer materials generally resulted in an expected signal significantly smaller than that calculated above.

Thus, the prospects of detecting a transverse MRFM signal using the setup shown in Figure 4.2(a) looked grim and did not merit the required experimental effort. The main culprit was the relatively weak coupling between the spins and the cantilever that is provided by the ferromagnetic tip. We therefore turned our attention to alternative ways of coupling the mechanical motion and spin dynamics.

The first possibility we considered was to use the coupling between the spins and strains. Such coupling is not present in all materials, but some nuclei with a total spin of more than one half possess a significant quadrupole electric moment which couples the spin to the local gradient of the electric field [70]. The Hamiltonian of this interaction is given by

$$\hat{H} = \sum_{i,j} \frac{\partial E_i}{\partial x_j} \frac{eq}{6I(2I-1)} \left[\frac{3}{2} \left(\hat{I}_j \hat{I}_i + \hat{I}_i \hat{I}_j \right) - I(I+1)\delta_{ij} \right], \tag{4.2}$$

where $\frac{\partial E_i}{\partial x_j}$ is the electric field gradient tensor, $\hat{I}_i$ are the components of the spin operators for the nucleus, e is elementary charge, q is the quadruple moment of the spin, and δ_{ij} equals 1 if $i = j$ and 0 otherwise. Because the electric field at the site of a given nucleus is created by nearby electrons and other nuclei, the gradients of electric field change when the material is deformed:

$$\frac{\partial E_i}{\partial x_j} = \sum_{kl} \epsilon_{kl}\, S_{ijkl}, \tag{4.3}$$

where ϵ_{kl} are the components of the local strain tensor and the tensor S_{ijkl} depends on the crystalline structure and other properties of the chosen material. The magnitudes of the tensor components S_{ijkl} vary widely in different materials, and reach some of the largest values in tantalum and niobium (on the order of 5×10^{22} V/m^2) [70].

Because the spin dynamics couples directly to strain, nuclear magnetic resonance can be detected using acoustic waves in these materials. This technique is called nuclear acoustic resonance (NAR) and has been demonstrated for a large number of materials [70]. The experiments typically measured the response of an ultrasound acoustic resonator that incorporated a centimeter-sized single crystal of tantalum, niobium, or other quadrupole-active material. It is easy to imagine generalizing this scheme to nanomechanical instead of acoustic resonators, since nanomechanical resonators can easily produce large strains at RF frequencies as well.

Figure 4.2(b) shows a setup that could be used for such an experiment. A thin film of a quadrupole-active material is deposited on the nanomechanical resonator (cantilever or doubly clamped beam) during the fabrication process. The motion of such a cantilever then produces stresses and strains in the thin film of the quadrupole-active material, which drives the dynamics of the nuclear spins. Similar to the case of transverse MRFM, we can describe the effect of the nuclear acoustic resonance on the cantilever motion with the susceptibility χ. At resonance, all spins inside the thin film will participate in the resonance, producing a total fractional change in the resonator amplitude on the order of

$$\chi \sim \frac{NQ_r I(I+1)(S_{ch}qe)^2\omega_c}{8k_B T Y_r V_r \Gamma_\perp}, \tag{4.4}$$

where N is the total number of active quadrupole spins, S_{ch} is the characteristic value of the coupling tensor in the used quadrupole-active material, Y_r is the Young's modulus of the resonator material, and V_r is the volume of the resonator.

For a 50-nm-thick film of tantalum on 100-nm-thick silicon resonator, I estimated the maximum fractional change of the resonator amplitude to be $\chi \approx 1/\Delta B[\text{Gauss}]$, where $\Delta B[\text{Gauss}]$ is the expected width of the resonance, expressed in units of magnetic field. In many nuclear acoustic resonance experiments, the width of resonance was on the order of 100 Gauss [70], which would produce an easily measurable 1% change in the amplitude of the resonator response.

In practice, the width of the resonance is likely to be much larger in our experiments because of inhomogeneous broadening. Nuclear acoustic resonance experiments typically used carefully grown single crystals of pure tantalum, whereas in our case, the deposited thin film would be polycrystalline

and full of impurities. Compared to a single crystal of tantalum, this will create large and spatially variable static electric field gradients that will modify the local nuclear resonance frequencies. Based on the measured magnitude of the S tensor, the width of the magnetic resonance of a thin film of tantalum could be broadened to 1000 Gauss or more with nonuniform static strains on the order of 10^{-3}.

Our efforts to pursue this experiment soon faced a serious practical problem: we were not able to fabricate a resonator with a high-quality thin film of tantalum on it. Tantalum films sputtered on silicon and silicon nitride substrates turned out to be under a large compressive stress. As a result, when we deposited tantalum on fully fabricated cantilevers, the cantilevers curled up. When we sputtered tantalum on a flat piece of a wafer, the film delaminated and buckled up in some places. Our efforts to perform lift-off patterning of such films were also unsuccessful. We decided not to pursue niobium films because the expected signal from them is approximately 30 times smaller than for tantalum.

The final coupling mechanism we studied involved thin ferromagnetic films and was more successful from a fabrication point of view. This experiment used the same geometry as for quadrupole coupling (Figure 4.2(b)), but the nature of the expected coupling between the motion of the cantilever and the spins inside the ferromagnetic film is completely different, due to the unique properties of ferromagnetic materials.

One distinctive feature of ferromagnetic materials is that the frequency of nuclear magnetic resonance in such materials is almost independent of the external magnetic field. Instead, the NMR frequency is primarily determined by the effective internal magnetic field, which is determined by the hyperfine interaction in ferromagnets and is usually on the order of 10 Tesla. Another distinctive feature of ferromagnetic materials is the formation of domains of uniform magnetization. The domain size is usually on the order of 1 micron, but depends strongly on the material and the geometry of the magnetic film.

The first NMR measurements of ferromagnetic samples were done in late 1950s using cobalt

powder samples [71]. The surprising result of these measurements was that the cobalt sample absorbed far more power from the coil than expected. The magnetic resonance occurred at frequencies between 212 MHz and 227 MHz depending on the temperature, and the signal was 5×10^5 larger than expected. Subsequent studies attributed this signal enhancement to the motion of magnetic domain walls in the ferromagnetic sample.

When an external RF field H_{RF} is applied to a ferromagnetic sample, it creates forces on domain walls and drives their motion. The motion of the domain walls due to the external field is very small, on the order of $x_d = D \times H_{RF}/H_a$, where D is the domain size and H_a is the anisotropy field. However, a nucleus in the vicinity of a domain wall will see a change in the magnetic field on the order of $x_d \times H_{hf}/d$, where d is the width of the domain wall and H_{hf} is the effective hyperfine field. The nucleus will therefore see an oscillating field that is larger than the external RF field by a factor of $(H_{hf}D)/(H_a d)$. For cobalt, this field enhancement factor works out be on the order of 1000. Since energy absorption scales as applied field squared, it is not surprising that the energy absorption was almost six orders of magnitude larger than expected.

If a static external field B_0 is applied during NMR experiments with ferromagnetic samples, it has only a very small effect on the frequency of the resonance because the frequency is determined by the much larger hyperfine field. However, a strong external field can affect the magnitude of the of the NMR signal. In particular, as the external field approaches the saturation magnetization, all domains will align parallel to the external field B_0 and the domain walls will disappear. The field enhancement mechanism described above will then disappear also, decreasing the NMR signal dramatically. Early NMR experiments have shown that the maximum field that can be applied to a ferromagnetic sample without significantly reducing the signal is approximately 0.1 Tesla [71], which is significantly smaller than the cobalt saturation magnetization of 1.6 Tesla.

The large enhancement of the NMR signal in ferromagnets seemed really promising for our Larmor-frequency experiments. The necessary setup can be similar to the one considered for the quadrupole case: a thin film of ferromagnetic material on top of a nanomechanical oscillator (Figure 4.2(a)). The coupling between the mechanical motion and the nuclear spins can be mediated by

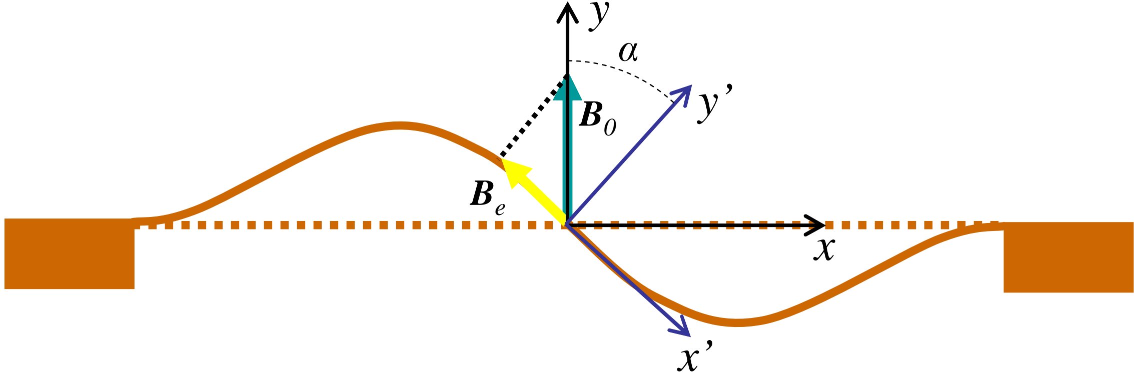

Figure 4.4: Effective in-plane magnetic field appearing during oscillations for the second out-of-plane mode of a nanomechanical oscillator.

two mechanisms. First, since the ferromagnetic film will be stressed during oscillation, the magnetostrictive effect will cause rotation of magnetization inside domains and domain wall motion. This changing magnetization can then drive the nuclear spins directly or through domain wall motion, similar to the case of external RF excitation described above.

Second, if we apply a moderate magnetic field (≤ 0.1 Tesla) perpendicular to the beam shown in Figure 4.2(a), the motion of the cantilever will create an effective RF field acting on the domain walls. During oscillations, different parts of the beam change their angle α with respect to the external field B_0 (see Figure 4.4). As a result, in the rotated frame of the ferromagnetic film (x', y'), the external magnetic field will appear to tilt periodically by the same angle α. For small angles, the in-plane projection of this external field is given by $B_e = \alpha B_0$, and the situation is equivalent to having a local RF magnetic field of the same amplitude. The effective field B_e will oscillate at the same frequency as the resonator and drive the magnetic domain walls in the ferromagnetic film, thereby coupling the mechanical motion to the spin dynamics.

Like in the case of transverse MRFM of quadrupole coupling mechanisms, we can detect the nuclear magnetic resonance in the ferromagnetic film by the effect this resonance would have on the motion of the resonator. The changes in the resonator's motion can again be described by the complex susceptibility χ. It is difficult to estimate χ for the case of the magnetostrictive coupling mechanism because we do not know enough about the magnetostrictive properties of thin cobalt films. For the second mechanism described above, which relies on the tilting of the resonator during

oscillation, we derived

$$\chi \sim \frac{N\hbar^2\omega_r Q_r}{4k_B T Y_r V_r \Gamma_\perp}\left(\frac{\gamma_n l_r B_0 C_{enh}}{Y_r V_r n_m t_r}\right)^2, \tag{4.5}$$

where N is the total number of active nuclear spins, l_r and t_r are the length and thickness of the resonator, n_m is the number of the used out-of-plane mode, and C_{enh} is the enhancement factor due to the domain wall motion.

Consider a 50-nm-thick cobalt film on top of 100-nm-thick, 10-μm-long SiC or SiN resonator, and assume that we will use the eighth out-of-plane mode with a resonance frequency of 230 MHz at a temperature of 4.2 K (these parameters correspond to actual devices we fabricated). If we also assume an NMR resonance width of 5 MHz and enhancement factor of 1000 [72, 73, 74], the susceptibility works out to be on the order of 10^{-2}, which should be detectable. Note that this estimate is very uncertain as there is only limited data on the resonance width or enhancement factor in thin cobalt films at low temperatures [72, 73, 74]. Nevertheless, we decided to go ahead and try to detect this signal.

4.2 Experimental results[5]

In this section, I describe our experiments using doubly clamped beams with deposited cobalt films. We chose to use cobalt because, of all ferromagnetic elements, cobalt gives the largest estimated susceptibility χ. However, cobalt was not easy to work with from a fabrication point of view. Evaporated cobalt films did not adhere well to silicon carbide substrates, so we switched to silicon nitride substrates instead. In addition, some of the patterned cobalt films slowly oxidized in air, changing shape and appearance under a microscope. We found that oxidation can be prevented by capping the cobalt layer with a thin layer of copper. We made the devices by first patterning the cobalt film and then fabricating the rest of the resonator using the methods described in Section 2.3. Figure 4.5 shows two representative resonators with ferromagnetic films.

Because the frequency of nuclear magnetic resonance in cobalt cannot be tuned by changing the

[5]Measurements described in this section were performed in collaboration with E.B. Myers and I. Kozinsky.

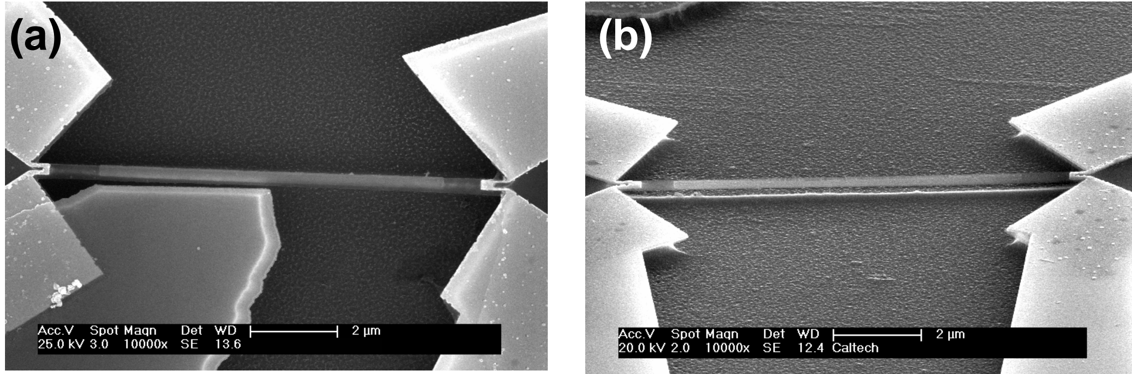

Figure 4.5: Scanning electron micrographs of doubly clamped beams with integrated ferromagnetic films, devices no. N1A3 (a) and N1B3 (b). The beams were nominally 10 μm long, 400 nm wide, and 100 nm thick. The metal loops at the two ends of the devices were used for thermoelastic actuation and piezoresistive detection. The brighter rectangles in the middles of the beams are the patterned ferromagnetic films, consisting of a 40-nm-thick cobalt layer and 20-nm-thick capping copper layer. The large irregular feature in the bottom left of panel (a) resulted from poor liftoff, but did not interfere with the operation of the device.

external magnetic field, we needed to fabricate devices with a mechanical resonance matching the cobalt NMR frequency, which is about between 215 and 225 MHz at low temperatures, depending on the crystalline phase. Basically, there were two ways to accomplish this goal: use a short beam with the fundamental resonance near 220 MHz or a longer beam with some higher out-of-plane mode near 220 MHz. The latter option was more attractive for two reasons. First, our experience with beams of varying lengths has shown that, for a given resonance frequency, higher modes of longer beams generally have higher quality factors than lower modes of shorter beams. Second, having multiple modes available for measurement allowed us to compare the properties of the mode that was resonant with the spins to the properties of other modes.

In these experiments, we used silicon-nitride beams that were nominally 400 nm wide and 10 μm long (Figure 4.5). The fundamental out-of-plane modes of these beams had resonance frequencies around 15 MHz and their eighth out-of-plane modes, around 225 MHz, close to the expected NMR frequency. The length of 10 μm was a reasonable choice, as significantly shorter beams had lower quality factors (see Section 5.1) and significantly longer beams had much smaller frequency spacing between different modes near 225 MHz, making the mode spectrum too complicated.

Even though the eighth out-of-plane modes of these devices were close to the expected NMR

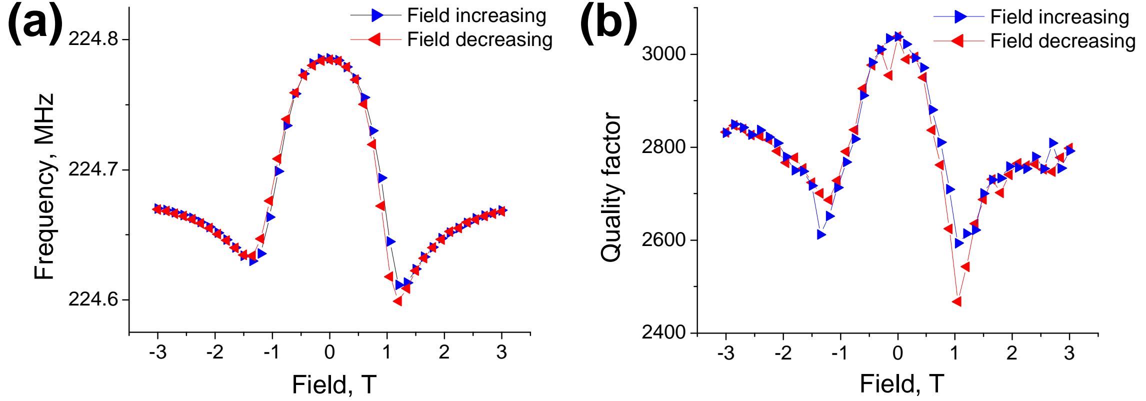

Figure 4.6: The frequency (a) and quality factor (b) of the eighth mode of the N1B3 beam versus the perpendicular magnetic field.

frequencies, we still needed a way to tune the mechanical resonance frequencies through the expected NMR frequency. The absorptive tuning technique was a convenient way to do that. Typically, we used argon gas as the adsorbate because it is much cheaper than xenon. The tuning range of 15% demonstrated in Section 3.2 was sufficient to change the resonance frequency of the eighth mode from 225 MHz to less than 200 MHz, thereby tuning this mode out of resonance with the nuclear spins.

Before trying NMR measurements, we first needed to verify that the deposited cobalt film was actually ferromagnetic. We did this by measuring the frequencies and quality factors of the mechanical modes as a function of the uniform perpendicular magnetic field B_0 (see Figure 4.2(b) for the geometry). Figures 4.6 show the results of these measurements for the eighth mode of the beam N1B3. The response of the resonance frequency and quality factor is rather complicated: as the field increased from zero to 3 Tesla, the frequency and quality factor first decreased as the magnetization in the magnetic domains started to rotate toward the direction of the external field, and then increased as the entire sample became saturated by the external field. Similar dependence of the resonance frequency on the magnetic field was previously observed in magnetically capped cantilevers [75]. Figures 4.6 also demonstrate noticeable hysteresis in the response, with the upward and downward field sweeps giving different results. Other modes of the beam produced similar-looking graphs. We could therefore conclude that the cobalt film on the resonator was indeed ferromagnetic.

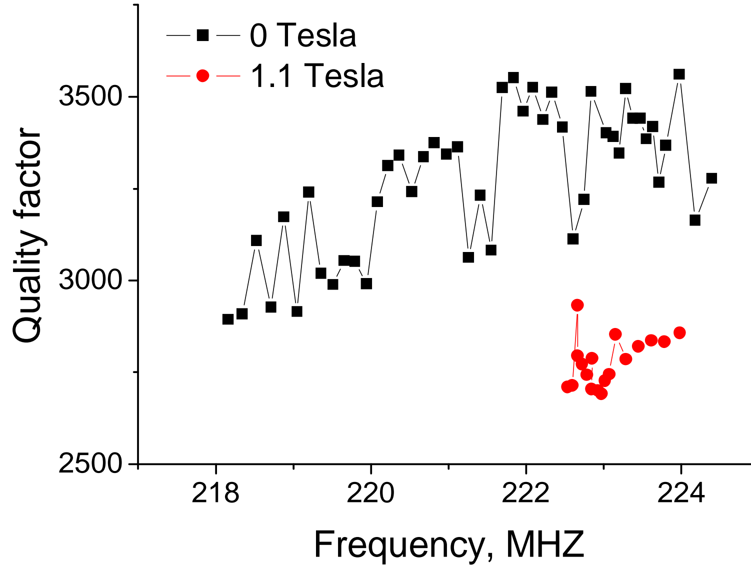

Figure 4.7: Changes in quality factor during adsorptive tuning of a beam with ferromagnetic film (device no. N1B3).

Next, we needed a way to measure the expected small change in the resonator amplitude and quality factor due to interaction with spins. In principle, we could tune the frequency of the resonator through the expected NMR frequency and observe a dip in the resonator's quality factor on resonance. Unfortunately, the uncertainty in fitted values of the quality factor was typically a few percent, of the same order of magnitude as the expected change in quality factor due to spin interaction. In addition, the quality factor generally decreased during absorptive tuning, which would mask the changes in quality factor due to NMR resonance. Indeed, we did not observe any anomalous changes in quality factor during tuning, as shown in Figure 4.7. At zero magnetic field, the quality factor decreased slightly over the 6 MHz tuning range, just like in the case of non-magnetic samples. At 1.1 Tesla perpendicular magnetic film, the quality factor was lower (see Figure 4.6), but it also did not display any anomalous behavior over the small tuning range we studied.

Given the difficulty of detecting a small change in quality factor, we tried another method of detecting the spin-resonator interaction that used time-domain measurements. If nuclear spins are driven hard enough with an RF filed, they can become saturated and the amplitude of their response can decrease substantially [62]. If the drive is removed, the spins will eventually de-saturate and

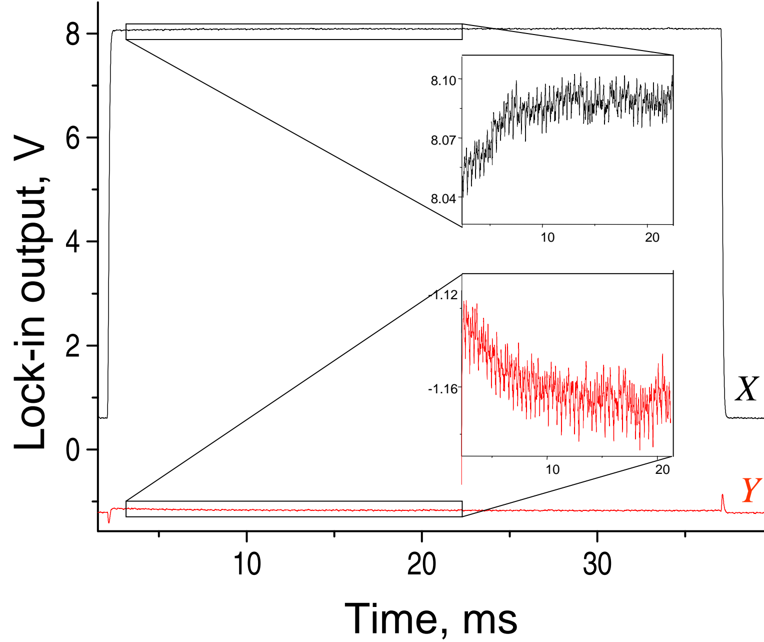

Figure 4.8: Time-domain response of resonator to a pulse drive for the eighth mode of device no. N1B3. Both quadratures of the response, X and Y, are shown. The curves are the result of averaging of 10 thousand pulses with a 5 Hz repetition rate. The insets zoom in on the relevant parts of the graph.

come back to thermal equilibrium. Both saturation and de-saturation occur over a time comparable to the longitudinal relaxation time $T_1 = 1/\Gamma_{\|}$. For cobalt samples, the experimentally determined longitudinal relaxation time varied between 0.2 and 17 ms [76]. By comparison, the relaxation time of resonator motion is $Q/\omega_r \approx 3000/(2\pi \times 225\ \text{MHz}) \approx 2\,\mu\text{s}$ for the eighth mode of the beam considered above. Therefore, the resonator dynamics are much faster than the saturation dynamics of spins, and we can use a mechanical resonance to both drive and probe the saturation of spins.

One way to detect saturation is to look at the response of the beam to a rectangular drive pulse. After the first few microseconds of the transient response of the resonator, its amplitude will reach a steady state whose amplitude will depend on the state of the spins. If the amplitude of the beam motion is not sufficient to saturate the spins, the steady-state amplitude will remain the same as long as the drive is maintained. On the other hand, if the beam motion creates enough local RF field in the ferromagnetic film to saturate the spins, the steady-state amplitude will increase on the time scale of T_1 as spins become saturated.

We have performed these measurements for the eighth mode of the beam N1B3 at 223.5 MHz and the results are shown in Figure 4.8. The resonator response does have some relaxation-like features with a relative change in resonator amplitude of 2% and a characteristic time scale of approximately 5 ms. The changes were in both quadratures of the signal, corresponding to an increase in the amplitude and a simultaneous decrease in resonance frequency. However, these features were completely independent of the magnetic field. We also observed the same features when we tuned the resonator frequency to 219 MHz and in the response of the 7th mode of the resonator at 190 MHz. All of this suggested that these features were unrelated to spin dynamics. One possibility is that they were caused by the changing temperature of the resonator as it responded to the heating pulses of thermoelastic drive.

Thus our attempts to find signatures of coupling between the motion of a nanomechanical mechanical did not yield positive results and we can only speculate about the reasons. It is possible that the enhancement factor in evaporated films is much lower than in powder samples. It is equally possible that the nuclear magnetic resonance in these samples was too broad or occurred at a significantly lower frequency.[6] Given these negative initial results and the substantial effort needed to fabricate new resonators of the kind shown in Figure 4.5 and troubleshooting the problems, we decided to pursue other experiments.

Despite our results, I remain confident that experiments of this kind will become feasible in the future. Future increases in the quality factor of resonators as well as their further miniaturization should increase the signal associated with coupling between resonator motion and transverse magnetization of spins, eventually making them detectable. These future advances may also allow experimental realization of new types of spin-resonator dynamics such as the laser-like system proposed in the next section.

[6] We have annealed some devices with ferromagnetic films in a reducing atmosphere, since annealing has been shown to narrow the width of NMR in sputtered films of cobalt [74]; however, the resulting films were non-magnetic.

4.3 Analogy to quantum optics: Cantilaser

In the previous sections, I discussed the physics of the interaction between spins and a nanomechanical resonator. In this section, I will consider the same physics from a different perspective by drawing analogies to quantum-optical systems. In particular, I will consider the analogy between a coupled spin-resonator system and the quantum-optical model of a laser.

The invention of masers and lasers in the middle of the twentieth century [77] has engendered whole new fields of science and myriads of applications. Regardless of the frequency range and other details of a practical implementation, all laser-like devices involve one or more quantum-mechanical oscillators resonantly interacting with a continuously pumped multilevel quantum system. In the ubiquitous optical laser, the oscillator is realized by a mode of a high-Q electromagnetic cavity, a mode resonant with optical transitions of bound electrons in the active medium. Masers use microwave transitions of gas molecules or electron spins of a paramagnetic solid in a strong magnetic field. Finally, the active medium of a free-electron laser is a relativistic electron beam, whose energy levels can be defined by a specially configured magnetic field [78].

This relative diversity of possible realizations of the active medium is not, however, matched by the demonstrated realizations of the other essential part of a lasing system, the oscillator. We are aware of only one laser-like device that used an oscillator different from a field mode of an electromagnetic cavity—the nuclear-magnetic-resonance (NMR) laser [79]. In that device, nuclear spins of a solid sample were inductively coupled to a resonant LC circuit. Although many properties of an LC circuit are strikingly different from those of a cavity resonator, one can argue that the underlying physics in the two cases is the same: The oscillations correspond to normal modes of a complex electromagnetic system, whether it consists of an electromagnetic field confined by reflecting walls or of coupled electric and magnetic fields of capacitive and inductive elements.

Here, we propose a laser-like device in which the oscillator is realized by a fundamentally different kind of a device—a nanomechanical resonator, e.g., a nanoscale cantilever or doubly clamped beam. High resonance frequencies, high quality factors, and low noise of nanomechanical resonators make it possible to use their long-term coherent response in a laser-like device. Similarly to the case of the

NMR laser and solid-state masers, we propose to use nuclear or electron spins in a strong external magnetic field as the active medium of a "mechanical laser". A nanomechanical oscillator can be effectively coupled to the magnetic moments of such spins by incorporating a small ferromagnetic tip on its surface. At microscopic distances between the cantilever and the sample, the coupling between the tip and the spins is essentially magnetostatic.

Systems consisting of a micro- or nanomechanical cantilever coupled to resonant magnetic spins of a solid sample have been extensively studied in the context of magnetic resonance force microscopy (MRFM) [66]. However, in all MRFM experiments performed so far, the fundamental frequency of the cantilever was orders of magnitude below the Larmor frequency of the magnetic spins. Resonant transfer of energy quanta from spins to the mechanical oscillator is impossible in this case. Instead, an RF or microwave field is used to modulate the sample magnetization at the cantilever frequency [66].

For the device proposed here, it is essential that the motion of the mechanical oscillator be resonantly coupled to the free precession of magnetic spins, which means that the frequency of the used mechanical mode must be close to the Larmor frequency of the sample [68]. For conventional experiments with external magnetic fields of a few Tesla, the Larmor frequencies are on the order of tens of megahertz and tens of gigahertz for nuclear and electron magnetic resonance, respectively [62]. Given that the highest fundamental-mode frequency of lithographically defined nanomechanical oscillators measured so far is slightly above 1 GHz [17], resonant coupling between mechanical oscillators and electron spins in strong magnetic fields seems unfeasible at this time. Operation in low magnetic fields, on the other hand, would prevent complete polarization of electrons and make the system more sensitive to ambient magnetic fields. We will therefore focus on the case of nuclear spins.

Figure 4.9 shows a schematic of the proposed device. A nanomechanical oscillator—a cantilever in this case—is positioned near a sample that contains precessing nuclear spins, some of which are shown schematically in the figure. A ferromagnet on the cantilever tip creates a magnetic field, which can be approximated as the field of a magnetic dipole. When superimposed on the uniform external field $\mathbf{B_0}$, this field modifies the total magnetic field seen by nuclear spins and, therefore,

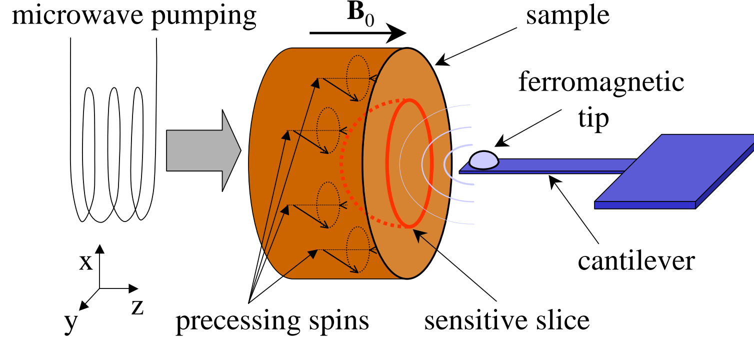

Figure 4.9: Schematic of a mechanical laser device.

their Larmor frequency. As a result, only a certain slice of the sample, known as the sensitive slice, will have the Larmor frequency resonant with the frequency of the used mode of the cantilever [66].

As we discussed in the previous section, the rotating transverse component of nuclear magnetization couples to the ferromagnetic tip via dipolar magnetostatic interaction, with the resulting force driving cantilever oscillations. Conversely, a moving ferromagnet creates an AC magnetic field that can drive transitions between Zeeman levels of nuclear spins—stimulated transitions in the language of standard rate-equation laser theory. The resulting coupled interaction—spins driving the cantilever and the cantilever, in turn, driving the spins—leads to a kind of positive feedback that arises in all laser-like systems.

Although a variety of nanomechanical devices could be used—involving, for example, torsional or flexural modes—we focus here on nanocantilevers, which are especially convenient for scanning with small tip-sample separations. The device we propose can then be aptly termed a "cantilaser". To provide a concrete example, we will assume the following parameters for the cantilever: fundamental-mode frequency $\omega_c/2\pi = 20$ MHz, effective spring constant $k_c = 0.1$ N/m, quality factor $Q = 10^5$, the transverse magnetic field gradient (due to the ferromagnetic tip) $\frac{\partial \mathbf{B}_\perp(\mathbf{r})}{\partial x} = 1$ G/Å$= 10^6$ T/m within the sensitive slice. This magnetic field gradient can be created by a rare-earth-metal magnet at a distance of about 1 micron [9, 81]. At such relatively large distances, one can usually neglect all nonmagnetic interactions between the cantilever and the sample. Note also that the intrinsic Q factor of a nanomechanical oscillator can be effectively increased by a few orders of magnitude using

positive feedback [82] or parametric pumping [83].

For the parameters of the nuclear spin subsystem, we will take values representative of crystalline materials [62]: transverse relaxation time $T_2 = 50\,\mu$s and nuclear gyromagnetic ratio $\gamma_n = 2\pi \times$ 10 MHz/T. The bulk of the sample material will be resonant with the cantilever oscillations in an external field of $B_0 = \omega_c/\gamma_n = 2$ T.

In order to observe lasing in any system, one must introduce a pumping mechanism to compensate for the energy dissipated in both the oscillator and the active medium. For nuclear spins, such pumping can be produced by dynamic nuclear polarization (DNP) [62]. In this mechanism, microwave or optical radiation is used to saturate an electron transition, causing them to preferentially absorb photons of only one circular polarization. Some of the absorbed angular momentum is then transferred from the electrons to the nuclei of the sample through various equilibration processes. This technique has been successfully employed to pump the NMR laser at the liquid helium temperature (4.2 K) using a microwave source as in Figure 4.9, with the effective pumping time as low as $T_p = 0.2$ s [79]. We will use this pumping rate and the equilibrium longitudinal polarization $M_{eq} = -0.3$ that is achievable in a 2-Tesla external field.

The dynamics of the cantilaser can be described by the Hamiltonian

$$\hat{H} = \hbar\omega_c \hat{a}^\dagger \hat{a} + \hbar\gamma_n \sum_i \mathbf{B}_i \cdot \hat{\mathbf{S}}_i + \hbar(\hat{a}^\dagger + \hat{a}) \sum_i 2\mathbf{g}_i \cdot \hat{\mathbf{S}}_i + \hat{H}_r,$$

where $a^\dagger$ and a are the creation and annihilation operators of the cantilever mode, $\hat{\mathbf{S}}_i$ is the spin operator of ith nucleus, $\hat{\mathbf{B}}_i$ is the the external field at the site of the ith spin, $\mathbf{g}_i = \frac{\gamma_n}{2} \frac{\partial \mathbf{B}(\mathbf{r}_i)}{\partial x} \sqrt{\frac{\hbar\omega_c}{2k_c}}$ is the vector constant of the coupling between the ith spin and the cantilever, and $\hat{H}_r$ describes relaxation-inducing couplings to the environment. This Hamiltonian was first considered by Jaynes and Cummings, who used it describe quantum behavior of masers [84]. In the same paper, they also showed that the corresponding dynamics can usually be described by semiclassical equations, which treat the resonator classically and the spins quantum mechanically.

Considering the nuclear spins in their respective rotating frames (as defined by the local field

$\mathbf{B}_i$ and field gradient $\frac{\partial \mathbf{B}(\mathbf{r}_i)}{\partial x}$ [68]) and using the slowly varying amplitude approximation for the cantilever, we can write such semiclassical equations in the form

$$\begin{aligned} &\dot{A} + \kappa A = -gNM_-, \\ &\dot{M}_- + \Gamma_\perp M_- = gM_z A, \\ &\dot{M}_z + \Gamma_\parallel (M_z - M_{eq}) = -g(M_- A^* + M_-^* A)/2, \end{aligned} \tag{4.6}$$

where A is the (generally complex) amplitude of cantilever oscillations, normalized by the amplitude, $\sqrt{\hbar\omega_c/(2k_c)} \approx 2.6 \cdot 10^{-13}$ m, of zero-energy quantum motion, $\kappa = \omega_c/2Q \approx 630\,\mathrm{s}^{-1}$ is the cantilever decay rate, N is the number of resonant spins in the sensitive slice, M_- and M_z are the normalized ($|M_-|^2 + M_z^2 \leq 1$) transverse and longitudinal (with respect to $\mathbf{B_0}$) components of nuclear polarization, $\Gamma_\perp = T_2^{-1} = 20 \cdot 10^3\,\mathrm{s}^{-1}$ and $\Gamma_\parallel = T_p^{-1} = 5\,\mathrm{s}^{-1}$ are the effective transverse and longitudinal polarization relaxation rates, and $g = \frac{\gamma_n}{2} \left| \frac{\partial \mathbf{B}_\perp(\mathbf{r})}{\partial z} \right| \sqrt{\frac{\hbar\omega_c}{2k_c}} \approx 8.0\,\mathrm{s}^{-1}$ is the scalar coupling constant of the interaction between the cantilever and the nuclear spins.

In Eqns. (4.6) we implicitly assumed that all resonant nuclei in the sensitive slice are spin-half and that they all see the same strength and gradient of the magnetic field. The latter is an obvious simplification since in MRFM experiments, the magnetic-resonance frequency and coupling strength varies continuously over the sensitive slice [80]. However, the same problem of inhomogeneous broadening and nonuniform coupling arises in most quantum optics and laser setups [85], and it was found experimentally [86, 87] that equations of the form (4.6) still correctly reproduce most features of the coupled spin–oscillator dynamics. We will therefore restrict our analysis to the simplest model of Eqns. (4.6)

It is easy to find the steady-state solutions of Eqns. (4.6). The nontrivial lasing solution may exist only in the case of population inversion, $M_{eq} < 0$, and is given by $A_{cw} = \sqrt{(N|M_{eq}| - N_t)\Gamma_\parallel/\kappa}$, where $N_t = \kappa\Gamma_\perp/g^2$ is the threshold population inversion. Substituting $M_{eq} = -0.3$ and other parameter values given above, we find that in order to support continuous-wave (cw) lasing, the number of atoms in the sensitive slice should be $N > N_{cw} = N_t/|M_{eq}| \approx 0.65 \cdot 10^6$. This may seem like a large number; however, even an atomically thin sensitive slice of a homogeneous sample

contains on the order of 10^7 nuclei if the diameter of the sensitive slice is just $1\,\mu$m. Much larger sensitive slices have been used in nuclear MRFM experiments so far, so exceeding the lasing threshold seems quite feasible.

One of the more interesting transient phenomena predicted by the Jaynes–Cummings model is the coherent oscillation of population between the oscillator and spins [84], an effect similar to the oscillations of energy between two weakly coupled classical harmonic oscillators. Also known as ringing superradiance, this phenomenon has been observed in different quantum-optical systems [86, 87]. In order for the energy oscillations to be observable in a cantilaser, the effective frequency of the oscillations, equal to $\sqrt{|M_{eq}|N}g$ [84], should be larger than the fastest relaxation rate of the system, $\Gamma_\perp$. We can therefore roughly estimate the minimum number of atoms necessary to observe the oscillations as $N_{sr} = \Gamma_\perp^2/(|M_{eq}|g^2) \approx 20 \cdot 10^6$. As we show below, our numerical simulations support the validity of this estimate.

Another interesting transient predicted by the Jaynes-Cummings model is a solitary pulse that irreversibly depletes the energy stored in the active medium. Known as giant pulses in the standard laser theory [85], these transients can appear if $\Gamma_\perp > |M_{eq}|Ng^2/\Gamma_\perp > \kappa$, which implies $N_{sr} > N > N_{cw}$. Such a giant pulse reduces the population inversion to zero and therefore consumes one half of the total potential energy of the active medium (i. e., the sensitive slice, which can in principle be adjusted to encompass most of the sample [80]). This is in contrast to the case of ringing superradiance, where all of the available energy oscillates back and forth between the cantilever and spins.

Figure 4.10 shows three characteristic transient outputs of a cantilaser, obtained by numerical integration of Eqns. (4.6) using the Mathematica software package. As the number of resonant nuclei in the sensitive slice decreases from $N = 200 \cdot 10^6 \gg N_{sr}$ to $N = 5 \cdot 10^6 \ll N_{sr}$, the frequency and amplitude of energy oscillations decreases until just one “giant” pulse is observed. If one further keeps decreasing the number of atoms, the single pulse becomes longer and smaller in amplitude until it disappears completely as the number of atoms goes below the cw lasing threshold N_{cw}. Note that the tails of the output transients always decay at the time scale of κ^{-1} because cantilever decay is

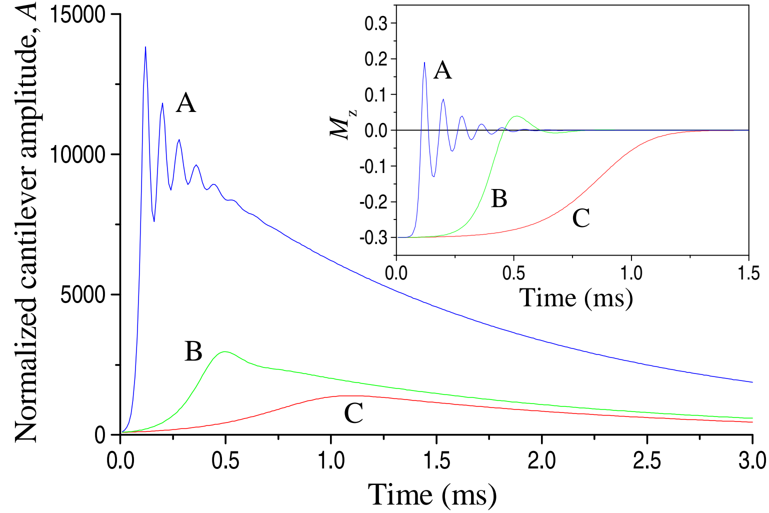

Figure 4.10: Characteristic transients of a cantilaser for different number of resonant nuclei within the sensitive slice: (A) $N = 200 \cdot 10^6$, (B) $15 \cdot 10^6$, and (C) $5 \cdot 10^6$. The main panel shows the normalized amplitude of cantilever oscillations, $A(t)$, the inset shows the longitudinal nuclear polarization, $M_z(t)$. The initial conditions are $A(0) = 94$, $M_-(0) = 0$, $M_z(0) = -0.3$.

the dominant mechanism of energy dissipation here. In contrast, the coherent oscillations, if present at all, decay at the time scale of $\Gamma_\perp^{-1} = T_2$ since spin-spin relaxation is the dominant mechanism for the loss of coherence.

The initial conditions for pulsed transients used in the simulations of Figure 4.10 can be produced by a Q-switching technique [85]. Note that the initial nuclear polarization, $M_-(0) = 0$, $M_z(0) = M_{eq}$, is simply the equilibrium polarization achieved in the presence of dynamic nuclear pumping and negligible interaction with the cantilever. Also, the initial normalized cantilever amplitude corresponds to thermal vibrations of the cantilever at the temperature $T = 4.2$ K: $A(0) = A_{th} = \sqrt{2k_BT/(\hbar\omega_c)} \approx 94$, where k_B is the Boltzmann constant.

Since a cantilaser shares so much in its design and principles of operation with MRFM setups, it is natural to consider whether the effects described above can be used to improve the sensitivity of nuclear MRFM. The single-shot sensitivity of the first nuclear MRFM experiment [65] was approximately 10^{13} thermally polarized nuclear spins at room temperature or about 10^{11} nuclear spins at 4.2 K (nuclear polarizability is inversely proportional to temperature). Since then, the sensitivity of MRFM experiments has been improved to 1 Bohr magneton [8], a magnetic moment that is created

by roughly 10^6 nuclear spins at 4.2 K. The closest competing technology—scanning SQUID-based magnetometry—has so far demonstrated a sensitivity of 10^5 Bohr magnetons [88], or 10^{11} nuclear spins at 4.2 K.

To consider the MRFM sensitivity of a cantilaser, we will calculate the ratio of power spectral density of lasing outputs to the power spectral density of thermomechanical noise. Since the resonant frequency of the cantilever and the Zeeman transition frequency of spins coincide, we can express all energy quantities in terms of the number of energy quanta $\hbar\omega_c$. The power of the thermomechanical noise is then proportional to $n_{th} = A_{th}^2/2 = k_B T/(\hbar\omega_c) \approx 4400$, and its bandwidth is $\Delta\omega_{th} = \kappa$. Well above the lasing threshold, the power of the cw lasing signal is $n_{cw} = A_{cw}^2/2 \approx \Gamma_{\parallel} N|M_{eq}|/(2\kappa) \approx N/840$, and its bandwidth is $\Delta\omega_{cw} \approx \kappa(n_{th}+1/2)/n_{cw}$ [85]. The signal-to-noise ratio for the cw output is then $SNR_{cw} = \frac{n_{cw}/\Delta\omega_{cw}}{n_{th}/\Delta\omega_{th}} \approx (n_{cw}/n_{th})^2 \approx \left(N/3.7\cdot 10^6\right)^2$. The quadratic increase in SNR_{cw} with the number of atoms reflects the spectral narrowing of the cw signal at high output power, a fact that is well known and used in optical lasers [85].

For both kinds of pulsed outputs we considered (ringing superradiance and single pulses), the efficiency of the energy transfer from spins to the cantilever mode is on the order of unity. The peak cantilever amplitude of a pulse in both cases then corresponds to mode population of about $n_{pulse} = N|M_{eq}|/2$. Since all pulsed outputs eventually decay at the time scale of κ^{-1}, their bandwidth can be taken to be $\Delta\omega_{pulse} \approx \kappa$. Proceeding as above, we find $SNR_{pulse} = N|M_{eq}|/(2n_{th}) \approx N/29000$. A cantilaser operating in the pulsed mode would therefore have a single-shot sensitivity of about $3\cdot 10^4$ nuclear spins at 4.2 K. A large part of this improvement derives from the hyperpolarization of nuclei by DNP processes, but the near-unity efficiency of energy transfer between spins and cantilever in pulsed transients is also significant.

We conclude by considering different possible perspectives upon mechanical lasing—from the standpoints of quantum optics, NMR spectroscopy, and MRFM. From the perspective of quantum optics, the cantilaser is very similar to a cavity QED system [89], albeit one with weak coupling strength, $g \sim \Gamma_{\parallel} \ll (\Gamma_{\perp}, \kappa)$, and high thermal population, $n_{th} \gg 1$. Since such combinations of parameters are not available in quantum optical systems or NMR laser, this opens up new possibilities

for studying coherent quantum phenomena in coupled oscillator–atom systems.

In conventional NMR studies, the possibility of a positive feedback between the sample and the detecting resonance circuit has been long recognized. Bloembergen first considered the back action of the detecting coil on the sample almost 50 years ago [90]. Unfortunately, such back action tends to shorten the signal pulses and therefore broaden spectral features. This explains why this positive-feedback effect, known to NMR practitioners as radiative damping, is generally undesirable in high-resolution NMR spectroscopy. In contrast, MRFM experimentalists are not interested in fine details of NMR spectra. Since the ultimate goal of MRFM is atom-by-atom 3D mapping of nanoscopic objects, the required spectral resolution should only be sufficient to distinguish between different nuclear species. MRFM practitioners are therefore willing to trade fine spectral resolution for signal strength and spatial resolution. This is exactly what a mechanical laser provides, by fully exploiting the positive feedback in the coupled oscillator–spin system.

Chapter 5

Studies of quality factors of nanomechanical resonators

The sensitivity of NEMS sensors depends on the mechanical quality factor of the resonator, with higher quality factors generally resulting in higher sensitivities. The quality factor characterizes the loss of mechanical energy in the mechanical resonator due to friction or other dissipation mechanisms:

$$Q \equiv \frac{\omega_R}{\gamma} \equiv \frac{\omega_R E_{res}}{P_{diss}}, \tag{5.1}$$

where ω_R is the resonance frequency, $\gamma \equiv P_{diss}/E_{res}$ is the energy loss rate, P_{diss} is the average power dissipated by the resonator, and E_{res} is total energy stored in the resonator. Devices with higher quality factors feature low mechanical loss, which makes them more sensitive to external perturbations. For example, the thermomechanical noise floor of a nanomechanical force sensor is given by $\sqrt{\frac{4k_B T k_r}{Q\omega_r}}$, where k_B is the Boltzmann constant, k_r is the effective spring constant of the resonator, ω_r is the resonance frequency, and Q is the quality factor. Similarly, the mass sensitivity of a nanomechanical resonator scales as $\frac{\sqrt{S_N}}{2QA}$, where S_N is the spectral density of displacement noise and A is the amplitude of the displacement signal. Despite the importance of quality factors in sensing applications, we have only limited understanding of the physical processes that determine quality factors of nanomechanical resonators in either vacuum or viscous environments like air.

A number of physical mechanisms have been studied in an effort to explain the observed quality factors of resonators in vacuum. Thermoelastic losses [91] are caused by the motion-induced

compression, which leads to heating and irreversible heat flow between different parts of the resonator. In microscale resonators, thermoelastic losses sometimes do explain the experimental quality factors [92]. However, in nanoscale resonators, the predicted damping rates due to thermoelastic damping are generally much smaller than those observed experimentally [91], suggesting that other mechanisms limit the quality factors in practice.

Clamping losses, also called support or anchor losses, are another mechanism that has been studied to explain the observed quality factors of micro- and nanoscale resonators [93, 94, 95, 96]. Clamping losses appear because the points where oscillators are attached to the substrate are never perfectly motionless. Instead, real resonators slightly deform the substrate near the clamping points, which produces sounds waves radiating away from the clamping point through the substrate. The energy of these sound waves is generally dissipated in the substrate, which means that the resonator loses energy due to this process.

The magnitude of clamping losses is determined purely by the geometry and elastic properties of the resonator and the substrate. However, calculating the clamping losses is generally not a simple task. Analytical formulas for the clamping losses of doubly clamped beams and cantilevers have been derived for some special cases of the substrates [93, 94, 95]. For more complicated geometries, the calculations of clamping losses can be done numerically [97]. However, the predictions of these models for the quality factor are generally either too large or too small compared with the experimentally observed values. In addition, most experiments report a clear dependence of the quality factors on the temperature, which is inconsistent with the clamping loss model. All of this suggests that still other mechanisms limit the quality factors in practice.

For the majority of nanomechanical resonators, surface-related losses appear to be the dominant source of mechanical losses. This widely held hypothesis is supported by the fact that the quality factor of nanomechanical resonators generally decreases with decreasing thickness and other resonator dimensions, i. e., increasing surface-to-volume ratio [98, 99, 100, 103]. In addition, the quality factors of nanomechanical resonators have been shown to change after annealing [104] or exposure to ion adsorbates[105]—processes that affect the surface of the resonator.

However, it is presently not known what physical process are responsible for the surface-related losses. Many such processes have been hypothesized, including excitation of adsorbed molecules, movement of lattice defects, and configurational rearrangement. It is likely that the dominant mechanisms of surface-related loss are completely different for resonators of different geometries and material properties. In addition, the dominant loss mechanisms may be different for measurements at room temperature and at cryogenic temperatures.

In other words, the origins of mechanical losses in nanoscale resonators remain something of a mystery. The theoretical work has been sparse and mostly focused on the quantum model of a resonator interacting with a bath of two-level systems [106, 107]. This model predicts a realistic dependence of the quality factor on temperature at low temperatures [106], but does not directly apply to room-temperature measurements. Experimental data is available for a variety of resonator materials, geometries, and temperatures [58, 98, 99, 100, 101, 102, 104, 105, 103], but is difficult to generalize.

In contrast to the case of vacuum, the dominant mechanism of mechanical losses in fluids is clear: it is the damping effect of the surrounding viscous fluid itself. However, the physics describing the relevant fluid dynamics can be very complicated. For example, in gas environments, the traditional continuum model of viscous fluids breaks down when the mean free path of gas molecules becomes comparable to the resonator dimensions [108]. In such cases, it becomes more appropriate to use the free molecular flow model, which generally predicts higher quality factors than the continuous model [108]. This improved quality factor of narrow nanoscale resonators has been observed experimentally [5, 109].

In the case of liquids, where the continuous model is generally adequate, Sader and coworkers have developed semi-analytical models to predict the frequencies and quality factors of out-of-plane and torsional modes [111, 112]. Experimental measurement of microscale cantilevers have borne out such predictions [110]. Using numerical simulations, Cross and coworkers have considered damping and the associated noise spectra in liquids [113]. Paul and coworkers have also considered additional damping mechanisms that appear when a resonator is situated close to a solid wall [114]. For

nanoscale resonators, there is a need for theoretical work modeling the quality factors of in-plane beam modes and other mode types, such as plate resonator modes.

In this chapter, I describe our measurements of quality factors of nanomechanical resonators in both vacuum and air. Using thermoelastic actuation and piezoresistive detection, we have been able to measure the quality factors of multiple out-of-plane and in-plane modes of doubly clamped beams. These measurements also suggested alternative resonator designs that would feature reduced mechanical losses in fluids; I present preliminary designs and measurements of such resonators as well.

5.1 Quality factors of flexural modes of beams in vacuum[1]

A number of experimental studies have reported measurements of quality factors for resonators of different geometries [98, 99, 100, 101, 103]. The majority of these measurements were done for the fundamental out-of-plane modes of cantilevers or doubly clamped beams, with each resonator providing just one data point. As a result, fabrication imperfections, which are usually different for each device, introduce additional scatter into the observed dependence of the quality factor on geometric parameters.

In this section, I describe series of measurements of multiple modes of the doubly clamped beams in high vacuum ($p \ll 1$ mTorr). These measurements may provide more reliable clues about the causes of mechanical loss in nanomechanical resonators because each resonator provides multiple data points. In this configuration, any fabrication imperfection would systematically affect all measured modes.

Figure 5.1 shows the measured vacuum quality factor versus frequency for the in-plane and out-of-plane modes of the doubly clamped beams that we have studied the most: a 16-μm-long SiC beam (E7A3) and an 8-μm-long SiC beam (E5C2). We measured many more modes than shown in Figure 5.1—at even higher frequencies—but we could not clearly identify them as in-plane our out-of-plane. We identified modes using the results of finite element simulations and the amplitude

[1]Measurements described in this section were performed in collaboration with I. Kozinsky.

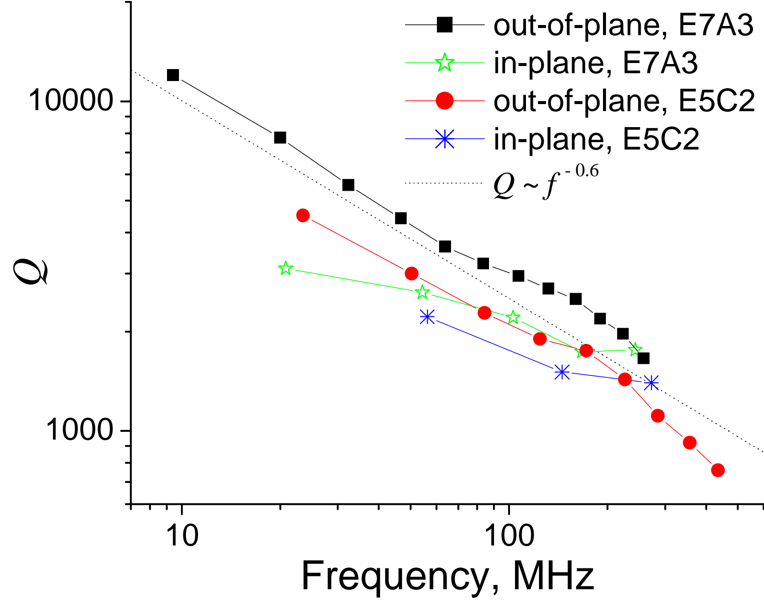

Figure 5.1: Measured quality factors versus frequency for the in-plane and out-of-plane modes of a 16-μm-long SiC beam (E7A3) and a 8-μm-long SiC beam (E5C2).

of measured response (in-plane modes generally produce a smaller amplitude of piezoresistive signal for the geometries we used—see section 2.3). The modes we could not identify were probably of a mixed nature, resulting from the mechanical interaction between an in-plane and an out-of-plane mode or between a torsional mode and out-of-plane mode.

The first thing that stands out in Figure 5.1 that the quality factor scales with respect to frequency differently for in-plane and out-of-plane modes. The quality factor of the out-of-plane scales roughly as $Q \propto f^{-0.6}$. We do not have enough data points to fit a scaling relationship for in-plane modes, but the exponent would clearly have to be smaller. As a result, the quality factors of in-plane modes are generally lower than those of out-of-plane modes at low frequencies, but the situation reverses for the high-frequency modes. Second, the quality factors depend on more than just frequency. The sequences of data points for the 16-μm-long and 8-μm-long devices are clearly offset from each other, despite the fact that they have identical geometries except for the lengths. At the same simlar frequencies, the quality factors of the longer device are approximately 30% larger. This means that these quality factors cannot be explained by a surface loss model that depends purely on the frequency.

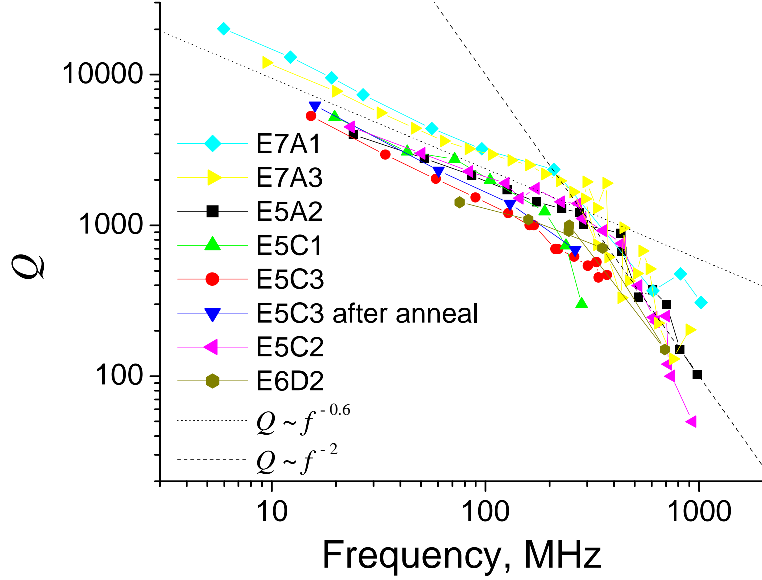

Figure 5.2: Quality factor of the out-of-plane and unclassified modes of multiple SiC beams: 24-μm-long E7A1, 16-μm-long E7A3, 8-μm-long E5A2, 8-μm-long E5C1, 8-μm-long E5C2, 8-μm-long E5C3 (before and after annealing), and 4-μm-long 6D2.

We have performed quality factor measurements on many other silicon-carbon beams, but were not always able to properly classify as many modes as for devices E7A3 and E5C2. For low-numbered out-of-plane modes, we generally observed the same scaling of quality factor $Q \propto f^{-0.6}$, as illustrated by Figure 5.2. Note that this graph also includes the data from devices E7A3 and E5C2, both the out-of-plane modes and the unclassified higher-frequency modes. One interesting set of measurements was provided by the device E5C3, which we measured after fabrication and again after in-situ annealing, which was done by passing DC current through both loops of the device in vacuum and therefore heating the device by an estimated 200 K. After annealing, the frequencies of the out-of-plane modes we measured shifted up by a few percent, probably due to a decrease in mass of surface adsorbates. The quality factors of the measured mechanical modes increased by 15% on average, but the scaling of the quality factor with frequency remained the same. Again, this suggests that the main mechanism of mechanical losses for the out-of-plane modes is related to the surface of the device and possibly the adsorbates on the surface.

Another prominent feature of Figure 5.2 is the apparent knee of the curves occurring at a frequency of approximately 400 MHz. Beyond this frequency, the quality factor seem to decrease with

frequency much faster than $Q \propto f^{-0.6}$. Unfortunately, we were not able to classify most of these high-frequency modes: Some of them are high-numbered out-of-plane modes, but others may be in-plane modes, torsional modes, or modes of mixed nature. Nevertheless, the quality factors of all these high-frequency modes seem to follow a different frequency scaling relationship and are possibly determined by a different physical process than the low-frequency modes.

One candidate for this high-frequency dissipation process is clamping loss. The theoretical prediction for the quality factors of the out-of-plane modes of a doubly clamped beam that is connected to two semi-infinite volumes of bulk material is approximately given by [95, 116],

$$Q \approx 10 \times \frac{l^5}{wt^4\pi^4(n+1/2)^4} \tag{5.2}$$

where l, w, and t are the length, width, and thickness of the beam, n is the mode number, and the derivation assumes that the beam has no tension. This formula predicts unrealistically high quality factors ($Q > 10^6$) for the fundamental and other low-numbered modes of the beams we studied, suggesting that other loss mechanisms are dominant for these modes. However, for high-numbered modes, $n > 10$, the predictions become much closer to the quality factors we observe in practice. For example, if we assume $w = 400$ nm and $t = 80$ nm, the fifteenth mode of an 8-μm-long beam is predicted to have a quality factor of approximately 3800. If we assume $t = 160$ nm, which better describes the combined thickness of the beam itself and the metal loops on the beam ends, the predicted quality factor drops to approximately 240, which is very close to the values we observed. In addition, since for high flexural modes, $\omega_n \propto n^2$, this formula predicts that the quality factor should scale as $Q \propto \omega^{-2}$. This dependence seems to fit the data in Figure 5.2, although the number of data points is not large enough to make any definite conclusions.

Of course, the assumptions used to derive Eqn. (5.2) are not very realistic for the beams we studied. Rather than being connected to an infinite semispace of the same material, the ends of the beam are connected to an approximately 400-nm-long SiC ledge—a membrane that results from the underetching during the suspension stage of the fabrication process. Beyond the ledge, the

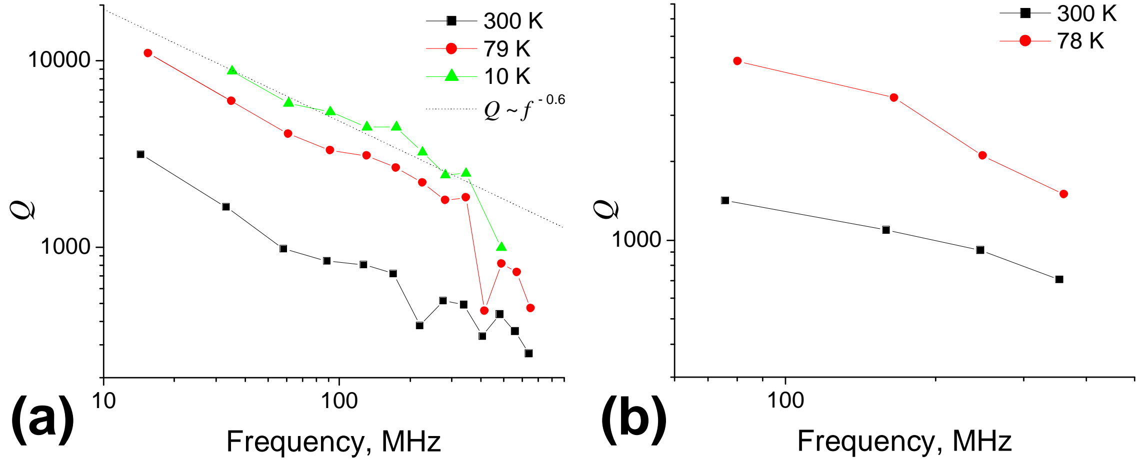

Figure 5.3: (a) Measured quality factors versus frequency for the first eight out-of-plane modes of an 8-μm-long SiC beam with cobalt film (E7D1) at various temperatures. (b) Same for the first four out-of-plane modes of 4-μm-long SiC beam without cobalt film (E6D2).

SiC layer is fixed to the bulk of the silicon chip, whose elastic properties are different from those of silicon carbide. We should therefore use any prediction of Eqn. (5.2) with caution. Still, it is encouraging that the quality factors predicted for high-numbered modes give values comparable to the experimental values.

In addition to plain silicon-carbide devices, we have also measured the quality factors of beams with deposited cobalt films, described in Chapter 4. Figure 5.3(a) shows the measured quality factor of one such beam at three different temperatures. At room temperature, the measured quality factors are approximately twice smaller than those of devices with no cobalt film, but surprisingly, they seem to follow the same scaling law $Q \propto f^{-0.6}$, albeit with more scatter. The same scaling law persists at low temperatures, with the quality factors of low-numbered out-of-plane mode shifting more or less in parallel. This suggests that the same physical mechanism limits the quality factors of low-numbered out-of-plane modes at both room and cryogenic temperatures for devices with and without cobalt films. The strong temperature dependence again contradicts the hypothesis that the quality factor of these low-numbered modes is limited by the clamping loss mechanism.[2] Note, however,

[2]As mentioned in the introduction to this chapter, clamping loss depends only on the geometry and the material properties of the resonator and the substrate. Therefore, clamping loss can exhibit a temperature dependence only to the extent that the geometry and the material properties change with temperature. Both in theory and in practice, these changes in geometry and material properties are quite small—no more than a few percent in the entire temperature range from from 300 K down to 10 K.

that the temperature dependence is less pronounced for the highest detected modes. Going from 300 K to 79 K, the quality factor of these higher modes increases by approximately a factor of two, compared to a factor of four for the low-numbered modes. We also observed similar behavior for the modes of a 4-μm-long SiC beam (Figure 5.3(b)), although it is not as clear because of fewer data points. For both beams, this behavior is consistent with the hypothesis that the quality factors of the high-frequency modes are limited by a temperature-independent mechanism, such as clamping loss.

Overall, the data we collected from beams in vacuum supports the hypothesis that the quality factor of low-numbered out-of-plane modes ($\leq$ 400 MHz) is limited by a surface-related loss mechanism, whereas the quality factor of high-numbered modes ($\geq$ 400 MHz) may be limited by the clamping loss mechanism. However, the surface-related loss mechanism depends on more than just the resonance frequency of the mode: Devices of different lengths have noticeably different quality factors at the same frequencies. We and other members of the Roukes group have also observed that, in order to maximize the quality factor of the fundamental mode, the ledge resulting from underetching should be minimized—larger underetch generally results in lower quality factors. The importance of the clamping conditions was also demonstrated in Ref. [101], where the measured quality factor of a free-free beam was more than twice larger than that of a doubly clamped beam of similar resonance frequency. At the same time, the authors of Ref. [101] argued that the surface roughness strongly affects the observed quality factors of doubly clamped beams. All of this indicates that typical high-aspect-ratio devices fabricated in our group have their quality factors limited by a surface-related loss mechanism that *depends* on the clamping conditions, but unlike the regular clamping-loss mechanism, is *not fully determined* by the clamping conditions.

It is not yet clear what physical processes may underlie such a surface-related, clamping-sensitive loss mechanism. However, it is easy to see why such a mechanism is likely to exist. Whatever microscopic physical process leads to mechanical loss (e.g., motion of defects, motion of surface adsorbates, surface reconfiguration, etc.), the dissipated energy must be transported by phonons away from the beam to the bulk of the substrate. The probability with which these energy-carrying phonons can

escape from the resonator to the outside bulk substrate generally depends on the clamping conditions of the resonator. More rigid clamping conditions generally suppress the transmission of phonons, whereas softer clamping allows phonons to pass through more easily. Therefore, the clamping conditions may easily affect the mechanical loss due to, for example, surface adsorbates because the clamping conditions determine the spectrum of thermal phonons that the surface adsorbates are exposed to. To the best of my knowledge, the thermal spectrum of phonons inside a nanomechanical resonator has not been calculated before, although the phonon density of states (DOS) has been calculated for a nanoparticle weakly coupled to a substrate [115]. A calculation of the thermal phonon spectrum for a cantilever or a beam may shed new light on the problem of surface-related losses in nanomechanical resonators in vacuum.

5.2 Quality factors of flexural modes of beams in air[3]

Apart from measurements of multiple beams in vacuum, we have also systematically measured the quality factors of two SiC beams in ambient air: the 8-μm-long beam E5C2 and 16-μm-long beam E7A3. Tables 5.1 and 5.2 list the results of these measurements. In air, mechanical losses occur due to the same mechanisms as in vacuum and, additionally, the viscous damping of the air. If we assume that the surface-related losses are similar in air and in vacuum[4], we can calculate the contribution to the mechanical losses due to air friction alone. The corresponding viscous-damping-limited quality factor can be calculated using the formula

$$Q_{visc} = \frac{1}{Q_{air}^{-1} - Q_{vac}^{-1}}, \tag{5.3}$$

where Q_{air} and Q_{vac} are the measured quality factors of the mode in air and in vacuum, respectively. The viscous-damping-limited quality factor, Q_{visc}, is the expected quality factor of a beam with no loss mechanisms other than air friction. For the low numbered modes, we have $Q_{vac} \gg Q_{air}$ and

[3] Measurements described in this section were performed in collaboration with I. Kozinsky.

[4] The vacuum measurements described earlier in the section were not performed in ultrahigh vacuum and we did not normally anneal the devices. Therefore, the surfaces of nanomechanical resonators were likely to have similar adsorbates in both air and vacuum.

Mode	f_{vac}	Q_{vac}	f_{air}	Q_{air}	Q_{visc}	Q_{theor}
1st out	9.42	12000	9.35	37	37	42
2nd out	20.0	7750	19.7	67	68	77
1st in	20.8	3110	20.7	130	—	—
3rd out	32.3	5570	32.0	106	108	105
4th out	46.8	4410	46.7	141	146	148
2nd in	54.4	2630	54.3	300	—	—
5th out	63.9	3620	63.8	173	182	181
6th out	83.5	3220	83.4	201	214	215
3rd in	103	2210	103	430	—	—
7th out	107	2950	106	231	250	254
8th out	132	2700	131	263	291	303
9th out	160	2510	159	298	338	366
4th in	167	1740	166	550	—	—
10th out	190	2190	190	330	389	400
11th out	223	1970	222	360	440	437
5th in	243	1760	243	700	—	—
12th out	258	1660	257	375	484	477
13th out	—	—	296	412	—	530

Table 5.1: Experimental resonance frequencies and quality factors in vacuum, f_{vac}, Q_{vac}, and air, f_{air}, Q_{air}, as well as the viscous-damping-limited quality factor calculated from experimental data, Q_{visc}, and theoretically, Q_{theor}, using the theory of Ref. [112]. Data are presented for the lowest thirteen out-of-plane (out) modes and the lowest five in-plane (in) modes of a 16-μm-long beam (device no. E7A3). We could not measure the quality factor of the 13th out-of-plane mode in vacuum because its resonance curve overlapped with the resonance curve of another mode—most likely a torsional mode—of the resonator.

therefore $Q_{visc} \approx Q_{air}$. However, for high numbered modes, Q_{vac} and Q_{air} become comparable and Q_{visc} provides a better picture of the viscous-damping mechanism than Q_{air} by itself.

Figure 5.4 shows the calculated values of Q_{visc} as a function of the resonance frequency in air. The quality factors of both in-plane and out-of-plane modes scale with frequency approximately as $Q_{visc} \propto f^{\,0.8}$. The curves formed by the quality factors of the out-of-plane modes more or less overlap for the two beams. In contrast, the two curves of the in-plane modes are significantly higher than those of the out-of-plane modes. The two in-plane curves are also noticeably different from each other, with the quality factors of the longer beam (E7A3) 20–30% higher than the quality factors of the shorter beam (E5C2) at the same frequencies. For the highest modes, the viscous-damping-limited quality factors reach values on the order of several hundred and one thousand for the out-of-plane and in-plane mode, respectively. However, the same high-numbered modes have

Mode	f_{vac}	Q_{vac}	f_{air}	Q_{air}	Q_{visc}	Q_{theor}
1st out	23.25	4500	23.1	70	71	84
2nd out	50.4	3000	49.7	130	136	168
1st in	56.3	2220	56.2	220	—	—
3rd out	84.2	2280	83.4	180	195	217
4th out	124.4	1900	123.6	230	262	293
2nd in	145.2	1510	144.9	410	—	—
5th out	172.3	1750	171.4	280	333	387
6th out	226.1	1430	225.2	350	463	453
3rd in	272.1	1400	271.6	570	—	—
7th out	285.3	1110	284.5	400	625	521
8th out	356.6	920	355.7	340	539	609
9th out	435.4	760	434.6	370	721	719
4th in	520.6	400	520.2	320	—	—

Table 5.2: Same as Table 5.1 for the lowest 9 out-of-plane (out) modes and the lowest 4 in-plane (in) modes of a 8-μm-long beam (device no. E5C2).

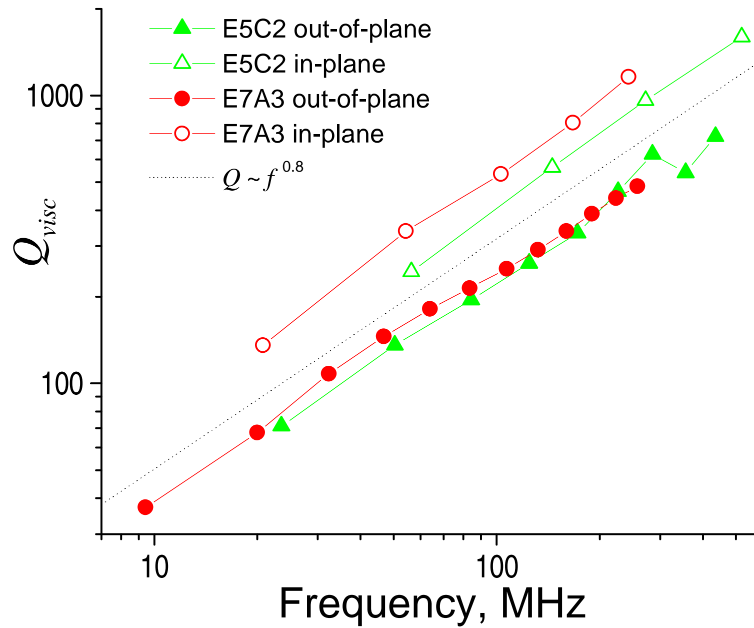

Figure 5.4: Calculated quality factors Q_{visc} due viscous damping in air for various modes of the 8-μm-long beam E5C2 and 16-μm-long beam E7A3.

relatively low quality factors in vacuum, which limits the maximum available quality factor in air, Q_{air}, to approximately 400 and 550, respectively.

Apart from experimental data, Tables 5.1 and 5.2 also show the theoretically calculated viscous-damping-limited quality factors for the out-of-plane modes. For these calculations we used the theory of Sader and coworkers [111, 112], which was originally developed for cantilever resonators, but can be easily generalized to doubly clamped beams. The agreement between theory and experiment is generally good, especially for the higher modes. The theoretical predictions for the lowest out of plane modes deviate from the experimental values by 10-20%. There are a number of possible explanations for this discrepancy. First, the existence of the nearby substrate may play a role in experiment, especially at the lowest frequencies, where the viscous penetration depth is largest. In contrast, the theory of Sader and coworkers was derived for a beam in an empty space. Second, the continuous fluid approximation used by Sader and coworkers is not strictly applicable to our beams, because the mean free path of approximately 70 nm in air at normal pressure is comparable to the dimensions of our beams. Other mechanisms my play a role too, and further theoretical and experimental study is needed to clarify the cause of the discrepancy.

Interestingly, the theory of Sader and coworkers predicts that resonators of different length but identical thicknesses and widths should have similar quality factors of out-of-plane modes at similar resonance frequencies. This is indeed the case for the out-of-plane modes in our experiments, as can be seen from the overlapping curves in Figure 5.4. In contrast, the quality factors of the in-plane modes do not overlap, but rather are offset from each other by an approximately constant factor. At this point, we do not yet have reliable theoretical predictions of quality factors for in-plane modes, so it is difficult to pinpoint the likely reason for this offset.[5] The development of such a theory in the future will allow us to optimize the geometries of in-plane resonators for high quality factors in air.

[5] John Sader and his student Doug Brumley are currently developing a theory of viscous damping for in-plane flexural modes.

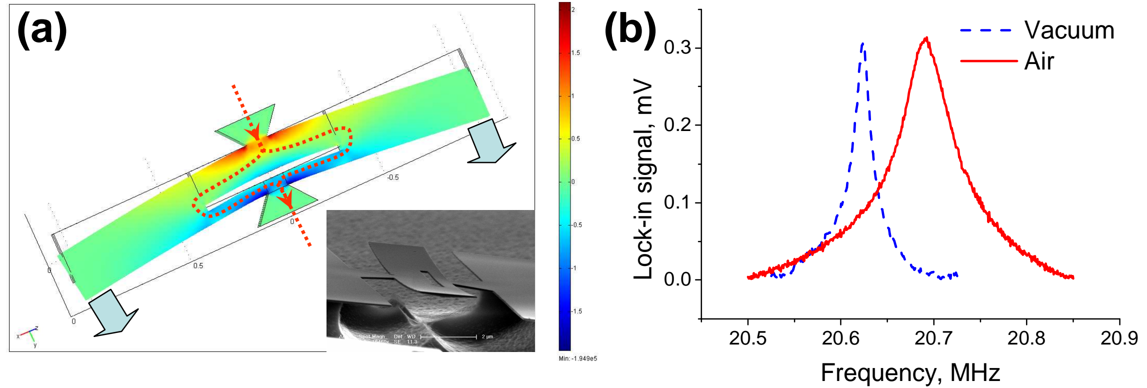

Figure 5.5: (a) Finite element simulation of the in-plane mode of a center-supported SiN beam resonator. The color codes the extensional strain along the length of the beam. The arrows indicate the primary direction of the deflection. The red dotted lines show the current paths used for detection and actuation. Inset shows a scanning electron micrograph of the actual device A1D1. (b) Resonance curves of the in-plane resonance in vacuum and air.

5.3 Alternative resonator designs for high quality factors in fluids

The quality factor studies of the previous section can be used to determine the design principles for resonant sensors with high quality factors in viscous environments, which would enable high-sensitivity measurements in air or liquid. Such devices would be very useful, for example, in gas sensing applications (Chapter 5.7). Some of the in-plane mode resonances described in the previous section featured viscous-damping quality factors Q_{visc} on the order of one thousand. However, all of these modes were difficult to measure because we designed the thermoelastic actuators and the piezoresistive detectors of these beams for measuring out-of-plane rather than in-plane modes. As a result, these modes required high drive and bias voltages to produce a measurable resonance response. This motivated me to look for alternative resonator geometries that would feature viscous-damping-limited quality factors of over 1000 in air and would still be easy to measure.

Figure 5.5(a) shows the first geometry I have studied. This type of a resonator is essentially a beam that is supported in the center rather than at the ends. Alternatively, it can be viewed as two cantilevers joined together. The central support prevents the existence of tension, which can significantly modify the frequency of doubly clamped beams. In addition, according to finite

element simulations, this geometry is much less sensitive to the depth of the underetch that appears during the suspension stage of the fabrication. The non-existence of tension and the low sensitivity to underetch should minimize the variations in the resonance frequency of such device due to fabrication imperfections. Such resonators should therefore be particularly useful as elements of resonator arrays, described in Chapter 6.

The resonances of such devices can be detected using the two-port measurement scheme described in Appendix B. The electric currents used for piezoresistive detection and thermoelastic actuation enter the resonator through one side at the clamping point, flow away from the center of the beam in opposite directions, then come back towards the center and exit the beam on the other side. The slit in the middle of the beam, which creates the two diverging current paths, is intentionally off-center. The asymmetry concentrates both the Joule heat used for actuation and the strain used for detection in the narrower part of the current path. As a result, I could effectively actuate and detect the fundamental in-plane mode of the beam, shown in Figure 5.5(a).

I fabricated these resonators from 100-nm-thick silicon nitride (SiN) covered with a 60-nm-thick gold film. The inset of Figure 5.5(a) shows an SEM image of a device that was 20 μm long and 2 μm wide. Figure 5.5(b) shows the experimentally measured resonance curves of this device in vacuum and air. The experimentally measured resonance frequency in vacuum was approximately 20.6 MHz, which agrees reasonably well with the resonance frequency of approximately 21.3 MHz predicted by the finite element simulations. One possible source of the discrepancy is the fact that the silicon nitride layer was partially etched during the suspension stage of the fabrication. The fitted quality factors in air and in vacuum were $Q_{air} \approx 440$ and $Q_{vac} \approx 1400$, corresponding to $Q_{visc} \approx 650$. Surprisingly, the resonance frequency was larger in air than in vacuum. This behavior differs from what we observed for all the in-plane modes of doubly clamped beams, and I do not currently have a good explanation for it.

I have also studied the extensional mode of the center-supported beams, shown in Figure 5.6(a).[6] I have measured these modes in SiN-gold bilayer devices and in devices made of only a 60-nm-thick

[6] The extensional mode of a ZnO-SiN resonator was recently demonstrated to be effective for gas sensing [117].

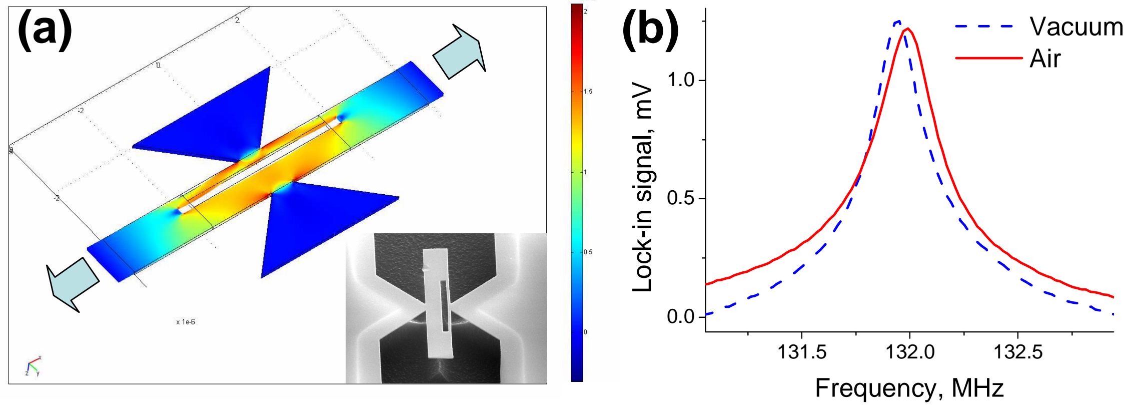

Figure 5.6: (a) Finite element simulation of the extensional mode of a center-supported gold beam resonator. Inset shows a scanning electron micrograph of the device. (b) Resonance curves of the extensional resonance in vacuum and air.

gold film. The gold devices do not suffer from partial etch of the silicon-nitride layer and are therefore easier to model. The inset of Figure 5.6(a) shows an SEM image of a 10-μm-long, 1-μm-wide gold device. Figure 5.6(b) shows the measured resonance curves of this device in vacuum and air. In vacuum, the measured resonance frequency was approximately 132 MHz, which agrees with predicted frequency of 133 MHz. The fitted quality factors in air and in vacuum were $Q_{vac} \approx 540$ and $Q_{vac} \approx 680$, corresponding to $Q_{visc} \approx 2500$. Again, the resonance frequency was larger in air than in vacuum.

For both in-plane flexural and the extensional modes of the center-supported beams, the viscous-damping-limited quality factors, Q_{visc}, were quite large. However, the actual quality factors in air were lower because other loss mechanisms, described by Q_{vac}, were significant for these devices. In the case of the SiN-gold resonator, the low quality factor in vacuum was probably due to the partial etching of the SiN layer, which made the bottom surface of the resonator very rough. In the case of the gold resonator, its quality factor in vacuum was expected to be low because metal-based resonators generally exhibit lower quality factors than semiconductor-based ones. I expect the vacuum quality factors to be significantly larger for well-processed semiconductor center-supported beams. Such resonators should have $Q_{air} \approx Q_{visc}$ and therefore provide better sensitivity, for example, in gas-sensing applications in air.

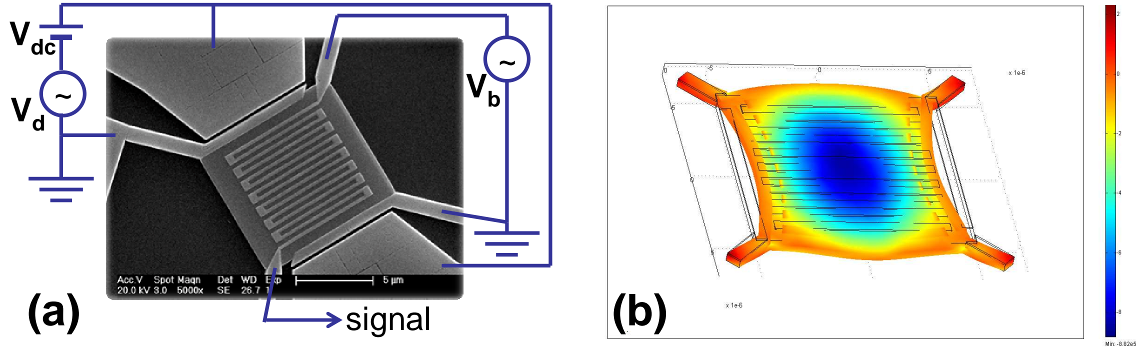

Figure 5.7: (a) Scanning electron microscope of a 10-μm-side plate resonator (before being suspended) and a schematic of the connections to the drive, bias, and detection circuitry. The brighter colors in the SEM image correspond to the metal electrodes and the serpentine metal piezoresistor made out of 50-nm-thick AlSi film. (b) Finite-element simulation of the Lamé mode of a 10-μm-side plate. The color codes extensional strain in the direction in the horizontal interaction. The predicted resonance frequency is approximately 325 MHz.

The final resonator geometry we have considered but not yet measured is that of a plate resonator, shown in Figure 5.7. In particular, we are interested in the in-plane plate modes, such as extensional (breathing) mode, wineglass and Lamé plate modes. Compared to out-of-plane and in-plane flexural resonators, in-plane modes of plate resonators of the same thickness and length have much higher resonance frequencies and often higher quality factors, which makes them particularly attractive for gas sensing applications. For example, a microfabricated square-plate silicon resonator with a thickness of 25 μm and a side length of 2 mm, had an extensional resonance frequency of 2.18 MHz and a quality factor of 1.16×10^6 and 15000 in vacuum and air, respectively [118]. Even with such large thickness, this resonator had a surface mass sensitivity of approximately 125 pg/cm^2 at a pressure of few milliTorr, about an order of magnitude better than the areal mass sensitivity of a quartz crystal microbalance.

Scaling the thickness of plate resonators to the sub-micron dimensions should allow us to increase these sensitivities by many orders of magnitude. Together with our collaborators from LETI (Grenoble, France), we have modeled and started the fabrication of square plate resonators with a thickness of 360 nm and a variety of side lengths from 50 μm down to 5 μm. The expected resonance frequencies of the Lamé modes (Figure 5.7(b)) of these resonators range from 65 to 650 MHz, depending on the side length. Traditionally, such plate resonators have been detected using electro-

static (capacitive) actuation and detection. However, as discussed in Chapter 1, capacitive detection becomes much less effective at the nano scale. Therefore, we designed plate resonators that could use electrostatic actuation and piezoresistive downmixing detection. Figure 5.7(a) shows the geometry of such a plate resonator and the necessary connections to the drive, bias, and detection circuitry.

For the Lamé mode, the capacitive drive can be realized by applying a voltage across a small gap on two opposite sides of the plates. The resulting resonant motion can be detected using a serpentine piezoresistor, which can be aligned along either side of the plate (see Figure 5.7(a)). To estimate the piezoresistive signal, let us consider a plate resonator with thickness t, side length l, and capacitive gap g. The force generated on the opposite sides of the plate by the electrostatic drive will have an amplitude of

$$F_d \approx \frac{\varepsilon_0 l t V_d V_{dc}}{g^2}, \tag{5.4}$$

where ε_0 is the electric permittivity of vacuum, V_{dc} and V_d are the DC voltage and the amplitude of the ac drive voltage on the capacitive electrodes (see Figure 5.7(a)). On resonance, the drive forces will result in the longitudinal strain with an amplitude of approximately $\epsilon = QF_d/(Ylt)$, where Q is the quality factor of the resonance and Y is the Young's modulus of the plate material. The amplitude of the detected piezoresistive signal will be given by

$$V_s \approx \frac{1}{2}\epsilon V_b = \frac{\varepsilon_0 V_b V_d V_{dc}}{2Yg^2}, \tag{5.5}$$

where V_b is the amplitude of the ac bias signal. Assuming $V_{dc} = 10$ V, $V_d = V_b = 1$ V, $Y =$ 150 GPa, $g = 100$ nm, and a realistic quality factor of $Q = 1000$ in air, the expected piezoresistive signal is approximately 50 μV, which is comparable to the piezoresistive signals produced by out-of-plane cantilever and beam resonators. Assuming Johnson noise of $V_n = 5$ nV$/\sqrt{Hz}$, which corresponds to the piezoresistor's resistance of 5 kOhm, the expected relative frequency stability is $\sigma_f = V_n/(2QV_s) \approx 5 \cdot 10^{-8}$ Hz$^{-1/2}$. The expected areal mass sensitivity is then given by $2\rho t \sigma_f \approx$ 8 pg/cm^2, where $t = 360$ nm and $\rho = 2330$ kg/m^3 is the thickness and density of the silicon plate. For comparison, one adsorbed monolayer of water creates an areal mass load of approximately

40 ng/cm^2—more than three orders of magnitude larger. Achieving higher quality factors in air, using a higher dc voltage, V_{dc}, or thinner resonators can potentially improve this sensitivity even further. Devices with such record-setting areal mass sensitivities in air would open new possibilities in, for example, gas sensing applications.

Chapter 6

Nanomechanical resonator arrays for gas sensing applications

Individual nanoscale resonators have been used to establish record sensitivities in force [7], position [11], mass [4], and gas concentration [119]. The small size of nanoscale resonators clearly makes them particularly sensitive to external perturbations. However, it also limits the power these devices can use and the magnitude of signal they can produce. A simple way to increase the functionality of nanoscale devices is to combine such devices into arrays.

There are a number of ways arrays can leverage the sensitivity of individual devices. For example, different devices within the array can be used as sensors of different chemical compounds. Such arrays have been fabricated using both microscale cantilever resonators [120] and nanowire resonators [121]. Alternatively, one can engineer the mechanical coupling between individual resonators to produce a collective mode of oscillation that inherits the positive characteristics of individual resonators, such as high frequency and quality factor, but is able to handle more power [122]. Such collective modes can then be further optimized to produce the desired overall response, such as that of a bandpass filter [123].

In this chapter I describe a simple way of creating arrays of *nominally identical* devices by connecting them electrically in such a way that the signals of individual resonators add together.[1] As I show below, such arrays are simple to fabricate, can handle more power and produce more signal than individual resonators, but also place stringent requirements on the actuation methods

[1] The initial design, analysis, and measurements of electrically connected resonator arrays were done by J.S. Aldridge and E.B. Myers.

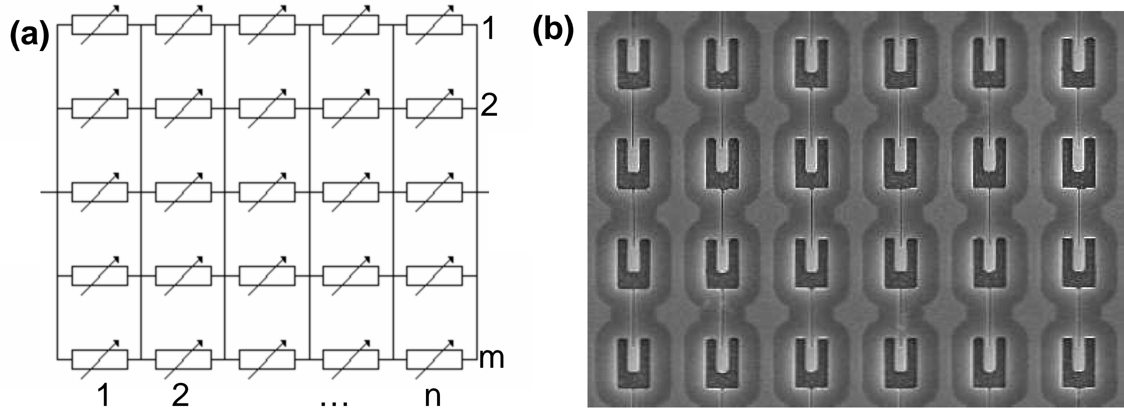

Figure 6.1: (a) Schematic of an electrically connected array of piezoresistors in the combined parallel-series configuration. (b) Fragment of an array of piezoresistive cantilevers fabricated at LETI (Grenoble, France). Each cantilever in the array is 2.8 μm long and 800 nm wide and consists of a 160-nm-thick structural silicon layer and 50-nm-thick AlSi metal layer.

and the fabrication tolerances.

6.1 Response of electrically connected arrays: Theory

Figure 6.1(a) shows a schematic of an electrically connected array of piezoresistors in the combined parallel-series configuration. Figure 6.1(b) shows one realization of such an array consisting of nominally identical piezoresistive cantilevers.

If we assume that at rest all piezoresistors have identical resistances R_0, the resistance of the entire array at rest is given by $R_{arr} = R_0 \times n/m$, where is m is the number of rows in the array, and n is the number of columns. If the resonators are excited into motion, the resistance of a piezoresistor in row i and column j will become $R_{ij} = R_0(1+\delta_{ij})$, where δ_{ij} is the relative change in its resistance due to the motion-related deformation. The resistance of the entire array in this case is given by

$$R_{arr} = \sum_{j=1}^{n} \frac{1}{\sum_{i=1}^{m} \frac{1}{R_0(1+\delta_{ij})}} \approx R_0 \frac{n}{m} \left(1 + \frac{1}{mn} \sum_{i=1,j=1}^{m,n} \delta_{ij} \right),$$

where the Taylor expansion is justified because the relative changes in the resistance of piezoresistors are generally small, $\delta_{ij} \ll 1$. When using piezoresistive downmixing, the signal is proportional to

the applied bias voltage V_b:

$$V_{arr} = \frac{1}{2}V_b\frac{\Delta R_{arr}}{R_{arr}} = \frac{1}{2}V_b\frac{1}{mn}\sum_{i=1,j=1}^{m,n}\delta_{ij}. \tag{6.1}$$

If all resonators respond in exactly identical ways, $\delta_{ij} = \delta_0$, the formula for the array signal reduces to that of an individual resonator:

$$V_{arr} = \frac{1}{2}V_b\frac{1}{mn}\sum_{i=1,j=1}^{m,n}\delta_0 = \frac{1}{2}V_b\delta_0. \tag{6.2}$$

The maximum drive that can be applied to an individual piezoresistive resonator is limited either by the nonlinearity of mechanical response or the maximum tolerable level of heating. In experiments, the maximum tolerable temperature increase due to heating was typically on the order of 100 K, corresponding to maximum dissipated power on the order of $P_{max} \sim 100$ μW for an individual resonator. If this maximum power is applied to each resonator in the array, the total dissipated power will naturally scale as the number of array elements, $N = nm$. In contrast, the bias signal, V_b, and the maximum signal that can be obtained from the array, V_{arr}, will scale as the number of columns, n.

It would seem then that an array consisting of just one row would be the most economical way to leverage the signal of individual resonators. However, having an array of just one row would mean that the array resistance scales linearly with the number of array elements, $R_{arr} = R_0 \times N$, and may reach excessively large values for arrays of thousands of resonators. In experiments, it is often desirable to keep the resistance of the total array close to some fixed value, usually 50 Ohm for high-frequency applications. In addition, a single-row array is very vulnerable to electrical defects since the breaking of the conducting path in just one piezoresistor would render the entire array inoperable. As a result, it is preferable to scale the number of rows proportionally to the number of columns, so that the arrays remain robust with respect to defective individual resonators and have approximately constant resistance. In this case, the piezoresistive signal scales proportionally to both n and m, and therefore proportionally to the square root of the total number of array

elements, $\sqrt{N}$. At the same time, the fundamental sources of noise in such measurement—Johnson noise and thermoelastic noise—do not depend on N at all. The signal-to-noise ratio then also scales as the square root of the number of elements, $\sqrt{N}$, and, of the total dissipated power, $\sqrt{Np_{max}}$. The situation when the signal-to-noise ratio increases proportionally to the square root of the total dissipated power is very common in electrical engineering.

Note, however, that the scaling of signal as $\sqrt{N}$ is the best-case scenario. In reality, different resonators *will not* respond to the drive in identical ways for a number of reasons. The first issue to consider is that the phase and amplitude of the drive may not be the same for all resonators. For example, in the case of piezoshaker drive (Section 2.1), the phases and amplitudes of the surface motion will vary due to the interference of ultrasound waves inside the bulk of the resonator chip. The length scale of such variations is on the order of the bulk acoustic wavelength corresponding to the resonator's frequency, $\sim 350\ \mu$m for a 25 MHz resonator on silicon substrate, which is smaller than the dimensions of the typical arrays we used in our experiments.

If we assume, for the sake of argument, that the drives for different resonators of the array have completely random phases φ_d but the same amplitude, then Eqn. (6.1) will take the form

$$V_{arr} = \frac{1}{2} V_b \frac{1}{mn} \sum_{i=1,j=1}^{m,n} \delta_{ij} e^{i\varphi_d}.$$

The expected magnitude of this signal is[2]

$$\langle |V_{arr}| \rangle = \frac{1}{2} V_b \frac{\sqrt{mn}}{mn} \delta_0 = \frac{1}{2} V_b \frac{1}{\sqrt{N}} \delta_0.$$

Since the bias signal V_b normally scales as $\sqrt{N}$, the use of arrays does not offer any advantages with respect to the use of an individual device in this case. It is therefore crucial to keep the drive phase the same for all the resonators in the array. Maintaining such phase coherence of the drive is difficult with piezoshaker drive but is much easier with integrated actuators, such as the thermoelastic actuators described in Section 2.3.

[2] The addition of signals with random phase is equivalent to a random walk in the complex plane, which implies that the magnitude of the sum $\sum_{i=1,j=1}^{m,n} \delta_{ij} e^{i\varphi_d}$ will scale as the square root of the total number of terms in the sum.

Even if the drives of all resonators in the array are perfectly in sync, the response of individual resonators may not be the same because they all have slightly different mechanical properties, in particular different resonance frequencies. The finite resolution of e-beam and optical lithography introduces slight variations in the dimensions of the fabricated resonators and hence their frequencies. A simple way to judge whether this dispersion in resonance frequency is significant is to compare it to the natural width of the resonance under typical operating conditions. For example, nanoscale resonators shown in Figure 6.1 have a typical quality factor on the order of 100 at atmospheric pressure in air, corresponding to a resonance width that is 1% of the resonance frequency. Therefore, if the dispersion of resonance frequency is much smaller than 1%, the individual resonance curves will strongly overlap and the Lorentzian-response terms δ_{ij} appearing in Eqn. (6.1) may be treated as the same, leading to Eqn. (6.2). Conversely, if the dispersion of the frequencies is much larger than 1%, the sum of the individual Lorentzian response curves will be much broader than an individual resonance, and the peak array signal will be much reduced with respect to the maximum possible signal given by Eqn. (6.2).

In order to quantify this qualitative argument, we need to consider the problem of adding up many Lorentzian resonance curves with randomly distributed resonance frequencies. The normal or Gaussian probability distribution is a common choice in such simulations; however, I have found that in reality the distribution of resonance frequencies has long and "fat" tails, i. e., the probability of finding resonance frequencies far off the mean is much larger than would be expected in a Gaussian distribution.[3] I have therefore chosen to use the Cauchy distribution, which has the probability density distribution similar to the Lorentzian:

$$p(\omega_R) = \frac{Q_{distr}/(2\pi\omega_0)}{1 + \left(\frac{\omega_R - \omega_0}{2\omega_0/Q_{distr}}\right)^2}, \tag{6.3}$$

where ω_0 is the center frequency of the distribution and Q_{distr} characterizes the width of the distribution, similarly to the way that a quality factor characterizes the width of a Lorentzian curve. The Cauchy distribution describes more accurately the long tails of the frequency distribution that

[3] The large number of outliers is illustrated by the data shown Figs. 6.5–6.7 below.

we observe in practice and has the added advantage that the expected form of the array response can be calculated analytically, as shown below.

The response of a forced, damped harmonic oscillator is given by

$$s(\omega) = A\frac{\omega_R^2/Q}{\omega_R^2 - \omega_D^2 + i\frac{\omega_R\omega_D}{Q}},$$

where A is the amplitude of the resonance signal, ω_R is its resonance frequency, Q is its quality factor, and ω_D is the frequency of the drive. If the quality factor of an individual resonator is large, $Q \gg 1$, the response near the resonance can be approximated by a complex Lorentzian

$$s(\omega) \approx A\frac{\omega_R/2Q}{\omega_R - \omega_D + i\frac{\omega_R}{2Q}}.$$

The expected signal from one array cantilever with a randomly distributed resonance frequency is then a convolution of the complex Lorentzian response with the Cauchy distribution:

$$\langle s(\omega)\rangle \approx \int_{-\infty}^{\infty} \frac{A\omega_R/2Q}{\omega_R - \omega_D + i\frac{\omega_R}{2Q}} \times \frac{Q_{distr}/(2\pi\omega_0)}{1+\left(\frac{\omega-\omega_0}{2\omega_0/Q_{distr}}\right)^2} d\omega_R = \frac{A\omega_0/2Q}{\omega_0 - \omega_D + i\frac{\omega_0}{2}(1/Q + 1/Q_{distr})},$$

which is simply the complex Lorentzian response with a new effective quality factor $Q_{eff} = 1/(Q^{-1} + Q_{distr}^{-1})$ and a new effective amplitude $A_{eff} = Q_{eff}/Q$. The expected signal of the entire array will have the same form, since it is essentially the sum of the expected signals of individual cantilevers and we assume all cantilevers in the array to be described by the same Cauchy distribution. In addition, for a large array, the typical response generally will not deviate far from the expected response as the random variations introduced by individual resonances will largely average out. Therefore, the frequency dispersion has the same result as an additional source of damping, corresponding to a quality factor Q_{distr}, reducing the effective quality factor of the array from Q to $Q_{eff} = 1/(Q^{-1} + Q_{distr}^{-1})$.

To illustrate this effect of the resonance frequency dispersion on the shape of the array response, I have performed numerical simulations for an array consisting of 2800 elements. The results are

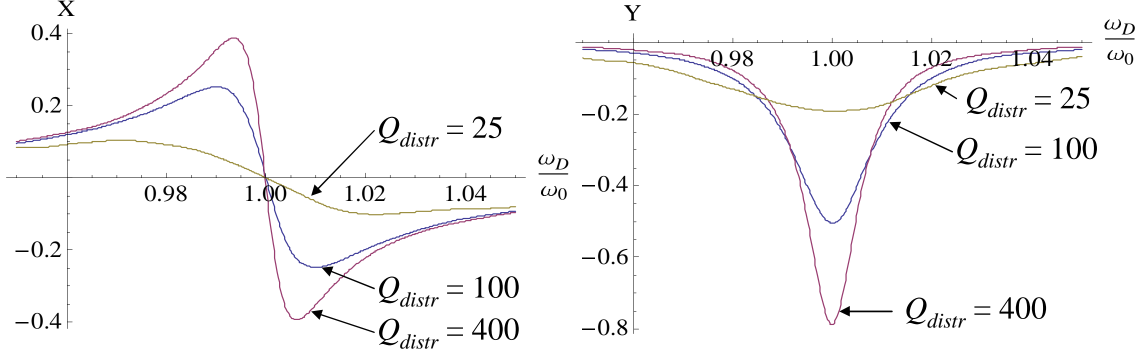

Figure 6.2: X and Y quadratures of the simulated response of an array of 2800 cantilevers with $Q = 100$ and Q_{distr} of 400, 100, and 25. The effective quality factors Q_{eff} in these cases are $1/(400^{-1} + 100^{-1}) \approx 80$, $1/(100^{-1} + 100^{-1}) \approx 50$, and $1/(25^{-1} + 100^{-1}) \approx 20$, respectively.

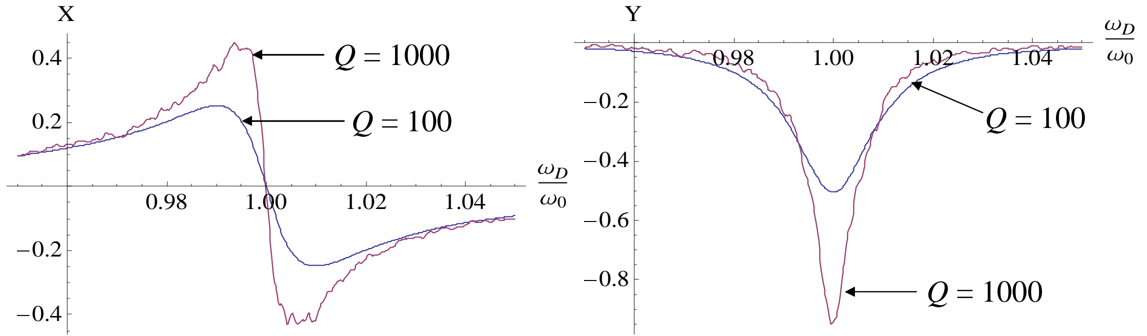

Figure 6.3: X and Y quadratures of the simulated response of an array of 2800 cantilevers with $Q_{distr} = 100$ and $Q = 100$ and 1000. The effective quality factors Q_{eff} in these cases are $1/(100^{-1} + 1000^{-1}) \approx 90$ and $1/(100^{-1} + 100^{-1}) \approx 50$, respectively.

shown in Figure 6.2. In the simulations, all resonators were assumed to have a quality factor of 100, and the width of the Cauchy distribution was varied, starting from a distribution width much smaller than the natural width of the resonance, $Q_{distr} \gg Q$, and ending with a distribution width much larger than the natural width of the resonance, $Q_{distr} \ll Q$. As expected, increasing the width of the frequency distribution broadens the resonance peak of the entire array and reduces its amplitude.

In Figure 6.2, the simulated response curves do not deviate significantly from the perfect Lorentzian curves due to the large number of the elements in the array and their relatively low quality factors. However, the fact that the overall response curves of the array consist of many narrow lines corresponding to individual resonators becomes evident if the quality factors Q of individual resonances

are high enough, as shown in Figure 6.3. These two curves simulate the response of the actual array shown in Figure 6.1(b) in air and vacuum. The frequency distribution width of the typical arrays I have worked with were on the order of 1%, corresponding to $Q_{distr} \approx 100$, and the quality factors of individual resonances were on the order of 100 and 1000 in air and vacuum, respectively. As a result, the experimental curves in air were much smoother than those in vacuum, and the effective quality factor of the array response was approximately 100 in vacuum and 50 in air, as illustrated by Figure 6.3.

The differences between different resonators in the array are, of course, not limited to the variations in the drive phase and resonance frequencies. The quality factors and and the amplitudes of response of individual resonators will also vary. However, we have found in our experiments that these variations are relatively insignificant and have a negligible effect on the overall response of the arrays.

6.2 Response of electrically connected arrays: Experiment

I have measured a number of electrically connected arrays fabricated by our collaborators at LETI (Grenoble, France) (see Figure 6.1(b)). The cantilevers forming the arrays were bilayer structures consisting of a 160-nm-thick structural silicon layer and a 50-nm-thick $Al_{0.96}Si_{0.04}$ metal layer, similar to the one shown in Figure 1.2(c). The lengths of the arrays varied between 1.6 and 5 μm depending on the particular array design, and the width of the cantilevers was either 800 nm or 1.2 μm. The majority of the arrays I have measured consisted of 20 rows and 140 columns for a total of 2800 array elements. The pitch between the array elements was either 6.5 μm or 10 μm depending on the design.

I measured the arrays using the two-port measurement scheme described in detail in the Appendix B. The main idea is to use a single metal loop of a resonator for both thermoelastic actuation and piezoresistive detection. This measurement scheme works in the same way for arrays as for individual cantilevers, the only difference being the need to supply more RF power in the case of arrays. The setup for measuring arrays is shown schematically in Figure 6.4(a). The power amplifier (Am-

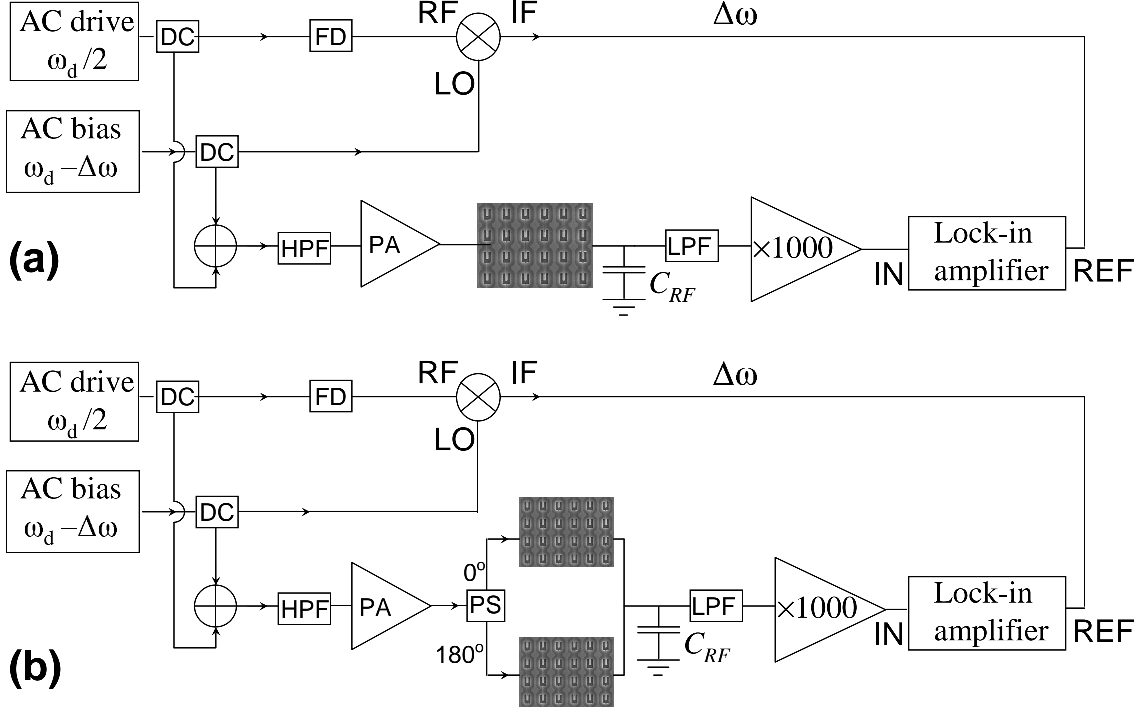

Figure 6.4: (a) Schematic of two-port measurements of arrays using thermoelastic actuation and piezoresistive detection. DC is the directional coupler, FD is the frequency doubler, HPF is the high-pass filter, LPF is the low-pass filter, and PA is the power amplifier. (b) Schematic of bridge measurement of two arrays. PS is the 180-degree power splitter.

plifier Research model 25A250A) was rated at 25 W maximum output power, but in our experiments the maximum power supplied to the arrays typically did not exceed 1 Watt per array.

Figures 6.5 and 6.6 show typical results of a two-port measurement of an array. Both measurements are of the "double" type, as described in the Appendix B. The background in these measurements was large, 10 to 100 times larger than the amplitude of the array resonance peak. Consistent with the simulations of the previous section, the vacuum response curves feature many sharp features corresponding to resonances of individual high-Q cantilevers. The air curves are generally smoother and the sharp features in them, where present, are due to noise spikes.

In order to obtain more information about the dispersion of frequencies in the arrays, we have also done measurements using thermoelastic actuation and optical detection.[4] The optical detection setup was a simple reflection interferometer with a spot size of approximately 10 μm. The results are

[4]I thank Rassul Karabalin for his help in using the optical detection setup.

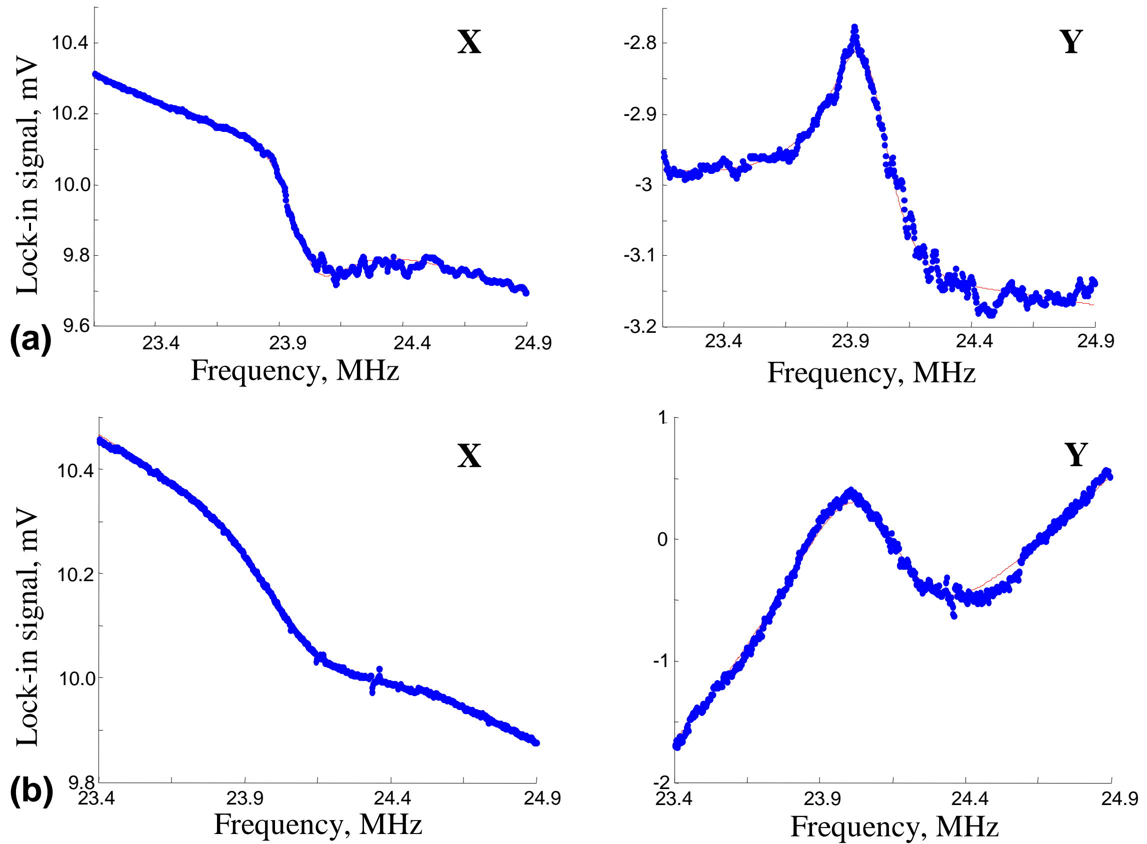

Figure 6.5: Resonant response of the CK-A array in vacuum (a) and air (b). Both quadratures of the lock-in response, X and Y, are shown. The blue dots are the experimental data, the red lines are best complex Lorentzian fits. In vacuum, the fitted frequency is 24.0 MHz and the effective quality factor is 80. In air, the fitted frequency is 24.1 MHz and the effective quality factor is 40.

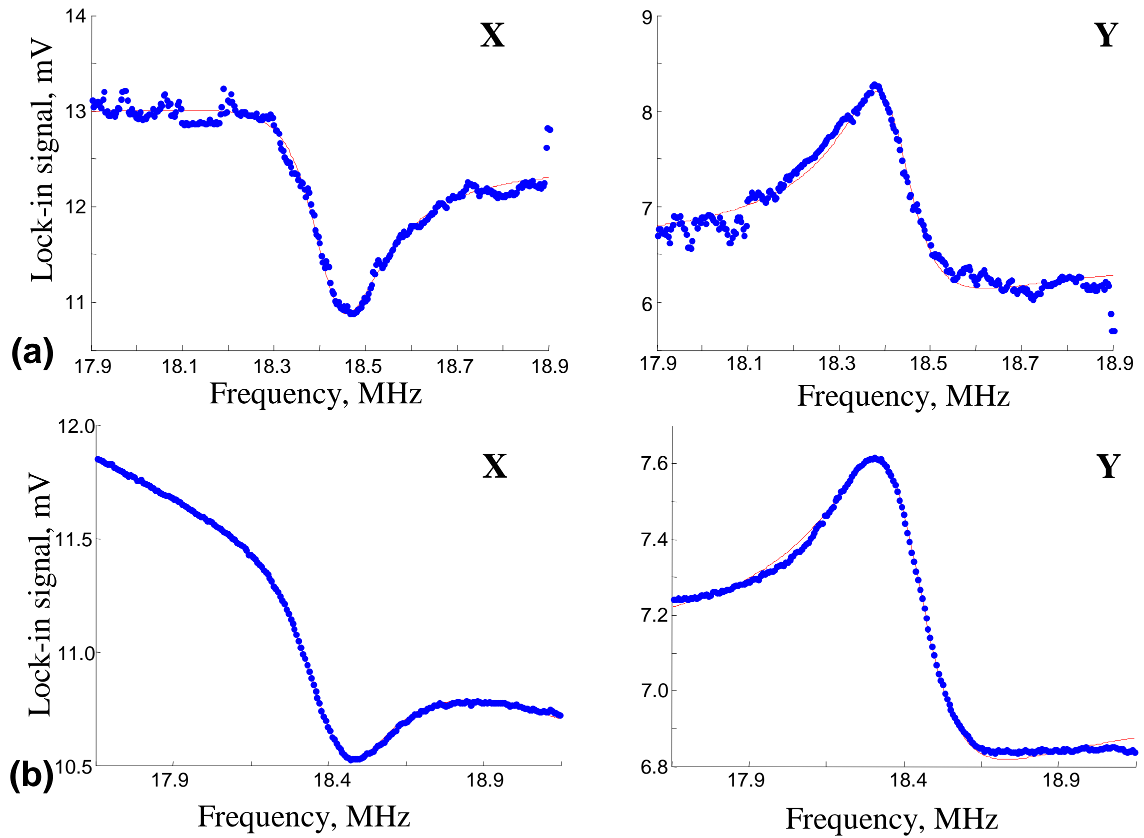

Figure 6.6: Resonant response of the A3A8 array in vacuum (a) and air (b). Both quadratures of the lock-in response, X and Y, are shown. The blue dots are the experimental data, the red lines are best complex Lorentzian fits. In vacuum, the fitted frequency is 18.4 MHz and the effective quality factor is 100. In air, the fitted frequency is 18.4 MHz and the effective quality factor is 50.

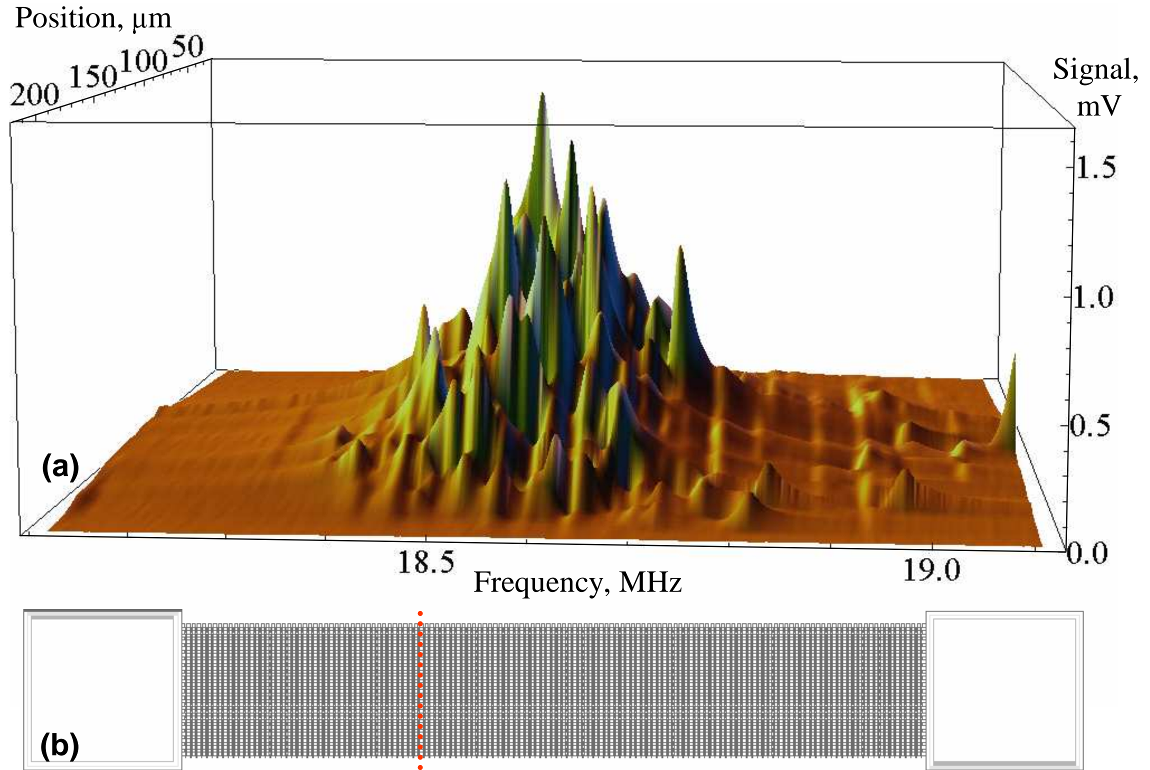

Figure 6.7: (a) Optically detected spectrum of cantilevers in array A3A9 for different positions of the laser spot. (b) Top-view schematic of the 140×20 array of cantilevers (device no. A3A9). Individual cantilevers are not visible in this image. The dotted red line schematically shows the positions of the laser spot used to acquire the spectra.

shown in Figure 6.7(a), where I plot the interferometer signal of array versus excitation frequency and the position of the beam spot. The position of the beam spot was swept across the width of the array A3A9 with a step of 5 μm (see Figure 6.7(b)).

The small size of the optical spot allows us to detect a small number of cantilevers within the beam spot instead of the entire array of 2800 cantilevers. As a result it is often possible to resolve the resonance peaks of individual cantilevers in these spectra. The majority of individual resonances are situated near the central frequency of 18.6 MHz, and these resonances form the main peak of the array response. However, there are also a large number of “outliers”, especially at frequencies above the central peak. Some of these resonances are sufficiently well resolved to be fitted individually. The quality factor of such individual resonances in vacuum was approximately 1000.

We did not have individual devices with geometries identical to those of array cantilevers, but

Name	Length	Width	f_{av}	$Q_{eff}(vac)$	$Q_{eff}(air)$
A3A6	5.0 μm	1.2 μm	5.88 MHz	130	12
A3A5	2.8 μm	0.8 μm	16.5 MHz	120	50
A3A7	2.8 μm	0.8 μm	18.4 MHz	100	50
A3A8	2.8 μm	0.8 μm	18.4 MHz	100	50
CK-A	2.1 μm	0.8 μm	24.1 MHz	80	40
CK-2-A	2.1 μm	1.2 μm	24.8 MHz	100	60
A3A4	1.6 μm	0.8 μm	$\approx$65 MHz	n/a	n/a

Table 6.1: Fitted parameters of the resonance peaks of arrays of cantilevers of different dimensions. All arrays consisted of 20 rows and 140 columns of individual cantilevers. The cantilevers consisted of 160-nm-thick Si structural layer and a 50-nm-thick AlSi metal layer. The difference between arrays A3A5, A3A7, and A3A8 was in the row and column pitches of the arrays.

we had many cantilevers with similar geometries. The quality factors of these cantilevers in vacuum were also on the order of 1000. This leads to the conclusion that the effective quality factor of the entire array observed in vacuum is determined by $Q_{distr} \approx 100$. In air, the quality factor of individual devices was on the order of 100, resulting in the effective quality factor of the array of $1/(1/100 + 1/100) = 50$, in accordance with the fitted quality factors of Figs. 6.5 and 6.6.

Table 6.2 summarizes the fitted parameters for various measured arrays. The effective quality factor in vacuum is on the order of 100, which means that the characteristic frequency spread is approximately 1%. In general, the frequency spread increases as the dimensions decrease because the same lithographic imperfections have a proportionately larger effect on smaller structures. Conversely, the quality factor of *individual* cantilevers in air generally decreases as their length increases because longer cantilevers have lower resonance frequencies, which reduces their quality factors in air [111, 112]. The effective quality factor of the array in air, therefore, does not have a simple dependence on the dimensions. The results of Table 6.2 and our prior measurements of similar cantilevers suggest that there is a "sweet spot" of dimensions that optimize the effective quality factor of the entire array. For out-of-plane fundamental resonances considered here, the cantilever length corresponding to this sweet spot is between 2 and 3 μm. Cantilevers much longer than 3 μm tend to have very low quality factors in air, whereas arrays of cantilevers much shorter than 2 and 3 μm tend to have too much frequency dispersion. The effective quality factor of 50 to 60 is therefore close to the practical maximum for the out-of-plane cantilevers of this thickness.

In can be seen from the Figs. 6.5 and 6.6 that the background is quite large in the array measurements. The background amplitude was larger than the resonance response amplitude by a factor of between 15 and 100 for different arrays. This relatively large background is a general feature of two-port measurements and is due to the temperature dependence of resistivity (See Appendix B for details), but in the case of arrays the situation is aggravated by the fact that the effective quality factor of the array is smaller than that of individual cantilevers, which reduces the amplitude of the resonance response. This large background creates a number of problems in measuring the response of arrays. First, it places additional requirements on the dynamic range of the detection equipment. For example, if the lock-in amplifier has a 4-digit analog-to-digital converter, the minimum measurable relative change is 10^{-4} of the full-scale sensitivity. If the background is 50 times larger than the resonance signal, the minimum measurable relative change of the *signal* will be $10^{-4} \times 50 = 0.5\%$, significantly worse than lock-in amplifier's intrinsic limitations. Second, from our experience, large background can increase noise in the system because background is never perfectly stable. The background in these measurements is caused by parasitic conductances and nonlinearities in circuit components in general and the chip substrate in particular. The parasitic conductances tend to fluctuate in time, occasionally producing the noise spikes seen, for example, in Figure 6.5(b).

In view of these problems it is generally advantageous to null the background signal, for example, by performing a balanced detection of two arrays simultaneously as shown in Figure 6.4(b). The two arrays in the balanced detection typically have similar but not identical dimensions, so that the average resonance frequencies of the two arrays are well resolved. The similarity of dimensions ensures that the background signals due to the two arrays cancel each other out, but the resonance peaks do not cancel out because they occur at different frequencies.

Figure 6.8 shows the result of a balanced measurement of two arrays CK-2-A and CK-2-B in vacuum. The response now features two resonance peaks, the lower corresponding to the array CK-2-A and the upper to CK-2-B. The background is now indeed much smaller and is of the same order of magnitude as the resonant signal. Because this measurement is done in vacuum, both quadratures have a “fine structure” of rapid variations attributed to the resonances of individual

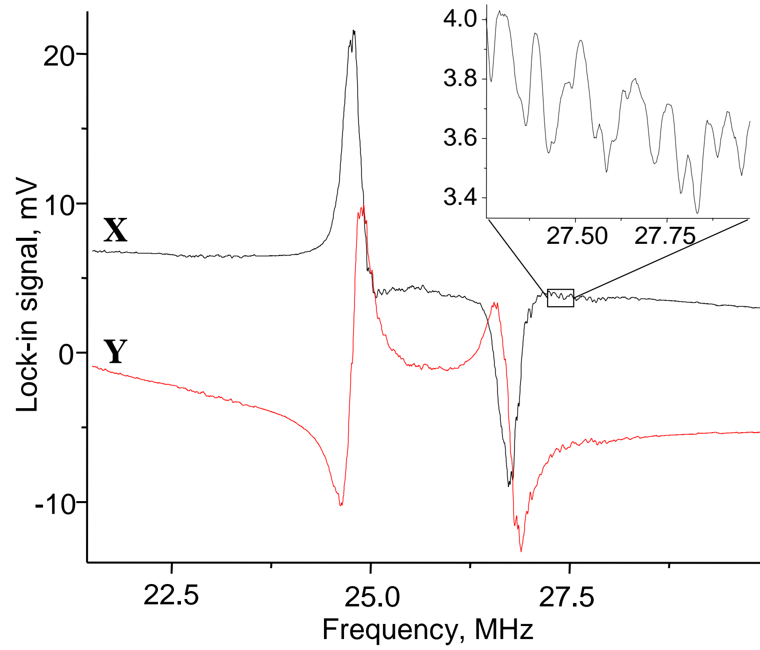

Figure 6.8: Balanced detection of the arrays CK-2-A and CK-2-B in vacuum. Both quadratures of the lock-in response, X and Y, are shown. The inset zooms in on a fragment of the X quadrature curve to show the rapid variations attributed to resonances of individual cantilevers. The noise level in these measurements was approximately 1.7 μV_{rms}, which is more than an order of magnitude smaller than the amplitude of the rapid variations.

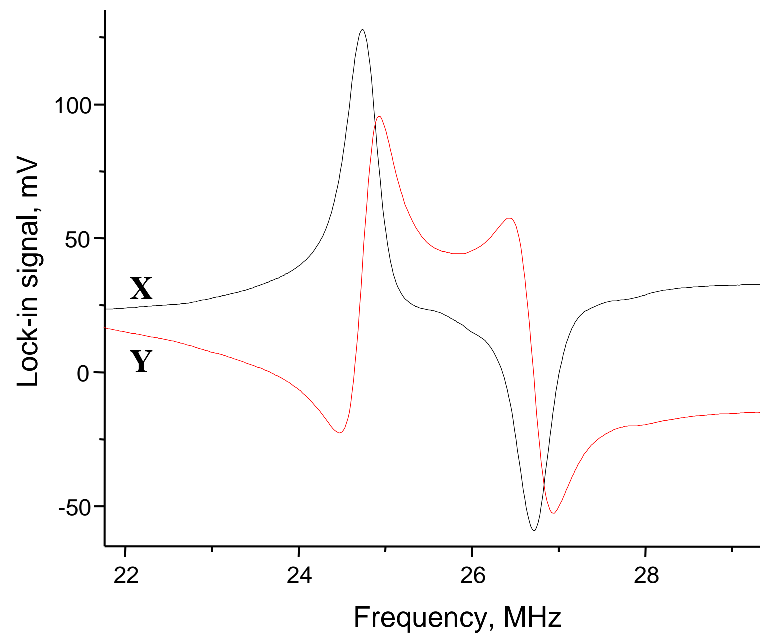

Figure 6.9: Balanced detection of the arrays CK-2-A and CK-2-B in air. Both quadratures of the lock-in response, X and Y, are shown. Much larger drive voltages are used here than in Figure 6.8.

cantilevers of the array. These variations are reproducible and are much larger than the amplitude of measurement noise. The amplitude of these variations also agrees with the expected amplitude of the individual resonances in this measurement scheme:

$$A_{array}\frac{Q}{NQ_{eff}} \approx 20\text{ mV}\frac{1000}{2800 \times 100} \approx 70\,\mu\text{V},$$

where A_{array} is the amplitude of the array response.

In air, these variations are smoothed out and the response looks like Figure 6.9. The fits of the two array resonance peak yield quality factors of approximately 60. The signal-to-noise ratio (SNR) is approximately 7500 with 1 millisecond time constant, which corresponds to approximately 100 Hz bandwidth. The calculated frequency noise for this setup is $\sigma = (\text{SNR} \times 2Q_{eff})^{-1} = (7500 \times 2 \times 60)^{-1} \approx 1.1$ ppm with 100 Hz bandwidth or 0.11 ppm with 1 Hz bandwidth.

6.3 Preliminary gas sensing data[5]

The primary goal of developing cantilever arrays is to create sensors with higher sensitivity than individual devices. In order to realize this goal, we need to integrate the sensor arrays with the rest of the gas sensing system. One way of doing it involves the fabrication of a microfluidic flow cell that can be mounted on top of the nanomechanical sensor and is directly connected to an external gas delivery system, such as a commercial gas chromatography (GC) system [32]. This way, the nanoscale resonator is only exposed to the analytes and carrier gas and remains isolated from the air of the environment. In addition, the volume of the cell and, therefore, the diffusion time, which often limits the speed of gas chromatography analysis, can be minimized with proper design [119].

In our preliminary experiments with arrays, we did not use a microfluidic cell. Instead, we operated the arrays in ambient air atmosphere and used a micropositioner to move the end of the 90-cm-long column of the gas-chromatography system immediately above the sensor array (see Figure 6.10). Prior to this, the array was coated with the DKAP polymer, developed at Sandia

[5]Measurements described in this section were performed in collaboration with E.B. Myers.

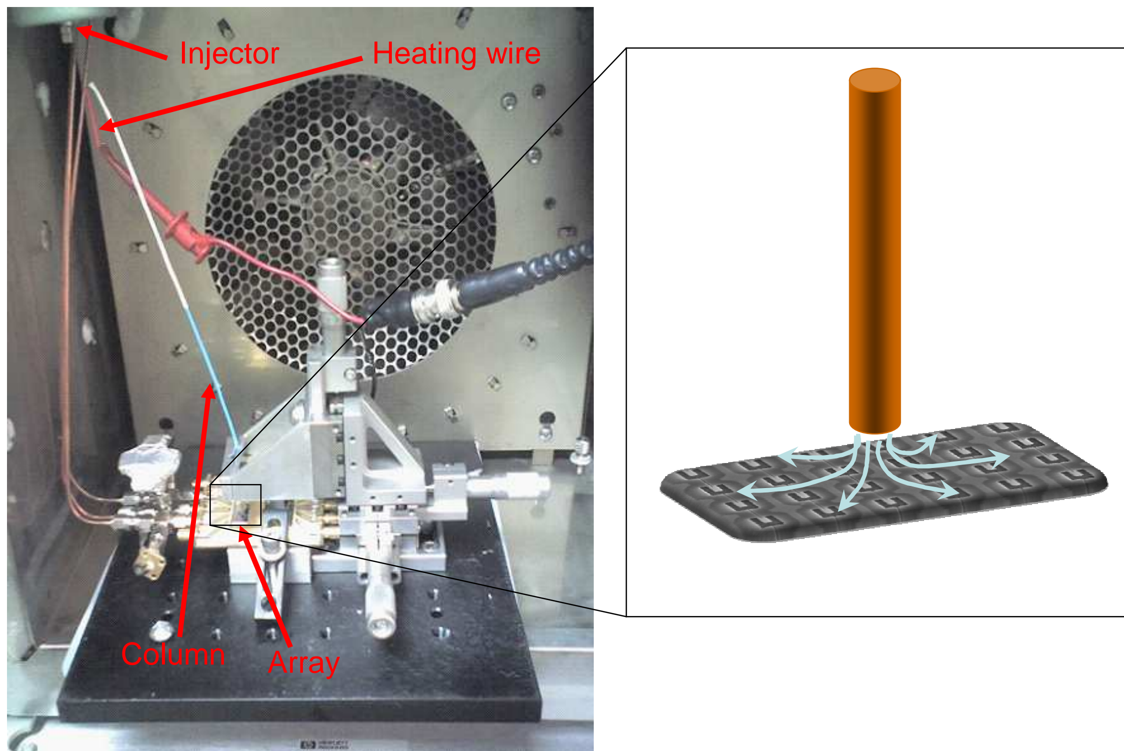

Figure 6.10: Integration of the array sensors into a commercial Hewlett Packard 5890 gas chromatography system. The photograph shows the inner chamber of the GC system with the injector, column, and column heating wires as well as the printed circuit board with the sensor arrays and a micropositioner. The inset shows schematically how the lower end of the column is positioned above the array and how the effluent flows from the column.

National Laboratory for detection of phosphonate gas molecules—precursors and simulants of nerve gas agents. A droplet of DKAP solution was put on the array chip surface and left to dry in air, leaving a thin film of polymer on the array cantilevers [32].

Functionalization of the array did not have a measurable effect on the frequency or the effective quality factor of the array response.[6] However, the quality factor was noticeably affected by the flow of the hydrogen carrier gas through the column. When the GC system was in operation, the hydrogen carrier gas was forced out of the bottom end of the column at the rate of 1–2 sccm (standard cubic centimeters per minute) and largely displaced the air in the immediate vicinity of the array (see inset of Figure 6.10). Because the viscosity of hydrogen is much lower than that of

[6]In previous experiments [32], the frequency of resonators typically decreased by less than 0.1% after functionalization due to the mass loading by the polymer. A change of 0.1% in frequency is easily measurable for an individual resonator with a quality factor of ∼1000 in vacuum, but much less noticeable for an array with an effective quality factor of only 100 in vacuum and 50 in air.

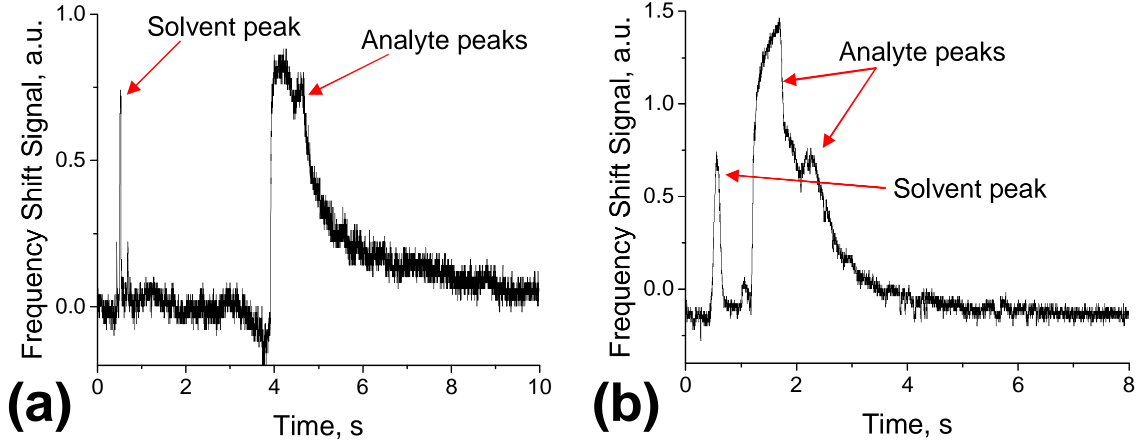

Figure 6.11: Gas chromatogram obtained with an array sensor in the bridge configuration without additional heating of the column (a) and with 10 Watt resistive heating of the column (b). In the case of resistive heating, the expected temperature increase of the column is a few tens of degrees.

air, this increased the quality factor of individual resonances, Q, and therefore the effective quality factor of the entire array in accordance with the formula $Q_{eff} = 1/(Q^{-1} + Q_{distr}^{-1})$. The increase in quality factor was typically 20%, from $Q_{eff} \sim 50$ to $Q_{eff} \sim 60$.

In order to test the gas sensing functionality of the arrays, we have performed open-loop measurements of frequency shift of the array CK-2-A after injecting a solution of diisopropyl methylphosphonate (DIMP), a nerve gas simulant, in CS_2 solvent. The open-loop frequency measurements of frequency shift are done by monitoring the dispersive quadrature of the Lorentzian response (see, for example, curve Y in Figure 6.9). If the drive and bias frequencies remain constant and the central peak frequency of the arrays changes by $\Delta\omega_R$, the dispersive components of the resonance signal will change by

$$\Delta Y \approx \frac{dY}{d\omega_R}\Delta\omega_R \approx \frac{2Q_{eff}A_{arr}}{\omega_R}\Delta\omega_R,$$

where A_{arr} is the amplitude of the resonance peak. Therefore, there is a direct correspondence between changes in the resonance frequency and the measured changes in the dispersive quadrature of the signal.

Figure 6.11 shows the resulting chromatograms. The narrow solvent peak happens immediately after injection of analyte into the column. The analyte peaks appear a few seconds later because of

their affinity to the special coating on the inside surface of the column. There are two discernible analyte peaks in both chromatograms. The later, smaller peak is most likely coming from partial contamination of the injected solution with diethyl methylphosphonate (DEMP)—another nerve gas simulant we used in these experiments. The timing and the widths of the peaks depended on the temperature of the column. The two panels of Figure 6.11 show the difference between the chromatograms obtained with and without additional heating of the column. In the heated case, the peaks appear sooner than in the non-heated case, consistent with the measurements done with individual cantilevers [32].

Taking into account amplification, a change of one volt in the dispersive component corresponds to the resonance peak shifting by approximately 8 kHz, or 8 kHz/24.5 MHz = 330 ppm. The best frequency sensitivity we could obtain in experiment was approximately 6 ppm with 1 ms time constant of the lock-in (corresponding to approximately 150 Hz bandwidth). This sensitivity is approximately an order of magnitude worse than the value calculated in the previous section, but still slightly better than the results obtained with individual cantilevers [32]. The sensitivity is worse because the noise measured inside the GC system was approximately an order of magnitude higher than in the experiments described in the previous section. At this point we have identified and eliminated some of the sources of excess noise, but more work needs to be done to achieve better sensitivity.

Regardless of the source of the noise, one way to improve the sensitivity of frequency measurements in he future is to use arrays with higher effective quality factors, Q_{eff}. In order to obtain better quality factors, we need to improve both the width frequency distribution, described by Q_{distr}, and the quality factor of individual resonators in air, Q. Both goals can be achieved by using in-plane modes or extensional modes, such as those described in Section 5.3. For cantilevers (and beams without tension), the resonance frequencies of out-of-plane, in-plane, and extensional resonances generally obey the following scaling laws:

$$f_{out} \sim \frac{t}{l^2}, \quad f_{in} \sim \frac{w}{l^2}, \quad f_{ext} \sim \frac{1}{l}. \tag{6.4}$$

where l, w, and t are the cantilever's length, width, and thickness, respectively.

For a given resonance geometry, the in-plane and extensional resonance frequencies are larger than the out-of-plane resonance frequency by a factor of w/t and l/t, respectively. This means that in-plane or extensional resonators can be made much larger than out-of-plane ones and still achieve the same high resonance frequency as out-of-plane resonators. For larger structures, the effect of fabrication imperfections should be proportionally smaller and we can expect the width of frequency distribution to be smaller as well.

As discussed in Chapter 5, in-plane resonators can also have dramatically higher quality factors in air because of reduced viscous damping. It is realistic to expect effective quality factors on the order of 500 from arrays of in-plane or extensional resonators. Such arrays should achieve frequency resolution approximately one order of magnitude better than the arrays described in this chapter, which would result in record concentration sensitivity in NEMS-based gas chromatography measurements.

Concluding remarks

In this thesis, I have described new ways to operate nanomechanical resonators and to use them in sensor applications. Of all the available detection techniques, we focused on piezoresistive detection and, in particular, the piezoresistive downmixing technique. Using downmixing allowed us to avoid the problem of parasitic capacitances and therefore to use high-impedance semiconductor piezoresistors at high frequencies. Downmixing also dramatically reduced the effect of parasitic electric feedthrough in piezoresistive measurements, allowing us to measure resonance response with low levels of interfering background.

We have also considered a number of actuation techniques for nanomechanical resonators. The traditional piezoshaker actuation was shown to be highly non-uniform in both space and frequency, especially at high frequencies and low temperatures. We therefore turned our attention to other actuation techniques, out of which thermoelastic actuation turned out be very effective for nanoscale resonators. Combined with piezoresistive detection, thermoelastic actuation enabled us to detect multiple modes of nanoscale doubly clamped beams and other types of resonators.

In addition to actuation and detection techniques, we have studied methods of tuning the resonance frequencies of nanomechanical resonators. We showed that the electrostatic tuning mechanism is effective for the fundamental modes of nanoscale beam resonators with resonance frequencies in the single-digit-megahertz range. However, electrostatic tuning becomes less effective as the frequency increases and is also very difficult for higher flexural modes of beam resonators. In contrast, the adsorptive tuning mechanism can be easily used to tune the resonances of arbitrary modes and frequencies as long as the temperature of the resonator is low enough. At liquid helium temperatures, we have tuned the resonance frequencies multiple modes of beam resonators by more than

15% using the additional mass of adsorbed inert gas molecules.

These new detection, actuation, and tuning techniques allowed us to study systems in which the coupling between the mechanical motion of a nanoscale resonator and the dynamics of nuclear spins could potentially be strong enough to be detectable. We have considered a number of such systems, including the traditional transverse MRFM setup, a system using a thin film containing nuclear spins with large quadrupole moments, and a system using a thin ferromagnetic film with magnetically active nuclei. Of these, the system using a thin ferromagnetic film was expected to produce the largest signal. However, our efforts to detect signatures of spin–resonator interaction in this system did not yield any conclusive results.

Apart from spin sensing, we could apply the same methods of actuation and detection to other problems related to nanomechanical sensors. In particular, the measurement of multiple modes of nanomechanical oscillators allowed us to study the frequency, temperature, and geometry dependence of quality factors of nanomechanical resonators in more detail than ever before. Our data indicated that, in vacuum, the quality factors of low-numbered flexural modes are limited by the same surface-related, clamping-sensitive loss mechanism at both room temperature and cryogenic temperatures. Our data also suggested that the quality factors of high-numbered flexural modes are limited by a temperature-independent loss mechanism—possibly, clamping losses. In air, our data showed that the quality factor generally increases with frequency and mode number. For some in-plane modes of the nanomechanical resonators, the viscous-damping-limited quality factors were on the order of 1000. These high quality factors of in-plane modes have motivated us to study a number of alternative resonator geometries, which also feature high qualify factors in air.

Finally, we have applied the same methods of thermoelastic actuation and piezoresistive detection to arrays of electrically connected cantilevers. We have shown that the maximum signal that can be obtained from arrays can scale as the square root of the number of array elements. However, in order to benefit from this scaling, the resonators of the array must be highly uniform in frequency. We have demonstrated that arrays of nanoscale cantilevers can be successfully functionalized and used in gas sensing experiments.

The experiments described in this thesis can be continued in a number of promising directions in the future. For example, detection of multiple modes of nanomechanical resonators can be used to improve the resolution of NEMS-based mass spectroscopy of biomolecules, currently pursued by Akshay Naik and Mehmet Selim Hanay in our group. In these experiments, the frequency shift produced by one macromolecule depends on two variables: the mass of the molecule and the exact position where it attaches itself to the resonator. Measuring the frequency shift of just the fundamental mode does not allow one to solve for both of the unknowns. However, simultaneous measurement of the frequency shift of two or more flexural modes of the beam should allow one to solve for both the position of the attached molecule and its mass—a necessary step towards building a real NEMS mass spectroscopy system.

Development of high quality factor resonators using the Lamé modes of plate resonators holds a promise of having unprecedented areal mass sensitivity in vacuum and air. The experimental work is currently underway in collaboration with our colleagues from LETI. High-Q plate resonators could also be used for biological molecule detection in liquid environments, where the lack of high quality factor devices has prevented us from conducting NEMS experiments so far. In order to realize the best geometries for sensing, it is essential to develop a theory for the loss mechanisms in air and liquid for plate resonators and other types of in-plane resonators.

Finally, arrays of center-supported beam resonators that employ in-plane flexural or extensional modes can be used to achieve record concentration sensitivity in gas sensing applications. Center-supported beam resonators benefit from high quality factors and the minimal dependence of their frequencies on the etching-related variation of the support geometry. As a result, arrays of such resonators can feature high effective quality factors and take full advantage of increased sensitivity offered by arrays. Development of ultra-sensitive resonator arrays will also be the first step toward future large-scale-integrated (LSI) nanomechanical systems, able to deliver dramatically better sensor performance for addressing real-world problems.

Appendix A

Phase relationships in piezoresistive downmixing

When using piezoresistive downmixing (Section 1.2), the bias frequency can be lower than the drive frequency, $\Delta\omega > 0$, or higher, $\Delta\omega < 0$. Both approaches can be used to detect the resonance at the downmixed frequency, $|\Delta\omega|$, but the phase behavior of the resonance signal depends of the sign of $\Delta\omega$ in a subtle way.

Normally, the response of a forced damped harmonic oscillator is described by the complex Lorentzian

$$s = A \frac{\omega_R^2/Q}{\omega_R^2 - \omega_D^2 + i\frac{\omega_R \omega_D}{Q}}, \tag{A.1}$$

where ω_R is the resonance frequency, ω_D is the drive frequency, A is the amplitude of the resonance signal, and Q is its quality factor. If the quality factor is large, $Q \gg 1$, the real and imaginary components of this signal, X and Y, plotted parametrically as a function of the drive frequency, will form a circle (see Figure A.1). As the frequency increases, the point corresponding to the amplitude components X and Y will move clockwise along the circle, as indicated by arrows in Figure A.1. The amplitude of the complex signal is largest at the resonance, $\omega_D = \omega_R$, when $X = 0$ and $Y = -A$.

In a typical experimental setup, there is some parasitic background in the system, so that the circle begins and ends not at the origin but at some arbitrary point corresponding to the complex amplitude of the parasitic background. In addition, various phase shifts that exist in the system due to cables and other RF components may rotate the circle by an arbitrary angle in the XY plane.

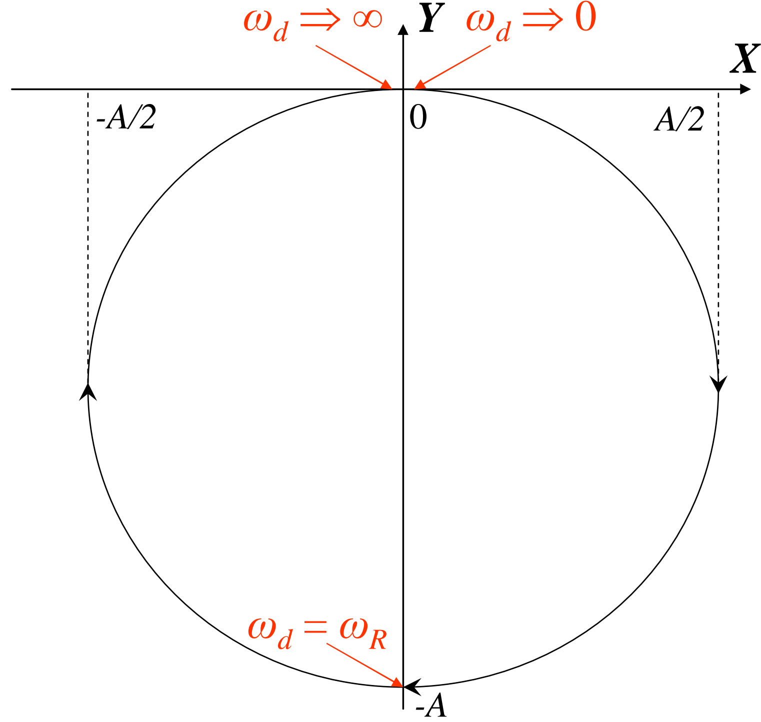

Figure A.1: Parametric plot of the real, X, and imaginary, Y, parts of the harmonic resonance response (A.1) with the drive frequency varying from 0 to infinity.

As a result, a typical parametric plot of detected X and Y quadratures will look as in Figs. A.2. The overall circular shape is preserved but it is subject to an arbitrary translation and rotation in the XY plane. For very high and low frequencies, the experimental points deviate from the fitted circle because the background varies slightly with frequency.

The two graphs A.2(a) and A.2(b) differ in the sign of the downmixed frequency $\Delta\omega$. As a result, the points on the parametric plots move in opposite directions in these graphs: clockwise in Figure A.2(a) and counterclockwise in Figure A.2(b). This difference in behavior can be understood by considering the phases of the voltages involved in downmixing. Generally, the change in piezoresistor's resistance follows the harmonic response and is in addition proportional to the intensity of drive, which in turn is proportional to the drive voltage V_d in the case of piezoshaker drive (Section 2.1), and the square of the drive voltage in the case of thermoelastic drive (Section 2.3).

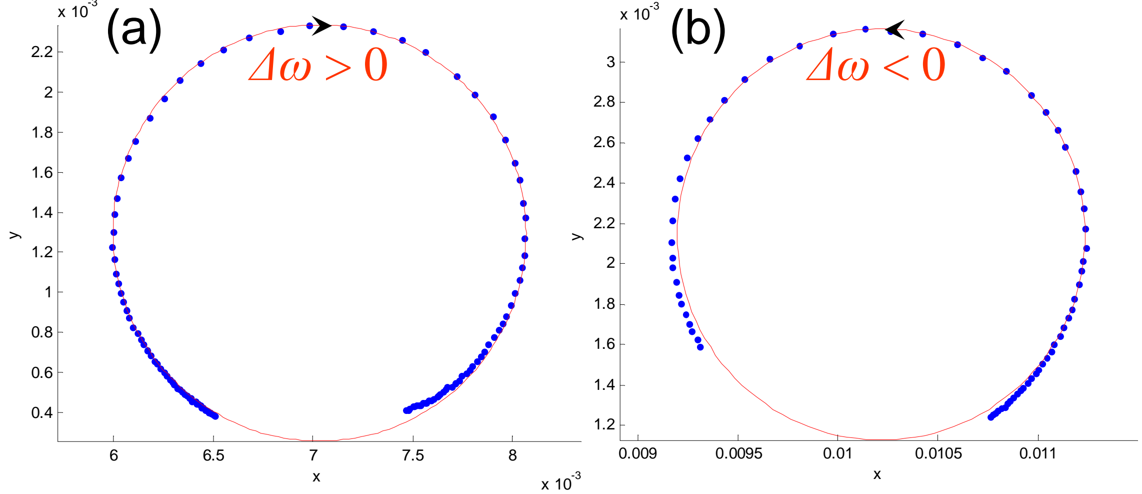

Figure A.2: Parametric plot of the real, X, and imaginary, Y, parts of the resonance response of a 37-MHz beam resonator. The circles are not complete because the drive frequency was varied approximately in the range $\omega_R - \omega_R/Q \leq \omega_d \leq \omega_R + \omega_R/Q$ in both figures. The left panel (a) shows the response for $\Delta\omega = +110$ kHz; the right panel (b), for $\Delta\omega = -110$ kHz. Note that the circles in panels (a) and (b) are rotated by similar, but not identical angles with respect to the "canonical" orientation in Figure A.1. With increasing frequency, the points move clockwise in panel (a) and counterclockwise in panel (b), as indicated by arrows.

Considering the shaker case for definiteness, the change in piezoresistor's resistance is given by

$$\Delta R = gV_d \cos(\omega_d t + \phi_d + \varphi_{res})|s|, \tag{A.2}$$

where g is the effective gauge factor of the piezoresistor, ϕ_d describes the phase delay of the drive with respect to the drive voltage due to cable delays, propagation delay of ultrasound in the silicon chip, and other factors; and $\varphi_{res} = \text{Arg}(s)$ is the phase and $|s|$ the amplitude of the resonant response (A.1) itself. When mixed with the bias voltage $V_b \cos((\omega_d - \Delta\omega)t + \phi_b)$, the resulting downmixed signal is proportional to

$$\begin{aligned} V_s &\propto V_d V_b \cos(\omega_d t + \phi_d + \varphi_{res} - (\omega_d - \Delta\omega)t - \phi_b)|s| && \text{(A.3)} \\ &= V_d V_b \cos(\Delta\omega t + \phi_d - \phi_b + \varphi_{res})|s| && \text{(A.4)} \\ &\equiv V_d V_b \cos(-\Delta\omega t - \phi_d + \phi_b - \varphi_{res})|s|, && \text{(A.5)} \end{aligned}$$

where I use the fact that cosine is an even function of its argument.

If the frequency offset is positive $\Delta\omega > 0$, the downmixed electrical signal has the same phase delay φ_{res} as the harmonic response (A.1). Accordingly, the point moves clockwise along the circle in the parametric plot of Figure A.2(a). Conversely, if frequency offset is negative $\Delta\omega < 0$, the phase of the signal voltage has the opposite delay to that of the harmonic response (A.1) and as a result, the point moves counterclockwise in Figure A.2(b). Therefore, in order to preserve the proper phase response of the downmixed signal, the frequency offset should preferably be kept positive, i. e., the bias frequency should be lower than the drive frequency.

Note that the same counterclockwise motion as in Figure A.2(b) would be observed for the harmonic response (A.1) if we flipped the sign of the quality factor (i. e., made it negative) since it would flip the phase of the response as well. Accordingly, the data-fitting program developed by Inna Kozinsky and myself [60] produces fits with either positive or negative quality factors, depending on the sign of the frequency offset. This ability of the fitting program to produce fits with both positive and negative Q factors also helped us to identify resonances in the two-port thermoelastic drive measurements, described in the next section.

Appendix B

Two-port measurements using piezoresistive downmixing and thermoelastic actuation

The combination of thermoelastic actuation and piezoresistive downmixing described in Section 2.3 uses two separate metal loops for actuation and detection. In principle, the same combination of thermoelastic actuation and piezoresistive downmixing can be used when only one loop is available, as for example in the case of a simple two-legged cantilever (see Figs. 1.2(a) and 1.2(c)). Figure B.1 shows the schematic of the measurement setup in this case. Both the drive and bias voltages are combined and sent into the metal loop. On the other side of the loop, a relatively large RF capacitor $C_{RF} = 6$ nF is connected to ground and therefore creates a virtual ground at high frequencies, $f \gg 1/(2\pi \cdot 50\ \Omega \cdot 6\ \text{nF}) \approx 500$ kHz. This ensures that both the drive and bias voltages primarily drop across the metal loop of the resonator rather than elsewhere in the circuit. A low-pass filter removes the remaining RF voltages, transmitting only the downmixed signal at frequency $\Delta\omega$, which is typically 100 kHz or less.

One difference between the four-port measurement described in Section 2.3 and the two-port measurement is the existence of a significant background in the two-port case. This background arises because the resistance of the piezoresistor depends not only on strain but also on the temperature. Since thermoelastic actuation relies on temperature variations to drive the cantilever, we cannot easily avoid this type of background. This effect produces a background signal at the downmixed frequency because the variations in resistance due to changing temperature and those due to the

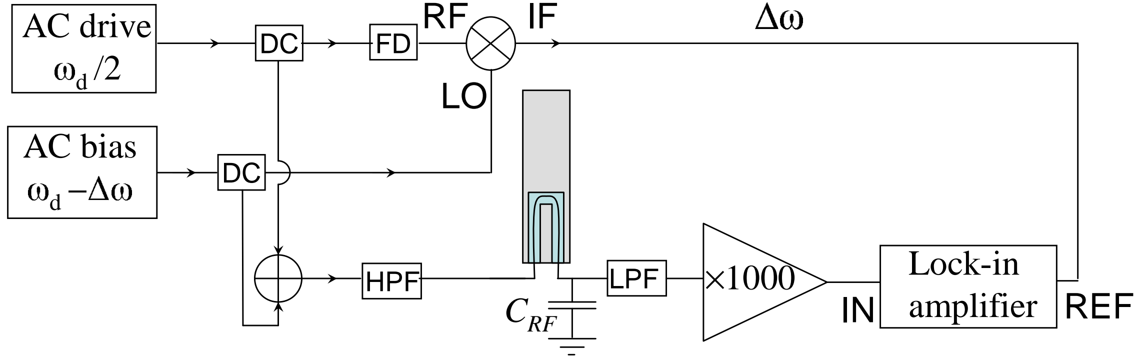

Figure B.1: Schematic of two-port measurement using thermoelastic actuation and piezoresistive detection. DC is the directional coupler, FD is the frequency doubler, HPF is the high-pass filter, LPF is the low-pass filter.

cantilever motion happen at the same frequency, and therefore mix down to the same frequency $\Delta\omega$. The magnitude of the background signal can be estimated as $V_b \sim V_b/2\alpha_R \Delta T$, where α_R is the temperature coefficient of resistance (on the order of 4×10^{-3} K^{-1} for most pure metals) and ΔT is the amplitude of temperature variations. In practice, this background and the resonant signal were roughly of the same order of magnitude for resonators with quality factors on the order of one thousand. As a result, the two-port measurement is relatively easy to use for vacuum measurements, where the signal is usually comparable to the background, and more difficult in air, where the quality factor can be as low as ten and signal can be orders of magnitude smaller than the background.

One way to reduce this type of background would be to fabricate the loop from specialty alloys like nichrome, constantan, or manganine, which are designed to have temperature coefficients of resistance up to two orders of magnitude smaller than those of pure metals. We have not yet explored this possibility due to the associated difficulties in fabrication. Another way to reduce this background is to use two separate, thermally isolated loops for actuation and detection. For the two-loop beam configuration described in Section 2.3, the thermal isolation is not perfect and heating one loop still affects the temperature of the other, but the separation between loops is large enough and the resulting isolation is good enough to make the background insignificant in practice.

Two-port measurement also differs from four-port measurements in that each mechanical resonance produces not one but two peaks during wide frequency sweeps of the kind shown in Figure

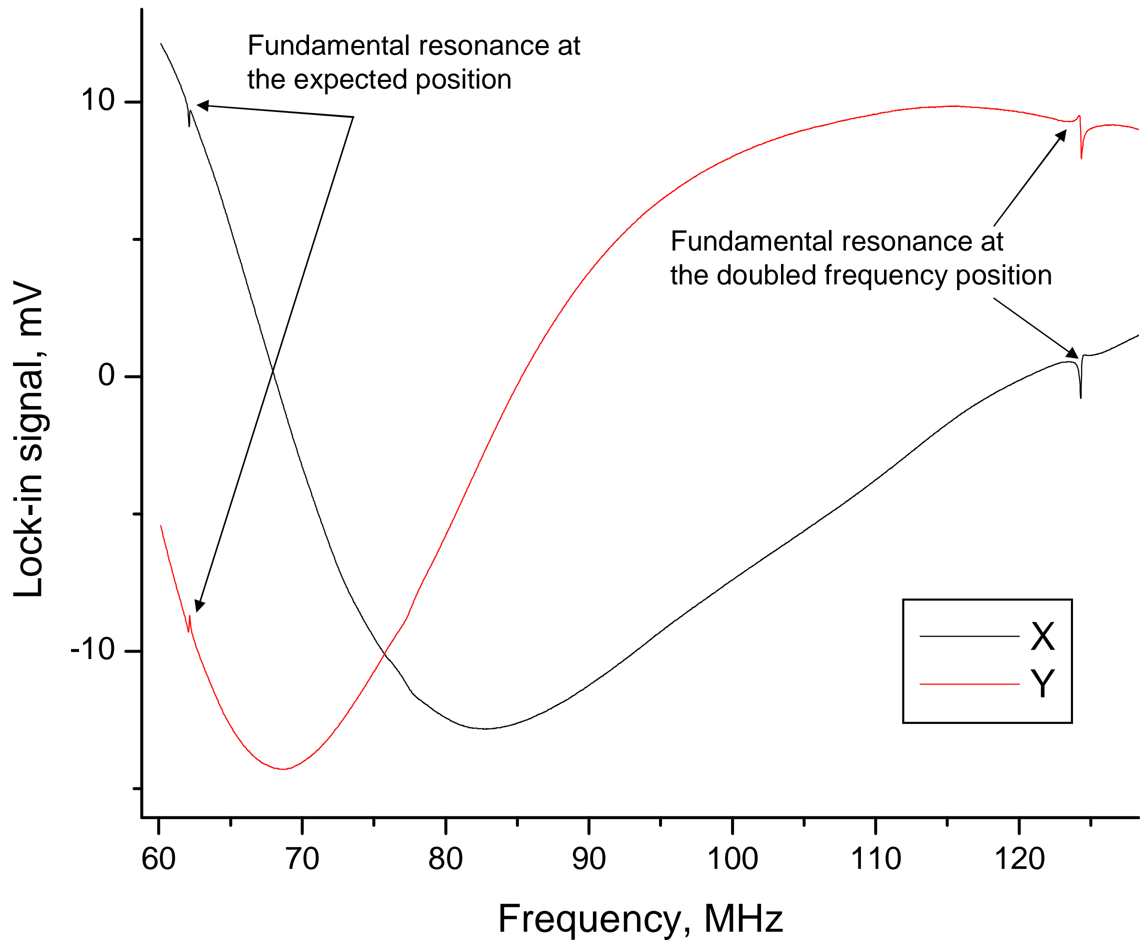

Figure B.2: Wide frequency sweep for a two-port measurement of a 1.6-μm long cantilever with the fundamental out-of-plane resonance frequency of 62.11 MHz. The sweep exhibits one resonance peak at the expected resonance frequency and another at roughly twice the expected frequency. Lorentzian fits of these two peaks produce resonance frequencies of 62.11 MHz and 124.32 MHz, quality factors of +1000 and −1000, and amplitudes of 0.75 mV and 1.45 mV, respectively. The frequency offset was 44 kHz for this measurement.

2.7. The first one appears at the expected position where the voltages are applied at the frequencies $\omega_1 = \omega_d/2 = \omega_R/2$ and $\omega_2 = \omega_b = \omega_R - \Delta\omega$. The second peak appears when one voltage is applied at the frequency $\omega_1 = \omega_R + \Delta\omega$ and another at $\omega_2 = 2\omega_R + \Delta\omega$. To understand how this peak forms, note that when we apply both of these voltages to the same loop, they will mix and produce temperature variations at the difference frequency $\omega_2 - \omega_1 = (2\omega_R + \Delta\omega) - (\omega_R + \Delta\omega) = \omega_R$, therefore driving the resonance. The resistance variations at frequency ω_R can now mix with the applied voltage at frequency $\omega_1 = \omega_R + \Delta\omega$ to produce a signal at the expected downmixed frequency $\Delta\omega$. The net result is that another peak appears in the graph at roughly twice the frequency of the expected peak. Figure B.2 shows a typical two-port frequency sweep showing a peak at the expected frequency and an additional peak at roughly twice the expected frequency.

Surprisingly, the amplitude of the additional peak is twice bigger than that of the expected peak. This can be explained by considering the algebraic relationships of the various voltage-mixing processes involved. If we apply a sum of two voltages of frequencies ω_1 and $\omega_2 = 2\omega_1 - \Delta\omega$, the heating is proportional to the square of total voltage:

$$\Delta T \propto (V_1 \cos\omega_1 t + V_2 \cos\omega_2 t)^2 = V_1^2 \cos^2\omega_1 t + 2V_1 V_2 \cos\omega_1 t \cos\omega_2 t + V_2^2 \cos^2\omega_2 t \quad \text{(B.1)}$$

$$= \frac{1}{2}V_1^2 \cos 2\omega_1 t + V_1 V_2 \cos(\omega_2 - \omega_1)t + \frac{1}{2}V_2^2 \cos 2\omega_2 t + \ldots. \quad \text{(B.2)}$$

Therefore, the temperature variations at frequency $(\omega_2 - \omega_1)$ are twice as big than those at frequency $2\omega_1$, and therefore drive the cantilever motion twice harder. The additional mixing process that produces the downmixed signal at frequency $\Delta\omega$ does not change that conclusion: the amplitude of "double-frequency" peak is twice that of the "regular" peak.

In addition to the twofold difference in amplitude, the phase of the resonance response of the additional peak is flipped with respect to that of the expected peak for reasons similar to those described as in the preceding section. As a result, the regular peaks are fitted with positive quality factors, while additional "double-frequency" peaks, with negative. This turns out to be helpful when analyzing data from wide measurement sweeps that contain peaks from multiple mechanical

resonances: if the fitted Q is positive, then there is indeed a mechanical resonance at the expected frequency $\omega_e = 2\omega_1 = \omega_2 + \Delta\omega$; however, if the fitted Q is negative, the real mechanical resonance happens at the frequency $\omega_e/2 - \Delta\omega$. In sensing applications, it is often more convenient to work with this "double-frequency" resonance peak since its signal-to-noise ratio is usually twice better for the same amount of heating.

Appendix C

Simulation of thermoelastic drive and piezoresistive detection

In Section 2.3, I described electrothermal actuation and piezoresistive detection of NEMS, which is effective at frequencies up to several hundred megahertz. Since the effectiveness of both electrothermal actuation and piezoresistive detection depends on the particular mode shape of the resonance, it makes sense to evaluate the combined efficiency of this actuation–detection scheme. In this appendix, I describe in more detail how one can theoretically estimate the response of this scheme using analytical calculations and finite-element simulations.

As described in Section 1.2, piezoresistive detection of motion uses the variation ΔR in the resistance R of the conducting loop, which in metals is mainly caused by the changes in the shape of the conductor [5]. The amplitude of the downmixed piezoresistive signal is approximately $V_s \approx V_b \Delta R/(2R) = V_b g \langle \epsilon_{xx} \rangle /2$, where V_b is the amplitude of the applied AC bias voltage, g is the effective gauge factor of the piezoresistor, and $\langle \epsilon_{xx} \rangle$ is the average longitudinal strain in the displacement transducer (coordinate axes are shown in the inset to Figure 2.8). The gauge factor of most thin metal films is on the order of two [5], and measurements of thermomechanical noise in our devices are consistent with this estimate. The longitudinal strain is determined by the mode shape, $\mathbf{u}^{(n)}(\mathbf{r})$, which specifies the vector displacement $\mathbf{u}$ of the infinitesimal volume element located at radius vector $\mathbf{r}$ for the considered mode number n. The mode shape produced by finite element simulation software will generally have an arbitrary amplitude, and to compensate for this fact, we will introduce a dimensionless drive-dependent mode amplitude c_n, so that the actual displacement field for a given

drive will be $c_n \mathbf{u}^{(n)}(\mathbf{r})$. The average longitudinal strain is then given by $\epsilon_{xx} = c_n \left\langle \partial u_x^{(n)}(\mathbf{r})/\partial x \right\rangle$, where the averaging is over the volume of the piezoresistor (for example, the 50-nm-wide detection legs on the left inset of Figure 2.6).

In order to determine the drive-dependent mode amplitude c_n, we will make a number of approximations that make the problem more tractable. In particular, we will assume that the temperature variations induced by the actuation voltage are sinusoidal, which is to be expected from sinusoidal actuation voltage. We will also assume that the quality factor of the considered mode is large enough that, on resonance, we can neglect the excitation of all other modes of the NEMS structure.

At the resonance frequency ω_n, the power continuously dissipated by the structure due to the finite mechanical quality factor of the system is the product of the energy loss rate multiplied by the maximum kinetic energy of the mode:

$$P_{diss} = \frac{\omega_n}{Q_n} \times \frac{c_n^2 \omega_n^2}{2} \int \rho(\mathbf{r}) \mathbf{u}^{(n)}(\mathbf{r})^2 d\mathbf{r} \equiv \frac{c_n^2 \omega_n^3}{2Q_n} \int \rho(\mathbf{r}) \mathbf{u}^{(n)}(\mathbf{r})^2 d\mathbf{r}, \tag{C.1}$$

where $\rho(\mathbf{r})$ the local mass density and the integration is over the volume of the entire simulated device. In the steady state, the dissipated power is compensated by the mechanical work done by the time-varying stresses induced by the drive. Note that the total stress tensor inside consists of three parts: the thermal stresses, the purely elastic stresses associated with the resonant motion, and the inelastic stresses associated with the dissipation mechanisms. The work of the inelastic (loss) stresses is negative, and its absolute value is given by Eqn. C.1. The work of the purely elastic stresses averages to zero over the full period. This leaves us with the thermal stresses, which actually drive the motion of the device.

Averaged over one oscillation amplitude, the mechanical power produced by the thermal stresses is given by

$$P_{therm} = c_n \frac{\omega_n}{2} \int \sum_{i,j} \sigma_{ji}(\mathbf{r}) \frac{\partial \mathbf{u}_i^{(n)}(\mathbf{r})}{\partial \mathbf{r}_j} d\mathbf{r}. \tag{C.2}$$

Here the summation is over all spatial coordinates and the integrals are over the volume of the bilayer resonator and $\sigma_{ji}(\mathbf{r})$ the amplitude of the thermal stress tensor. If we assume, for simplicity,

that gold and silicon carbide are elastically isotropic then $\sigma_{ii}(\mathbf{r}) \approx 3\alpha(\mathbf{r})\Delta T(\mathbf{r})B(\mathbf{r})$, where $\alpha(\mathbf{r})$ is the thermal coefficient of linear expansion, $\Delta T(\mathbf{r})$ is the amplitude of temperature change, and $B(\mathbf{r})$ is the bulk modulus.

Equating expressions C.1 and C.2 allows us to solve for the mode amplitude

$$c_n = \frac{Q_n}{\omega_n^2} \frac{\int 3\alpha(\mathbf{r})\Delta T(\mathbf{r})B(\mathbf{r}) \sum_i \frac{\partial \mathbf{u}_i^{(n)}(\mathbf{r})}{\partial \mathbf{r}_i} d\mathbf{r}}{\int \rho(\mathbf{r})\mathbf{u}^{(n)}(\mathbf{r})^2 d\mathbf{r}}. \tag{C.3}$$

The amplitude of the corresponding downmixed voltage signal is then given by

$$a = V_b g \langle \epsilon_{xx} \rangle /2 = V_b \frac{g Q_n}{2\omega_n^2} \frac{\left\langle \partial u_x^{(n)}(\mathbf{r})/\partial x \right\rangle \times \int 3\alpha(\mathbf{r})\Delta T(\mathbf{r})B(\mathbf{r}) \sum_i \frac{\partial \mathbf{u}_i^{(n)}(\mathbf{r})}{\partial \mathbf{r}_i} d\mathbf{r}}{\int \rho(\mathbf{r})\mathbf{u}^{(n)}(\mathbf{r})^2 d\mathbf{r}}. \tag{C.4}$$

In the expression above, the resonance frequency, ω_n, and the mode shape, $\mathbf{u}^{(n)}(\mathbf{r})$, along with its spatial derivatives, can be found from finite-element simulations. The only term that presents further difficulty is the spatial distribution of the temperature variation $\Delta T(\mathbf{r})$. Note that this is the amplitude of temperature oscillations at the frequency of the considered mode rather than the total temperature increase due to Joule heating with drive voltage V_d.

In principle, the temperature variations can again be found using finite-element simulations, although in practice it can be quite laborious since it is a dynamic (rather than static) problem involving direct-current electrostatics and thermal conductance. An additional complication is that for NEMS devices, some of the structural dimensions often approach the mean free path of electrons and/or phonons in the material, making boundary scattering significant and thus making the standard bulk analysis of thermal and electrical conductance inappropriate [124].

If the dimensions of the actuation loop are fixed, one can make a number of assumptions that simplify the analysis significantly. In particular, since most of the temperature variation due to Joule heating happens inside the drive loop and the thermal expansion coefficient of gold (and most other metals) is much larger than that of substrate semiconductors, we can limit the integration in the numerator of Eqn. (C.4) to the volume of the conductor loop. Furthermore, we found from numerical simulations that, for excitation frequencies below the inverse thermal time constant of

the drive loop, the amplitude of temperature variations is spatially roughly constant throughout the drive loop, which allows us to move the temperature dependence outside integral:

$$a = V_b \frac{gQ_n}{2\omega_n^2} \frac{3\alpha_{Gold}\Delta T_{Gold} B_{Gold} \left\langle \partial u_x^{(n)}(\mathbf{r})/\partial x \right\rangle \times \int \sum_i \frac{\partial \mathbf{u}_i^{(n)}(\mathbf{r})}{\partial \mathbf{r}_i} d\mathbf{r}}{\int \rho(\mathbf{r}) \mathbf{u}^{(n)}(\mathbf{r})^2 d\mathbf{r}}, \tag{C.5}$$

where the averaging in the numerator is over the legs of the detection loop, the integral in the numerator is over the volume of the drive loop, and the integral in the denominator is over the volume of the entire device. In this approximation, the amplitude of detected signal depends largely on the frequency and shape of the considered mode.

The analysis above can most easily be applied to the analysis of multiple modes of the same device, as was done in Section 2.3 but can also, to some extent, guide the design of new devices, especially if the geometry of the drive loop remains fixed. In this latter case, the amplitude of temperature variations inside the drive loop will remain roughly constant even as the geometry of the rest of the device varies, and the combined efficiency of the actuation and excitation primary depends on the shape of the mechanical modes.

In our experiments, the optimal shape of the excitation loop was found largely through trial and error. In general, the best results were obtained when the thickness of the excitation loop and the structural substrate were approximately the same. If multiple modes are to be measured, it is beneficial to keep the excitation and detection loop as short as possible as this prevents cancellation of the integral and average in the numerator of Eqn. (C.5) for higher modes and keeps the thermal time constant as short as possible. If only one mode is to be measured in the experiment, the length of the actuation loop can be extended to approximately the first inflection point of the considered mode in order to maximize the integrals in Eqn. (C.5). Note, however, that for operation at high frequencies, this increase in the drive integral can be offset by an increase in the thermal time constant of the device, which will reduce the amplitude of useful temperature variations in the drive loop and instead increase the average temperature of the device.

Bibliography

[1] K.E. Petersen, *Silicon as a Mechanical Material*, Proc. IEEE **70**, 420 (1982).

[2] C. Liu, *Foundations of MEMS* (Prentice Hall, London, 2005).

[3] A.N. Cleland, M.L. Roukes, *A nanometre-scale mechanical electrometer*, Nature **392**, 160 (1998).

[4] Y.T. Yang, C. Callegari, X.L. Feng, K.L. Ekinci, M.L. Roukes, *Zeptogram-scale nanomechanical mass sensing*, Nano Lett. **6**, 583 (2006).

[5] M. Li, H.X. Tang, M.L. Roukes, *Ultra-sensitive NEMS-based cantilevers for sensing, scanned probe and very high-frequency applications*, Nat. Nanotech. **2**, 114 (2007).

[6] J.S. Bunch, A.M. van der Zande, S.S. Verbridge, I.W. Frank, D.M. Tanenbaum, J.M. Parpia, H.G. Craighead, P.L. McEuen, *Electromechanical resonators from graphene sheets*, Science **315** 490 (2007).

[7] H.J. Mamin, D. Rugar, *Sub-attonewton force detection at millikelvin temperatures*, Appl. Phys. Lett. **79**, 3358 (2001).

[8] D. Rugar, R. Budakian, H.J. Mamin, B.W. Chui, *Single spin detection by magnetic resonance force microscopy*, Nature (London) **430**, 329 (2004).

[9] H.J. Mamin, M. Poggio, C.L. Degen, D. Rugar, *Nuclear magnetic resonance imaging with 90-nm resolution*, Nat. Nanotech. **2** 301 (2007).

[10] R.G. Knobel, A.N. Cleland, *Nanometre-scale displacement sensing using a single electron transistor*, Nature (London) **424**, 291 (2003).

[11] M.D. LaHaye, O. Buu, B. Camarota, K.C. Schwab, *Approaching the quantum limit of a nanomechanical resonator*, Science **304**, 77 (2004).

[12] A. Naik, O. Buu, M.D. LaHaye, A.D. Armour, A.A. Clerk, M.P. Blencowe, K.C. Schwab, *Cooling a nanomechanical resonator with quantum back-action*, Nature (London) **443**, 193 (2006).

[13] D. Karabacak, T. Kouh, K.L. Ekinci, *Analysis of optical interferometric displacement detection in nanoelectromechanical systems*, J. Appl. Phys. **98**, 124309 (2005).

[14] I. De Vlamincka, J. Roels, D. Taillaert, D. Van Thourhout, R. Baets, L. Lagae, G. Borghs, *Detection of nanomechanical motion by evanescent light wave coupling*, Appl. Phys. Lett. **90**, 233116 (2007).

[15] P.A. Truitt, J.B. Hetzberg, C.C. Huang, K.L. Ekinci, K.C. Schwab, *Efficient and sensitive capacitive readout of nanomechanical resonator arrays*, Nano Lett. **7**, 120 (2007).

[16] A.N. Cleland, M.L. Roukes, *Fabrication of high frequency nanometer scale mechanical resonators from bulk Si crystals*, Appl. Phys. Lett. **69**, 2653 (1996).

[17] X.M.H. Huang, C.A. Zorman, M. Mehregany, M.L. Roukes, *Nanodevice motion at microwave frequencies*, Nature **421** 496 (2003).

[18] N.E. Flowers-Jacobs, D.R. Schmidt, and K.W. Lehnert, *Intrinsic noise properties of atomic point contact displacement detectors*, Phys. Rev. Lett. **98**, 096804 (2007).

[19] V. Sazonova, Y. Yaish, H. Ustunel, D. Roundy, T.A. Arias, P.L. McEuen, *A tunable carbon nanotube electromechanical oscillator*, Nature (London) **431**, 284 (2004)

[20] H.B. Peng, C.W. Chang, S. Aloni, T.D. Yuzvinsky, A. Zettl, *Ultrahigh frequency nanotube resonators*, Phys. Rev. Lett. **97**, 087203 (2006).

[21] Y. Kanda, *Piezoresistance effect of silicon*, Sens. Actuators **A28**, 83 (1991).

[22] M. Tortonese, R.C. Barrett, C.F. Quate, *Atomic resolution with an atomic force microscope using piezoresistive detection*, Appl. Phys. Lett. **62**, 834 (1993).

[23] J.A. Harley, T.W. Kenny, *High-sensitivity piezoresistive cantilevers under 1000 angstrom thick*, Appl. Phys. Lett. **75**, 289 (1999).

[24] H.J. Mamin, R.P. Ried, B.D. Terris, D. Rugar, *High-density data storage based on the atomic force microscope*, Proc. IEEE **87**, 1014 (1999).

[25] P. Vettiger, G. Cross, M. Despont, U. Drechsler, U. Durig, B. Gotsmann, W. Haberle, M.A. Lantz, H.E. Rothuizen, R. Stutz, G.K. Binnig, *The "millipede"—Nanotechnology entering data storage*, IEEE Trans. Nanotech. **1**, 39 (2002).

[26] R.L. Gunter, W.G. Delinger, K. Manygoats, A. Kooser, T.L. Porter, *Viral detection using an embedded piezoresistive microcantilever sensor*, Sens. Actuat. A **107**, 219 (2003).

[27] J. Arlett, J.R. Maloney, B. Gudlewski, M. Muluneh, M.L. Roukes, *Self-sensing micro- and nanocantilevers with attonewton-scale force resolution*, Nano Lett. **6**, 1000 (2006).

[28] K. Hjort, J. Soderkvist, and J. Schweitz, *Gallium arsenide as a mechanical material*, J. Micromech. Microeng. **4**, 1 (1994).

[29] I. Bargatin, I. Kozinsky, M.L. Roukes, *Efficient electrothermal actuation of multiple modes of high-frequency nanoelectromechanical resonators*, Appl. Phys. Lett. **90**, 093116 (2007).

[30] F.N. Hooge, *1/f noise sources*, IEEE Trans. Elecron Dev. **41**, 1926 (1994).

[31] F.N. Hooge, *1/f noise in continuous thin gold films*, Physica, **45**, 386 (1969).

[32] M. Li, *Very high frequency nano-electro-mechanical resonators and their chemical sensing applications*, Ph.D. Thesis, California Institute of Technology, 2007.

[33] K.L. Ekinci, Y.T. Yang, X.M.H. Huang, M.L. Roukes, *Balanced electronic detection of displacement in nanoelectromechanical systems*, Appl. Phys. Lett **81** 2253 (2002).

[34] A.N. Cleland, M.L. Roukes, *Noise processes in nanomechanical resonators*, J. Appl. Phys. **92**, 2758 (2002).

[35] D.W. Carr, S. Evoy, L. Sekaric, H.G. Craighead, J.M. Parpia, *Measurement of mechanical resonance and losses in nanometer scale silicon wires*, Appl. Phys. Lett. **75**, 920 (1999).

[36] S.C. Masmanidis, R.B. Karabalin, I. de Vlaminck, G. Borghs, M.R. Freeman, M.L. Roukes, *Multifuctional nanomechanical systems via tuneably coupled pizoelectric actuation*, Science **317** 780 (2007).

[37] X.M.H. Huang, M. Manolidis, S.C. Jun, J. Hone, *Nanomechanical hydrogen sensing*, Appl. Phys. Lett. **86**, 143104 (2005).

[38] S.C. Jun, X.M.H. Huang, M. Manolidis, C.A. Zorman, M. Mehregany, J. Hone, *Electrothermal tuning of Al-SiC nanomechanical resonators*, Nanotechnology **17**, 1506 (2006).

[39] N.V. Lavrik, P.G. Datskos, *Femtogram mass detection using photothermally actuated nanomechanical resonators*, Appl. Phys. Lett. **82**, 2697 (2003).

[40] B. Ilic, S. Krylov, K. Aubin, R. Reichenbach, H.G. Craighead, *Optical excitation of nanoelectromechanical oscillators*, **86**, 193114 (2005).

[41] A. Sampathkumar, T.W. Murray, K.L. Ekinci, *Photothermal operation of high frequency nanoelectromechanical systems*, Appl. Phys. Lett. **88**, 223104 (2006).

[42] L. Jiang, R. Cheung, J. Hedley, M. Hassan, A.J. Harris, J.S. Burdess, M. Mehregany, C.A. Zorman, *SiC cantilever resonators with electrothermal actuation*, Sens. Act A **128**, 376 (2006).

[43] R.B. Reichenbach, M. Zalalutdinov, J.M. Parpia, H.G. Craighead, *RF MEMS oscillator with integrated resistive transduction*, IEEE Electron Device Lett. **27**, 805 (2006).

[44] I. Bargatin, E.B. Myers, J. Arlett, B. Gudlewski, M.L. Roukes, *Sensitive detection of nanomechanical motion using piezoresistive signal downmixing*, Appl. Phys. Lett. **86**, 133109 (2005).

[45] Y.T. Yang, K.L. Ekinci, X.M.H. Huang, L.M. Schiavone, M.L. Roukes, C.A. Zorman, M. Mehregany, *Monocrystalline silicon carbide nanoelectromechanical systems*, Appl. Phys. Lett. **78**, 162 (2001).

[46] I. Kozinsky, H.W.C. Postma, I. Bargatin, M.L. Roukes, *Tuning nonlinearity, dynamic range, and frequency of nanomechanical resonators*, Appl. Phys. Lett. **88**, 253101 (2006).

[47] S. Timoshenko, *Analysis of bi-metal thermostats*, J. Opt. Soc. Am. and Rev. Sci. Instr. **11**, 233 (1925).

[48] K.M. Jackson, J. Dunning, C.A. Zorman, M. Mehregany, W.N. Sharpe, *Mechanical properties of epitaxial 3C silicon carbide thin films*, J. MEMS **14**, 664 (2005).

[49] J.J. Yao, N.C. MacDonald, *A micromachined, single-crystal silicon, tunable resonator*, J. Micromech. Microeng. **5**, 257 (1995).

[50] S.M.M. Kafumbe, J.S. Burdess, A.J. Harris, *Frequency adjustment of microelectromechanical cantilevers using electrostatic pull down*, J. Micromech. Microeng. **15**, 1033 (2005).

[51] F.D. Bannon, J.R. Clark, C.T.-C. Nguyen, *High-Q HF microelectromechanical filters*, IEEE J. Sol. St. Circ., **35** (2000).

[52] M. Agarwal, S.A. Chandorkar, H. Mehta, R.N. Candler, B. Kim, M.A. Hopcroft, R. Melamud, C.M. Jha, G. Bahl, G. Yama, T.W. Kenny, B. Murmann, *A study of electrostatic force nonlinearities in resonant microstructures*, Appl. Phys. Lett. **92**, 104106 (2008).

[53] R.R.A. Syms, *Electrothermal frequency tuning of folded and coupled vibrating micromechanical resonators*, J. MEMS, **7**, 164 (1998).

[54] S. Enderling, J. Hedley, L.D. Jiang, R. Cheung, C. Zorman, M. Mehregany, A.J. Walton AJ, *Characterization of frequency tuning using focused ion beam platinum deposition*, J. MEMS, **17**, 213 (2007).

[55] B.J. Gallacher, J. Hedley, J.S. Burdess, A.J. Harris, M.E. McNie, *Multimodal tuning of a vibrating ring using laser ablation*, J. Mech. Eng. Sci. C **217**, 557 (2003).

[56] V. Sazonova, Y. Yaish, H. Ustunel, D. Roundy, T.A. Arias, P.L. McEuen, *A tunable carbon nanotube electromechanical oscillator*, Nature **431**, 284 (2004).

[57] K.L. Ekinci, X.M.H. Huang, M.L. Roukes, *Frequency-tunable micromechanical oscillator*, Appl. Phys. Lett. **84**, 4469 (2004).

[58] S.S. Verbridge, D. Finkelstein Shapiro, H.G. Craighead, J.M. Parpia, *Macroscopic tuning of nanomechanics: Substrate bending for reversible control of frequency and quality factor of nanostring resonators*, Nano Lett. **7**, 1728 (2007).

[59] M. Zalalutdinov, B. Ilic, D. Czaplewski, A. Zehnder, H.G. Craighead, J.M. Parpia, *Frequency-tunable micromechanical oscillator*, Appl. Phys. Lett. **77**, 3287 (2000).

[60] I. Kozinsky, *Nonlinear nanoelectromechanical systems*, Ph.D. Thesis, California Institute of Technology, 2007.

[61] I.I. Rabi, J.R. Zacharias, S. Millman, P. Kusch, *A new method of measuring nuclear magnetic moment*, Phys. Rev. **53**, 318(1938).

[62] C.P. Slichter, *Principles of magnetic resonance* (Springer, New York, 1990).

[63] J.A. Sidles, *Noninductive detection of single-proton magnetic resonance*, Appl. Phys. Lett. **58**, 2854 (1991).

[64] D. Rugar, C.S. Yannoni, J.A. Sidles, *Mechanical detection of magentic resonance*, Nature **360** 563 (1992).

[65] D. Rugar, O. Zuger, S. Hoen, C.S. Yannoni, H.-M. Vieth, R.D. Kendrick, *Force Detection of Nuclear Magnetic Resonance*, Science **264** 1560 (1994).

[66] J.A. Sidles, J.L. Garbini, K.J. Bruland, D. Rugar, O. Zuger, S. Hoen, C.S. Yannoni, *Magnetic resonance force microscopy*, Rev. Mod. Phys. **67**, 249 (1995).

[67] S. Kuehn, S.A. Hickman, J.A. Marohn, *Advances in mechanical detection of magnetic resonance*, J. Chem. Phys. **128**, 052208 (2008).

[68] J.A. Sidles, J.L. Garbini, G.P. Drobny, *The theory of oscillator-coupled magnetic resonance with potential applications to molecular imaging*, Rev. Sci. Instr. **63** 3881 (1992).

[69] Y.-J. Wang, M. Eardley, S. Knappe, J. Moreland, L. Hollberg, J. Kitching, *Magnetic resonance in an atomic vapor excited by a mechanical resonator*, Phys. Rev. Lett. **97**, 227602 (2006).

[70] D.I. Bolef, R.K. Sundfors, *Nuclear acoustic resonance* (Boston: Academic Press, 1993).

[71] A.C. Gossard, A.M. Portis, *Observation of nuclear resonance in a ferromagnet*, Phys. Rev. Lett. **3**, 164 (1959); A.C. Gossard, A.M. Portis, *Nuclear resonance in ferromagnetic cobalt*, J. Appl. Phys. **31**, S205 (1960).

[72] M. Cerisier, K. Attenborough, E. Jedrika, W. Wojcik, S. Nadolski, C. Van Haesendonck, J.P. Cellis, *Structural study of nanometric electrodeposited Co films using* ^{59}*Co NMR*, J. Appl. Phys. **89**, 7083 (2001).

[73] V.S. Pokatilov, S.V. Kapel'nitskii, V.N. Karazeev, *Nuclear magnetic resonance study of thin cobalt-base ferromagntic films*, Sov. Phys. Sol. St. **32**, 1155 (1990).

[74] C. Christides, S. Stavroyiannis, D. Niarchos, M. Wojcik, S. Nadolski, E. Jedrika, *Significant modificaton of* ^{59}*Co NMR hyperfine fields assigned to specific structural changes in sputtered Co/Au and Co/Cu multilayers*, Phys. Rev. B **59**, 8812 (1999).

[75] C.W. Miller, U.M. Mirsaidov, T.C. Messina, Y.J. Lee, J.T. Markert, *External field effects on the resonant frequency of magnetically capped oscillators for magnetic resonance force microscopy*, J. Appl. Phys. **93**, 6572 (2003).

[76] M. Weger, *Longitudinal nuclear magnetic relaxation in ferromagnetic iron, cobalt, and nickel*, Phys. Rev. **128**, 1505 (1962).

[77] J.P. Gordon, H.J. Zeiger, C.H. Townes, *Molecular microwave oscillator and high-resolution spectrometer*, Phys. Rev. **95**, 282 (1954); T.H. Maiman, *Stimulated optical radiation in ruby*, Nature **187**, 493 (1960).

[78] T.C. Marshall, *Free electron lasers* (MacMillan, New York, 1985).

[79] R. Badii, E. Brun, M. Finardi, L. Flepp, R. Holzner, J. Parisi, C. Reyl, J. Simonet, *Progress in the analysis of experimental chaos through periodic orbits*, Rev. Mod. Phys. **66** 1389 (1994).

[80] A. Suter, D.V. Pelekhov, M.L. Roukes, P.C. Hammel, *Probe-sample coupling in the magnetic resonance force microscope*, J. Magn. Res. **15** 210 (2002).

[81] K.J. Bruland, W.M. Dougherty, J.L. Garbini, J.A. Sidles, S.H. Chao, *Force-detected magnetic resonance in a field gradient of 250 000 Tesla per meter*, Appl. Phys. Lett. **73** 3159 (1998).

[82] A. Mehta, S. Cherian, D. Hedden, T. Thundat, *Manipulation and controlled amplification of Brownian motion of microcantilever sensors*, Appl. Phys. Lett. **78** 1637 (2001).

[83] R.B. Karabalin, X.L. Feng, S.C. Masmanidis, D.A. Harrington, R. Lifshitz, M.C. Cross, M.L. Roukes, *Parametric Amplification in High Frequency Nanomechanical Systems* (unpublished).

[84] E.T. Jaynes, F.W. Cummings, *Comparison of quantum and semiclassical radiation theories with application to the beam maser*, Proc. IEEE **51** 89 (1963).

[85] H. Haken, *Laser theory* (Springer, New York, 1984).

[86] Y. Kaluzny, P. Goy, M. Gross, J.M. Raimond, S. Haroche, *Observation of Self-Induced Rabi Oscillations in Two-Level Atoms Excited Inside a Resonant Cavity: The Ringing Regime of Superradiance*, Phys. Rev. Lett. **51** 1175 (1983).

[87] R.J. Brecha, L.A. Orozco, M.G. Raizen, M. Xiao, H.J. Kimble, *Observation of oscillatory energy exchange in a coupled-atom-cavity system*, J. Opt. Soc. Am. B **12** 2329 (1995).

[88] P.G. Bjornsson, B.W. Gardner, J.R. Kirtley, K.A. Moler, *Scanning superconducting quantum interference device microscope in a dilution refrigerator*, Rev. Sci. Instr. **72** 4153 (2001).

[89] P.R. Berman (Ed.), *Cavity quantum electrodynamics* (Academic, Boston, 1994).

[90] N. Bloembergen and R.V. Pound, *Radiation damping in magnetic resonance experiments*, Phys. Rev. **95** 8 (1954).

[91] R. Lifshitz, M.L. Roukes, *Thermoelastic damping in micro- and nanomechanical systems*, Phys. Rev. B **61**, 5600 (2000).

[92] R.N. Candler, M. Hopcroft, W.T. Park, S.A. Chandorkar, G. Yama, K.E. Goodson, M. Varghese, A.E. Duwel, A. Partridge, M. Lutz, T.W. Kenny, *Reduction in Thermoelastic Dissipation in Micromechanical Resonators by Disruption of Heat Transport*, Proceedings of the 2004 Solid State Sensors and Actuators Workshop, p. 45 (2004).

[93] M.C. Cross, R. Lifshitz, *Elastic wave transmission at an abrupt junction in a thin plate with application to heat transport and vibrations in mesoscopic systems*, Phys. Rev. B **64**, 085324 (2001).

[94] D.M. Photiadis, J.A. Judge, *Attachment losses of high Q oscillators*, Appl. Phys. Lett. **85**, 482 (2004).

[95] J.A. Judge, D.M. Photiadis, J.F. Vignola, B.H. Houston, J. Jarzynski, *Attachment loss of micromechanical and nanomechanical resonators in the limits of thick and thin support structures*, J. Appl. Phys. **101**, 013521 (2007).

[96] M.R. Geller, J.B. Varley, *Friction in nanoelectromechanical systems: Clamping loss in the GHz regime*, arXiv:cond-mat/0512710v1 (2005).

[97] D.S. Bindel, E. Qdvy, T. Koyamat, S. Govindjeet, J.W. Demmel, R.T. Howe, *Anchor Loss Simulation in Resonators*, Proceedings of MEMS 2005, Miami, FL (February 2005).

[98] J. Yang, T. Ono, M. Esashi, *Energy dissipation in submicrometer thick single-crystal silicon cantilevers*, J. MEMS **11**, 775 (2002).

[99] M. Imboden, P. Mohanty, A. Gaidarzhy, J. Rankin, B.W. Sheldon, *Scaling of dissipation in megahertz-range micromechanical diamond oscillators*, Appl. Phys. Lett. **90**, 173502 (2007).

[100] A.B. Hutchinson, P.A. Truitt, K.C. Schwab, L. Sekaric, J.M. Parpia, H.G. Craighead, J.E. Butler, *Dissipation in nanocrystalline-diamond nanomechanical resonators*, Appl. Phys. Lett. **84**, 972 (2004).

[101] X.M.H. Huang, X.L. Feng, C.A. Zorman, M. Mehregany, M.L. Roukes, *VHF, UHF and microwave frequency nanomechanical resonators*, New J. Phys. **7** 247 (2005).

[102] X.L. Feng, C.A. Zorman, M. Mehregany, M. L. Roukes, *Dissipation in single-crystal 3C-SiC ultra-high frequency nanomechanical resonators*, Tech. Digest, Solid-State Sensors, Actuators, and Microsystems Workshop, pp. 86-89 (Hilton Head, 2006).

[103] S.S. Verbridge, J.M. Parpia, R.B. Reichenbach, L.M. Bellan, H.G. Craighead, *High quality factor resonance at room temperature with nanostrings under high tensile stress*, J. Appl. Phys. **99**, 124304 (2006).

[104] J. Yang, T. Ono, M. Esashi, *Surface effects and high quality factors in ultrathin single-crystal silicon cantilevers*, Appl. Phys. Lett. **77**, 3860 (2000).

[105] T. Ono, M. Esashi, *Effect of ion attachment on mechanical dissipation of a resonator*, Appl. Phys. Lett. **87**, 044105 (2005).

[106] C. Seonez, F. Guinea, A.H. Castro Neto, *Surface dissipation in nanoelectromechanical systems: Unified description with the standard tunneling model and effects of metallic electrodes*, Phys. Rev. B **77**, 125107 (2008).

[107] M. Schlosshauer, A.P. Hines, G.J. Milburn, *Decoherence and dissipation of a quantum harmonic oscillator coupled to two-level systems*, Phys. Rev. A **77**, 022111 (2008).

[108] R.B. Bhiladvala, Z.J. Wang, *Effect of fluids on the Q factor and resonance frequency of oscillating micrometer and nanometer scale beams*, Phys. Rev. E **69**, 036307 (2004).

[109] D.M. Karabacak, V. Yakhot, K.L. Ekinci, *High-frequency nanofluidics: An experimental study using nanomechanical resonators*, Phys. Rev. Lett. **98**, 254505 (2007).

[110] M.K. Ghatkesar, T. Braun, V. Barwich, J.-P. Ramseyer, C. Gerber, M. Hegner, H.P. Lang, *Resonating modes of vibrating microcantilevers in liquid*, Appl. Phys. Lett. **92**, 043106 (2008).

[111] J.E. Sader, *Frequency response of cantilever beams immersed in viscous fluids with applications to the atomic force microscope*, J. Appl. Phys. **84**, 64 (1998).

[112] C.A. Van Eysden, J.E. Sader, *Frequency response of cantilever beams immersed in viscous fluids with applications to the atomic force microscope: Arbitrary mode order*, J. Appl. Phys. **101**, 044908 (2007).

[113] M.R. Paul, M.T. Clark, M.C. Cross, *The stochastic dynamics of micron and nanoscale elastic cantilevers in fluid: fluctuations from dissipation*, Nanotechnology **17** 4502 (2006).

[114] M.T. Clark, M.R. Paul, *The Stochastic Dynamics of Rectangular and V-shaped Atomic Force Microscope Cantilevers in a Viscous Fluid and Near a Solid Boundary*, arXiv:0801.2136v2 (2008).

[115] K.R. Patton, M.R. Geller, *Phonons in a nanoparticle mechanically coupled to a subtrate*, Phys. Rev. A **67**, 155418 (2003).

[116] C.M. Chang, M.R. Geller, *Mesoscopic phonon transmission through a nanowire-bulk contact*, Phys. Rev. A **71**, 125304 (2005).

[117] W. Panga, L. Yan. H. Zhang, H. Yu, E.S. Kim, W.C. Tang, *Femtogram mass sensing platform based on lateral extensional mode piezoelectric resonator*, Appl. Phys. Lett. **88**, 243503 (2006).

[118] J.E.-Y. Lee, B. Bahreyni, Y. Zhu, A.A. Seshia, *Ultrasensitive mass balance based on a bulk acoustic mode single-crystal silicon resonator*, Appl. Phys. Lett. **91**, 234103 (2007).

[119] M. Li, E.B. Myers, H.X. Tang, S.J. Aldridge, M.L. Roukes, R.J. Simonson, J.J. Whiting, *Nanomechanical resonator arrays for ultrafast microscale chromatographic chemical recognition* (unpublished).

[120] J. Zhang, H.P. Lang, F. Huber, A. Bietsch, W. Grange, U. Certa, R. McKendry, H.-J. Gunterodt, M. Hegner, Ch. Gerber, *Rapid and label-free nanomechanical detection of biomarker transcripts in human RNA*, Nat. Nanotech. **1**, 214 (2006).

[121] M. Li, R.B. Bhiladvala, T.J. Morrow, J.A. Sioss, K.-K. Lew, J.M. Redwing, C.D. Keating, T.S. Mayer, *Bottom-up assembly of large-area nanowire resonator arrays*, Nat. Nanotech. **3**, 88 (2008).

[122] S.-S. Li, Y.-W. Lin, Z. Ren, and C.T.-C. Nguyen, *Disk-array design for suppression of unwanted modes in micromechanical composite-array filters*, Tech. Digest, 19th IEEE Int. Conf. on Micro Electro Mechanical Systems (MEMS'06), p. 866, Istanbul, Turkey, (Jan. 22–26, 2006).

[123] S.-S. Li, Y.-W. Lin, Z. Ren, and C. T.-C. Nguyen, *An MSI micromechanical differential disk-array filter*, Dig. of Tech. Papers, the 14th Int. Conf. on Solid-State Sensors & Actuators (Transducers'07), p. 307, Lyon, France, (June 11-14, 2007).

[124] Y.S. Ju, K.E. Goodson, *Phonon scattering in silicon films with thickness of order 100 nm*, Appl. Phys. Lett. **74**, 305 (1999).